Smartphones for Control and Detection of Rapid Diagnostic Tests

Rahil Jain

A dissertation

submitted in partial fulfillment of the

requirements for the degree of

Doctor of Philosophy

University of Washington

2018

Reading Committee:

Barry R. Lutz, Co-Chair

Robert B. Darling, Co-Chair

Karl Bohringer

Program Authorized to Offer Degree:

Electrical Engineering

Abstract

Smartphones for Control and Detection of Rapid Diagnostic Tests

Rahil Jain

Chair of the Supervisory Committee:
Barry Lutz
Associate Professor
Department of Bioengineering

This dissertation discloses smartphone audio-powered microfluidic technologies for flow control and detection in point-of-care rapid diagnostic tests. This work builds on the classic electric-hydraulic analogy and the concept of frequency-tuning to create, model, and characterize microfluidic equivalents of RLC electrical circuits with resonance in the audio range. These microfluidic resonant circuits were used to create novel microfluidic pump devices that provide both flow magnitude (on/off) and direction (forward/backward) control. The resonance frequency of microfluidic devices was most sensitive to the deformable part of the device that acts like a fluidic capacitor. By physically coupling this elastic capacitor to a clotting sample of plasma, enzymes essential to inducing elasticity to the blood clot, like fibrin cross-linking activator FXIIIa, can be functionally detected as resonance frequency shifts from the decreased total capacitance. Since flow control and analyte detection – two core components of a rapid

diagnostic test – occurs in the audio frequency range, this microfluidic technology is well-suited to be paired with any audio device, like a smartphone, to serve as a replacement for the instrumentation commonly required in disease testing.

TABLE OF CONTENTS

LIST OF FIGURES

LIST OF TABLES

ACKNOWLEDGEMENTS

First and foremost, I want to thank my advisor Dr. Barry Lutz. It has been an honor to be his first Ph.D. student. In addition to microfluidics, analogical thinking, critical reasoning, medical diagnostics, and entrepreneurship, Barry has taught me, both consciously and unconsciously, innumerable life lessons in people and project management, evangelism, honesty, and fortitude. I am indebted for all his contributions of time, ideas, and funding to make my Ph.D. experience productive and stimulating. The energy and enthusiasm he has for science, in general, are contagious. His managerial style is so unique that he never fails to motivate you while remaining patient and kind. Barry has set such a high bar for 'the Bossman' that I am confident that no one in my future can fill those shoes. I am also thankful for the excellent example he has provided balancing tough academic career and family.

I was lucky to have two advisors who stood by me and helped me keep focus the course of Ph.D. I am grateful to Dr. Robert B. Darling for advising me on the engineering aspects of my Ph.D. work. I have been profoundly amazed by the breadth of the knowledge Dr. Darling possess and it has immensely assisted in the development of the novel characterization tools I developed in this dissertation work. The coursework I took with Dr. Darling were the highlights of my time here at UW. In the final leg of the Ph.D. work, I had the opportunity to more closely collaborate with Dr. Darling on the Amazon Catalyst grant for the Airy battery-less sensors. His product vision supported by a broad technical knowledgebase has effectively guided the design and development of the product and related IP.

I am also grateful to my Ph.D. committee member Dr. Karl Bohringer and the GSR, Dr. Adam Alessio. They bring a different perspective to my work and their feedback, comments, and questions have helped broaden my purview.

The members of the Lutz group have contributed immensely to my personal and professional time at UW. The group has been a source of friendships as well as good advice

and collaboration. I am especially grateful to one of the most productive and helpful Lutz group members who stuck it out in grad school with me: Nuttada Panpradist. A person of immeasurable character and strength, Nuttada, has been a dependable source for help and guidance with basic information like immigration, committee formation, graduation policies to advanced scientific knowledge. I am also grateful for my undergraduate mentees Doan and Annapurni. Doan's capstone work with blood coagulation formed the basis for the analyte detection aspect of this thesis work. Annapurni helped execute numerous pet projects for me and I am glad she persisted without a clear pathway. I also thank Amy, Bob, Daniel, David, Enos, Ian, Jonathan, Shivani, and Zach for making life fun at the Lutz Lab.

Members of the Yager group have helped immensely when I was starting out. First and foremost, I acknowledge the generosity and support of Dr. Paul Yager in letting me access his lab facility and personnel. Dr. Bhushan Toley was my cubemate and I am beholden to all the impromptu discussions we had. Good times. Dr. Josh Buser has been an immense help in providing guidance with Blender and other 3D design tools that resulted in the eye-catching cover designs. I am appreciative of Peter Kauffman for numerous instrumentation and circuit discussions that affected the design of my experimentation setups and sensors featured in this work. Peter also taught me so much about coffee. I am also appreciative of other current and past members of the Yager group, particularly Dr. Carly Holstein, Dr. Sam Byrnes, Sujatha Ramachandran, Dr. Josh Bishop, Dr. Lisa Lafleur, Dr. Paula Ladd, and Max Wheeler. Last but not the least, Chelsea Musick, for always willing to help with online ordering and making sure the orders get delivered to us on time. Thanks so much.

I gratefully acknowledge the funding sources that made my Ph.D. work possible. I was funded by the National Science Foundation for my first 4 years. My work was also supported by the Amazon Catalyst award in the final stages of the Ph.D. I would also like to thank the U.S. Immigration Service whose irrational need for regular, months-long visa background checks forced me to remain in the country, miss a conference in Italy and another in China and miss meeting my family for last two years. Devoid of these useless distractions, it was during this time most of the dissertation work was completed.

I would also like to acknowledge our collaborators Dr. Nathan White and Blythe Adamson. I am also grateful to my team at Hook who stood by me and took over my responsibilities when I needed to focus on my real job. Thank you for that.

Lastly, I would like to thank my family for all their love and encouragement. For my parents who raised me with a love of science and supported me in all my pursuits. For the presence of my sister Rashi here in the States. And most of all for my loving, supportive, encouraging, and patient wife Swati whose faithful presence during the entire course of this Ph.D. is so appreciated. Thank you.

Chapter 1. INTRODUCTION

Smartphones are emerging as potential replacements for instrumentation involved in performing point-of-care (POC) rapid diagnostic tests (RDTs). This is fueled in part by the rapid rise of smartphone users, even in low-income nations[1]. Smartphone applications have predominantly focused on detecting test results using smartphone cameras[2]–[8]. In contrast, the core capability found on all smartphones – audio input and output – has been relatively unexploited in the development of microfluidic devices for health testing. Recently, cellphone audio output from the headphone jack was used to drive a sample preparation device that performed mechanical lysis of bacteria[9], and a separate work used the headphone jack to power the onboard electronics and communicate with the diagnostic dongle device[10]. These work mark significant milestones in audio-based diagnostic applications, while also highlighting the potential for further miniaturization and integration of RDTs. One such possibility is by merging microfluidics. This dissertation work capitalizes on this opportunity to create audio-responsive microfluidic circuits and demonstrates their application for flow control and analyte detection in RDTs.

Chapter 2 provides a detailed review of the smartphone applications for health monitoring and diagnostic testing. The potential for smartphones to revolutionize POC health testing in global health and low resource settings is highlighted. The unique advantages brought by a smartphone-based diagnostic approach in achieving the WHO ASSURED mandate are discussed in Section 2.2. The two audio-based diagnostic applications from above are reviewed in the context of this work. The opportunity to innovate and the challenges with such a novel approach to diagnostics are detailed in the concluding Section 2.3.

0 introduces the concept of audio-responsive microfluidic resonant circuits based on the classic electric-hydraulic analogy. The prior work in this field of 'frequency-tuning' is discussed in detail. Section 3.2 describes the parallel and series resonant modes in microfluidic circuits and the resemblance to their electrical counterparts. The modeling approach for microfluidic devices based on a simple electric circuit model with frequency-dependent circuit elements is outlined in Section 3.3. The laminated fabrication method for microfluidic resonant circuits is explained in Section 0.

Chapter 4 reports the electrically-inspired characterization toolkit developed for frequency mapping of flow magnitude and phase in microfluidic resonant circuits, illustrated in Figure 1.1. The techniques of AC analysis (Section 4.1), Fourier analysis (Section 4.2), and Step Analysis (Section 4.3), illustrated in Figure 1.2, are demonstrated through appropriate device designs. The concluding Section 4.4 describes how the choice of the characterization technique varies with the experimentation goal and available instrumentation, and evolves with the maturity of the technology platform.

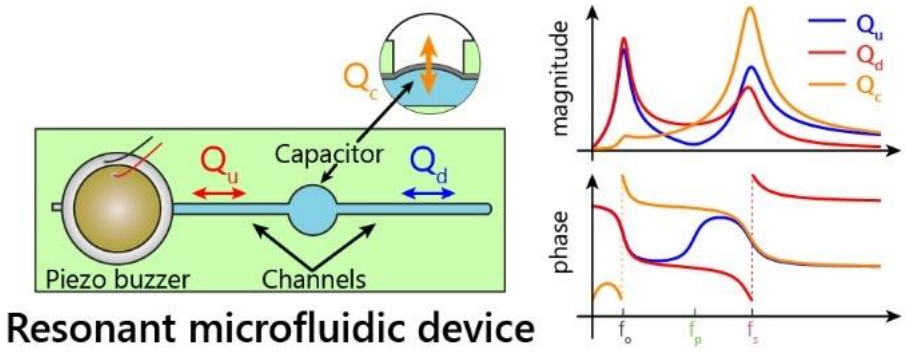

Figure 1.1. Microfluidic resonant device and model-predicted frequency response of the flow

Chapter 5 presents the application of the concepts developed so far for flow control applications. Design, fabrication, operation, and characterization of the frequency-tuned

microfluidic pumps based on audio-responsive circuits are presented in the opening Sections 5.1-5.5. Perhaps the most significant contribution of this dissertation work in form of frequency-tuned directional and bi-directional pumps are described in Section 5.6, and illustrated in Figure 1.3. The concluding Section 5.6 discusses applications of the frequency-tuned pumps for miniaturization and simplification of flow control in microfluidic lab-on-a-chip (LOC) devices.

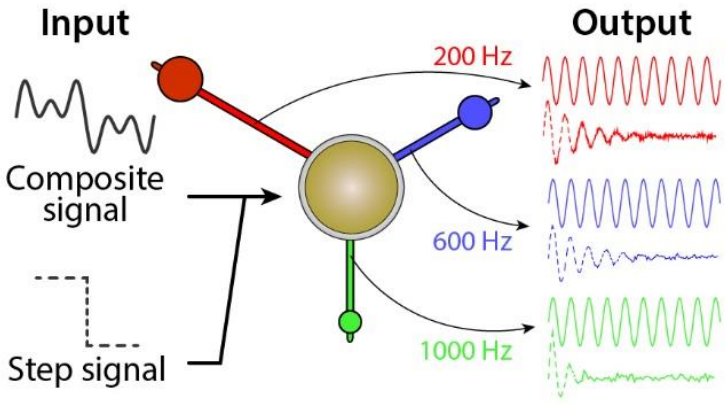

Figure 1.2. Frequency characterization using Fourier and Step Analysis techniques

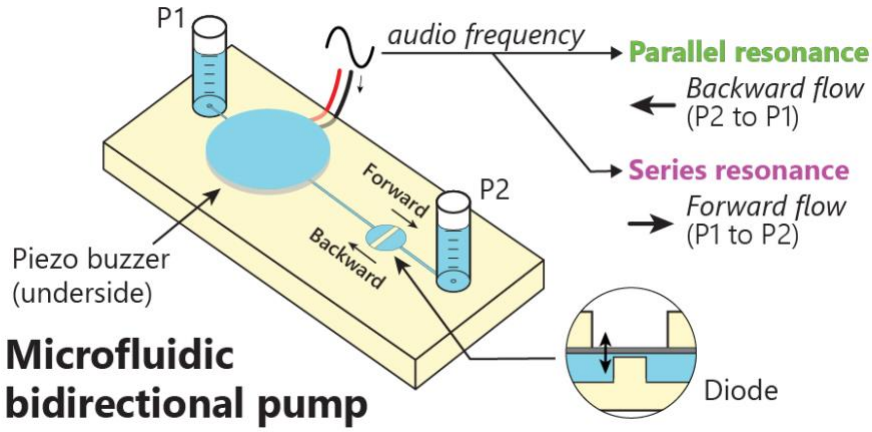

Figure 1.3. Frequency-tuned microfluidic bi-directional pump

Error! Reference source not found. demonstrates the application of microfluidic resonant circuits in functional measurement of blood coagulation. An overview of the coagulation cascade and the importance of the individual clotting factors and components for overall clot integrity is reviewed in Section 6.1. Current state-of-the-art coagulation global and local tests are also described in this section. In Section 6.2, the rheological properties of blood, plasma, and other blood derivatives are discussed. The changes in these rheological properties with clotting of blood and blood derivatives is discussed for elastic fibrin gel – the structural part of a blood clot. Section 6.2 also reviews the importance of FXIIIa in crosslinking of fibrin gels. Section **Error! Reference source not found.** presents the concept and the preliminary results from using the microfluidic resonant circuits for FXIIIa level measurement in fibrinogen-thrombin clots. In the concluding Section 6.4, the outlook for this novel analyte-detection technology is presented. The questions raised through this work are documented to provide new research directions for future work.

Chapter 7 offers the concluding remarks to summarize this dissertation work. Chapter 8 provides the supplementary information to support the main text chapters. Bibliography and Author Vita are provided following this chapter.

Chapter 2. BACKGROUND

As more and more disease diagnostic testing moves to POC due to several advantages compared to laboratory testing like portability, lower-cost, faster turn-around, and ease-of-use, there is an immediate interest in utilizing the instrumentation readily available at POC to aid in the process. Smartphones and wearables are some example device categories that have expanded beyond their primary application and into healthcare opportunities. Equipped with a myriad of sensors, computation resources and communication technologies, smartphones and wearable devices are being utilized for health monitoring applications like tracking exercises, metabolism, reproductive health, and fitness routines as well as health diagnostics. This chapter reviews the recent advances in using smartphones in health diagnostics applications. This chapter serves as a preface to this dissertation's contribution in extending the smartphone application by capitalizing on the core audio capabilities of the smartphone technology.

2.1 OVERVIEW OF SMARTPHONE-BASED HEALTH APPLICATIONS

In the last decade, the number of smartphone-based healthcare applications has exploded as evidenced by over 50k mobile health applications submitted to FDA[11]. Researchers around the world have reviewed these advances. Patrick *et al*. and Wang *et al*. offered respective review opinions in 2008 and 2009, respectively[12], [13]. Early applications used the smartphone cameras to perform biomedical imaging as outlined in the review by Xie *et al*[14]. In the last few years, the smartphone technology has rapidly evolved. Modern smartphones now feature high-resolution camera imagers (10 MP and higher), with excellent ISO and low-light performance, built-in flash, adaptive lenses, multiple cameras to assist with depth analysis, optical and electronic image stabilization and numerous software algorithms working to bring out a true image. These advances

are bound to improve and extend biomedical imaging applications of smartphones. For example, the research group of Professor Aydogan Ozcan at UCLA develops smartphone applications for fluorescence imaging and microscopy that can detect a single virus as well as perform automated cytometry[15]. Perhaps the most exciting proof of smartphone capabilities for health diagnostics was offered by the Sia group at Columbia where they used a smartphone with a custom dongle to diagnose HIV and Syphilis at the POC[16]. This work was widely featured in the media along with science editorials affirming that the field of smartphone-assisted diagnostics was of immediate relevance and impact.

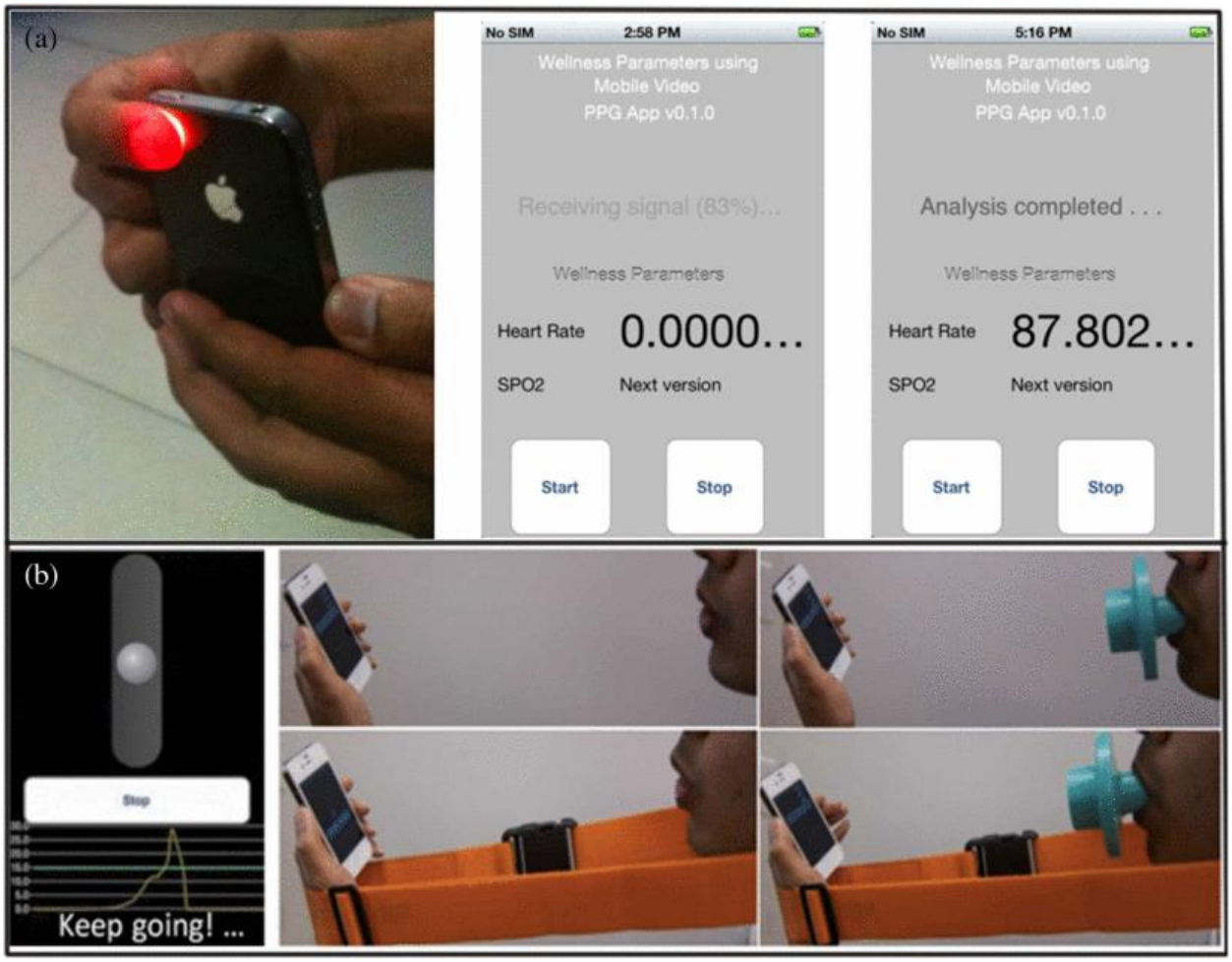

Figure 2.1. In-vivo health testing with smartphones (adapted from [17])

Broadly speaking, the application of smartphones for health diagnostics can be divided into two categories – in vivo testing and in vitro testing[17]. In vivo testing uses the built-in sensors to perform health monitoring. Figure 2.1 shows two examples that use the flash and camera to perform heart rate detection and repurposes the smartphone microphone to measure the lung capacity (spirometry)[18], [19]. Other applications have looked at capturing images of iris, forehead, and tongue etc. to perform basic health analysis. While these applications have made a significant impact in establishing the premise and versatility of smartphone-assisted health monitoring, more involved health testing requires additional sensors, electronics, and biochemical devices in the conjunction with the smartphone.

In-vitro testing with smartphones explores the application of smartphones beyond images and sounds. These applications are based on custom or off-the-shelf hardware and dongles paired up with a smartphone application. The hardware and dongles are equipped with specialized sensors that provide previously unattainable information such as temperature, ultrasound imaging as shown in the two examples in Figure 2.2[20], [21]. Some other examples include using smartphones in conjunction with simpler blood pressure monitors, glucose monitors and coagulation monitors[22]. Smartphones in in-vitro applications play a smaller role as a user-input and computational device for analyzing, storing and transmitting the data from the sensor hardware. Beyond simple health analysis and monitoring, smartphones are now being utilized to assist or perform complex biochemical assays for infectious disease testing and global health applications. These applications are reviewed in the following section.

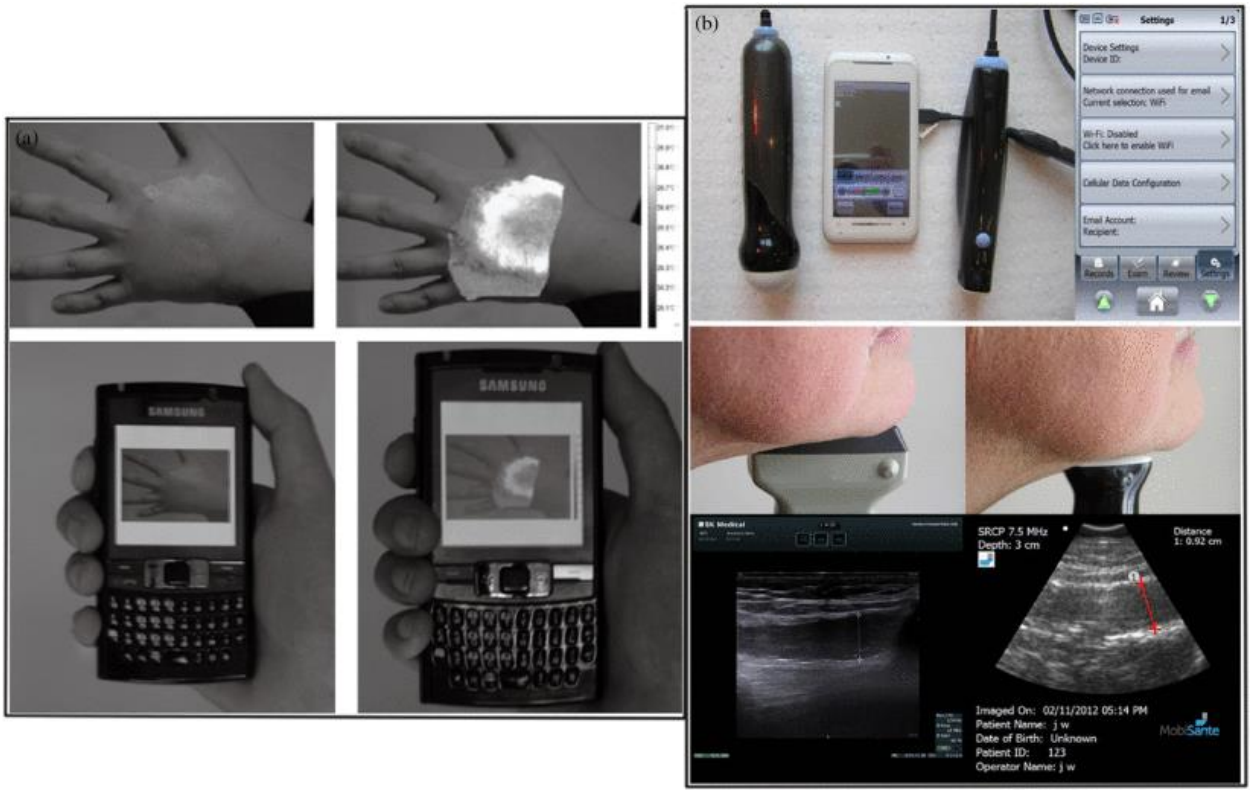

Figure 2.2. In-vitro health testing with smartphones (adapted from [17])

2.2 SMARTPHONES FOR INFECTIOUS DISEASE TESTING

POC infectious disease testing is complex and more involved than the simple health monitoring examples provided in the previous sections. A sample-in-result-out infectious disease test involves pre-processing of the patient sample, biochemical assay, and a readout. While it is not possible for smartphones to replace any or all the components of a complex infectious disease test, smartphones have the potential to augment the functionality of individual components of an infectious disease test. The following section reviews the requisites for smartphones that make them a suitable choice to support POC infectious disease testing, especially in low-resource settings.

2.2.1 **Assured criterion for medical diagnostics**

The World Health Organization (WHO) has pioneered the ASSURED criteria to guide the development of new POC diagnostics for infectious diseases[23]. The ASSURED criteria consist of the following features:

- **A**ffordable to use by those at risk of infection,
- **S**ensitive with minimum acceptable false negatives,
- **S**pecific with minimum allowable false positives,
- **U**ser-friendly even for those not trained in the art,
- **R**apid, to prevent loss-to-follow-ups.
- **E**quipment-free, and
- **D**elivered to those who need it and where they use it.

In addition to these, the same WHO bulletin recommended the need for data-linkage to support follow-up care and epidemiology public-health efforts.

2.2.2 **Smartphones and Assured criteria**

POC testing for infectious diseases is available in two formats – disposable, standalone tests (e.g. pregnancy test) and disposable cartridges with reusable readers (e.g. i-Stat®, Coaguchek®). In the standalone format, the test result is manually read out as the presence or absence of a colored line or spot on the strip. On the other hand, in the cartridge and+ reader format, the readout from the disposable cartridge is typically automatic, under controlled lighting conditions and is more accurate. The reusable readers are typically handheld or desktop-sized (i.e. portable) and may be used for simple control of the biochemical reaction on the disposable cartridge as well as readout of the result of the test using optical or electrical sensors. In many cases, the reader also provides

processing of the raw sensor data, displaying the result using a built-in user interface and communicating results to a remote location using a wireless or wired connection. The readers are usually battery-powered and can last a few hundred testing cycles[24], [25].

Modern smartphones are packed with sensors, actuators, displays, and computational prowess that can be repurposed to assist with POC diagnostic testing. The smartphone touchscreen is a more user-friendly and rich graphical display than what most commercial readers feature (monochrome LCD-type displays). The touchscreen can guide the user in performing the test through an easy-to-follow 'app'. The app introduces an array of novel interactions with the users. For example, the First Response ® Bluetooth pregnancy test app offers to play calm, soulful music while the user waits for the biochemical process to finish. Increasingly powerful camera modules and LED flash on smartphones can be utilized to detect the presence or absence of the line or spot on the disposable strip. The raw image data can be algorithmically processed to remove the signal from the ambient noise. The results of the test can be displayed through a user-friendly app and even shared with the doctor or the healthcare facility. Thus, a smartphone may serve as an ideal replacement for the readers used in POC disease testing. By offloading the instrumentation needed to perform and analyze a POC test to a smartphone, the overall disease testing can be made more affordable, user-friendly, deliverable, equipment-free, and optionally the health information can be more accessible for public health efforts. Therefore, smartphones may be the key to achieve the ASSURED criteria outlined for POC diagnostic tests. The challenges in realizing this vision of smartphone-powered POC diagnostic tests are outlined in Section 2.3.

2.2.3 **Example applications**

There have been numerous examples of using smartphones to assist with POC diagnostic testing. Many of these applications have been reviewed recently by Xu *et al* and Vashist *et al*[17], [22].

The selected examples reviewed below are especially relevant to this dissertation work as they utilize the smartphone audio capabilities in performing rapid diagnostic testing.

A major breakthrough in miniaturization of instrumentation needed to perform a complex enzyme-linked immunosorbent assay (ELISA) was presented by the Sia group at Columbia[16]. The team developed and tested a novel smartphone dongle (Figure 2.3) capable of replicating the mechanical, optical, and electrical functions of a lab-based multiplexed ELISA for syphilis and HIV. The major challenge with such an integrated design is limited electrical power availability. The team made a conscious compatibility design choice to employ the 3.5 mm headphone jack commonly found on all non-Apple smartphones (most used in developing countries) to provide electrical power and for data communication. The power provided by the headphone is just enough to drive the audio drivers on earphones (<100 mW at 1V), so it was an engineering feat to squeeze all the electrical power to perform control and detection on the plastic microfluidic card conducting the ELISA assay with minimal manual intervention. The actual ELISA assay was also optimized to run on a disposable plastic card with minimum power needs and manual intervention.

This low-power engineering feat was achieved by replacing the active, electrical pumps by a passively-powered vacuum pump to perform the microfluidic reagent flow control and hijacking the audio from the headphone jack to extract electrical power as well as used for unidirectional data communication as shown in Figure 2.3 (B)[26]. DC power was harvested by rectifying a 19 kHz signal on the differential audio lines of the headphone jack. The DC power was used by LED and photodiode pairs to measure the optical density (OD) measurement of the silver enhancement ELISA. The photodiode output was converted to a frequency-shift keyed (FSK) signal by a low-power microcontroller and transmitted via the microphone line on the headphone jack. The smartphone app processed the received signal and displayed the result to the user. The app also

guided the user in performing the diagnostic test. In addition to demonstrating an integrated solution that utilizes the ubiquitous audio capabilities of a smartphone, this work could be considered as a pioneering step towards marrying microfluidics with advances in consumer electronics. This dissertation work uses the audio tones from smartphones for a more direct flow control and analyte detection than shown in this study.

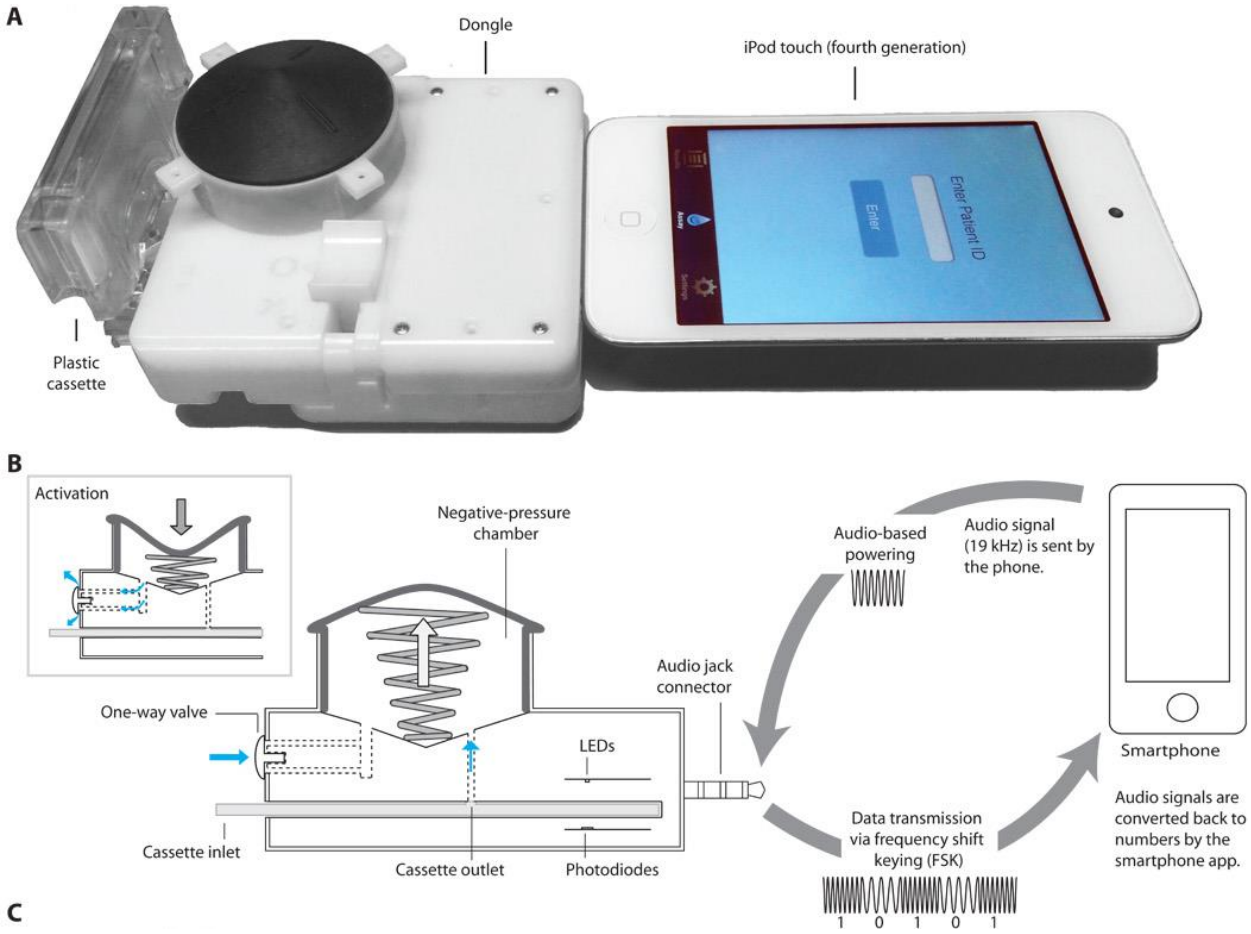

Figure 2.3. Smartphone dongle for syphilis and HIV testing uses audio jack for power and communication (adapted from [16])

Another major bottleneck towards mass deployment of POC diagnostic devices is sample preparation. The team of engineers and scientists from The Yager group at the University of Washington have invented the sample preparation technique of Audiolyse[9] as shown in Figure

2.4. Unlike ELISA, which detects the protein or antibody associated with the pathogen of interest, nucleic acid tests produce a positive result when the DNA or RNA of the pathogen is present in the sample. Such tests require the sample preparation step of cell lysis where the cell membrane is mechanically, electrically or chemically stressed and ruptured to release the fluid containing the DNA or RNA. The fluid, called lysate, is then purified and processed using an amplification assay (like polymerase chain reaction) to create millions of copies of the pathogenic DNA that can be easily detected using appropriate signal transduction chemistry. The technique of Audiolyse is a mechanical approach and does not require any special reagents that could complicate downstream amplification. The portable device is simply an electric coil wound around a plastic holder for a lysis tube. A magnetic field was generated when a sinusoidal signal (30 Hz in this case) from a smartphone was applied to the coil. The field caused a magnetic sphere inside the lysis tube to spin. The fast-spinning sphere physically broke even the most hardy cells like *Staphylococcus epidermidis* and *Mycobacterium marinum*. The team demonstrated a 20-60% lysis efficiency for the audio-powered lysis device compared to a benchtop bead beater, while costing substantially less and being more power efficient.

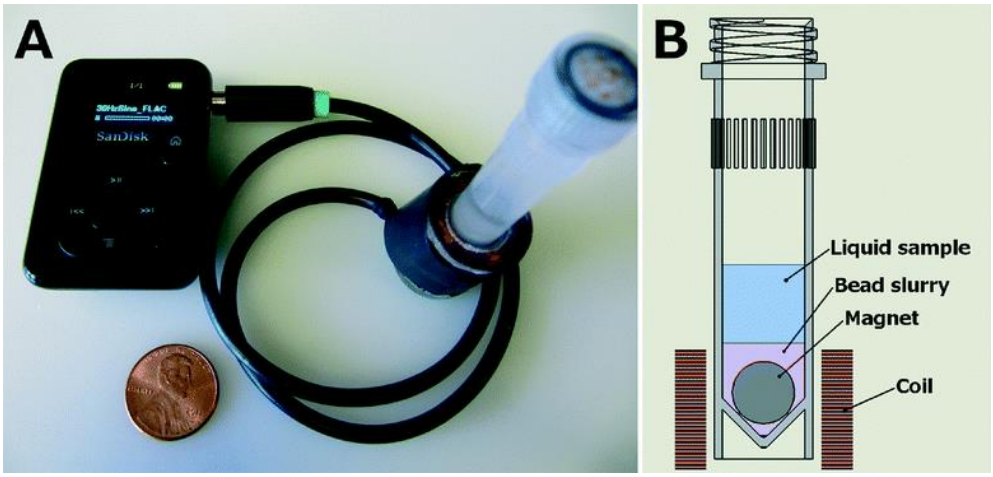

Figure 2.4. The Audiolyse device for sample preparation (adapted from [9])

2.2.4 **Opportunity to innovate**

Both the work described in the previous section highlight the unique opportunities to utilize the audio capabilities of the smartphone with POC diagnostics devices. The smartphone dongle proposed by the Sia group utilizes the audio because of the universal, smartphone-agnostic, headphone jack. The underlying physics or chemistry on the microfluidic card does not rely on the audio implementation. The dongle could be readily adapted micro USB or the Apple lightning connector with minimal design changes and would be potentially beneficial because of the increased available power as well as the simplified serial communication interface. The point is that the dongle is not dependent on any audio-specific technology or physics but rather using audio as a means of providing electric power, which is still a commendable engineering and scientific achievement. On the other hand, the performance of the Audiolyse device are is inherently dependent on the audio frequency and magnitude. This is the same design philosophy used in this dissertation. The science of the microfluidic devices presented here for flow control and analyte detection in POC diagnostic devices centers around ‘audio’ via the resonance frequency. This approach provides unique integration opportunities that were not present in an audio-agnostic microfluidic approach. For example, the vacuum pump used in the smartphone dongle could be replaced by audio-responsive pumps developed in this dissertation. Optical density (OD) measurements using LEDs and photodiodes could be replaced by analyte-mediated changes in fluid properties detected by the shift in resonance frequency. Granted, this would require a major re-work of the silver enhancement assay chemistry, but the key takeaway is that by intimately merging the microfluidics with the audio technology, POC diagnostics can be made more compact, integrated, and affordable.

2.3 CHALLENGES WITH SMARTPHONE-BASED HEALTH TESTING

Despite the unique boost that smartphones bring in achieving the ASSURED mandate for medical diagnostic devices, there are also unique challenges that should guide the research and development of next-generation POC diagnostic devices.

2.3.1 **Device-to-device variability**

Smartphones vary with model, generation, and manufacturer. This choice is a good thing for consumers because it provides them options from which to choose from based on individual needs. However, for diagnostic device makers hoping to capitalize on the ubiquitous nature of smartphones, it a major challenge. For example, the maximum audio power output (volume) is dependent on the audio amplifier on the smartphone. Inexpensive phones often provide much less power to the earphones than high-end phones[26]. Thus, it is plausible that the smartphone dongle presented by the Sia group supports some phones and not many others. Besides audio power, like everything in technology world, the camera performance varies significantly between smartphones. The variability in audio power in also present in camera when used as a readout. Device model and generation can also affect the sensors and ports available. For example, Apple's 'bold' design to remove the headphone jack from the sixth generation iPhone triggered the infamous craze to remove the only universal I/O port on smartphones. As a smartphone-based diagnostic device maker, being at the forefront of the smartphone industry trends is a necessity to guide design decisions.

2.3.2 **Battery consumption**

The smartphone dongle presented by the Sia group (Section 2.2.3) theoretically works for about 41 cartridge 'runs' before the smartphone battery (2300 mAh capacity) is depleted. This is

significantly small than handheld readers that are rated to a couple of hundred reads. Batteries remain the area of heaviest investment and interest in the smartphone industry, so the battery capacity is expected to continue its upward trend. For any smartphone-based health diagnostic device, the requirement for the number of runs would depend on whether the test is being performed by the patient at home or by a clinician in an office setting. The challenge becomes increasingly relevant when it is expected that the same smartphone is used to perform many tests, like in a doctor's office. In such scenarios, diagnostic device makers should consider providing a backup battery case that augments the available battery capacity and reduces downtimes for recharge. In addition to added battery capacity, a custom case may also offer handy storage for consumables and supplies. However, a case is not a solution for diagnostic devices connected to the charging ports (USB-C, lightning) as the battery cases recharging utilizes the same port.

2.3.3 **Ambient and user-dependent challenges**

Beyond the smartphone device variability, the dissimilarity between testing setups introduces differences from lighting conditions, angles, orientations and other ambient effects. This challenge is especially relevant in diagnostic applications that involve image capture on a smartphone. The software normalization for these effects using computer vision and machine learning techniques. In addition, diagnostic device makers include fiducial marks on the cartridges and use special jigs and custom lighting condition to reduce image-to-image variability. Some of these approaches are outlined in detail in Prof. Ozcan's review[15].

2.3.4 **Security and HIPAA compliance**

As with many connected devices and services, there is an increased interest in data security and privacy. As a diagnostic device maker, care needs to be taken to ensure patient privacy is

maintained. The guidelines recommended that patient-specific information (name, demographics and test results) is encrypted before being saved locally on the device or any remote database. Modern smartphones routinely perform the encryption task, so there are no technical barriers to implementation. In the rare scenario that the smartphone to diagnostic device connection is wireless, like the Bluetooth pregnancy device, the communication needs to be encrypted at both ends. If encryption is not feasible due to limited computational resources on the diagnostic devices, a short-range communication like NFC should be used to prevent sniffing of patient-specific information.

2.3.5 **Uncertain regulatory framework**

As indicated by the number of pending regulatory applications in the research article by McInerney[11], FDA may be playing catch up as smartphone technology continually creates new opportunities for the future of health testing. The FDA guidelines for mobile medical applications were last updated in 2015 and may not have kept pace with or predicted the fast-evolving smartphone ecosystem. In addition to a moving target, mobile health applications, due in part to the novelty of the field and in part to the challenge of promulgating regulations on such a diverse, ever-changing platform, are harder to regulate than conventional medical devices. Any diagnostic device maker developing a smartphone app for medical diagnostics should be aware that there is unknown risks and uncertainties associated with the regulatory process. To reduce that, FDA recommends getting involved at an early development stage rather than when the technology is ready for testing.

Chapter 3. MICROFLUIDIC RESONANT CIRCUITS

This chapter reviews the classic electric-hydraulic analogy and introduces the theory, design, modeling, and fabrication of series and parallel microfluidic resonant circuits.

3.1 ELECTRIC-HYDRAULIC ANALOGY

Circuits comprising of resistors (R), inductors (L) and capacitors (C) have been the workhorse of electrical engineering. RLC circuits exhibit series and parallel resonant behavior which finds application in practical devices like radio tuners and notch filters, respectively. The electric-fluidic analogy, first described by Sir Oliver Lodge in the early 1900s[27], allows translation of the same rich behavior to hydraulics. Electrical voltage and current is considered analogous to hydraulic pressure and flowrate respectively. A simple microfluidic channel filled with a viscous, incompressible fluid can be thought of as a combination of a resistor (R) and inductor (L) as shown in Figure 3.1. The resistor represents the internal friction due to the viscosity of the fluid, and the inductor exhibits represents the inertial reluctance of the dense fluid to changes in motion. The fluidic counterpart of an electrical capacitor (C) is a deformable feature, like a bubble or a diaphragm, that provides transitory fluid storage and is also known as elastic compliance[28]. Hence, circuit elements needed to create common passive circuits, like RLC circuits, are present in microfluidics.

In order to create net flow, harmonic (AC) flow needs to be rectified to create steady (DC) flow. Channel features that introduce flow direction preference, such as diffuser and weir valves, are used for this purpose. These elements are the microfluidic equivalents of an electrical diode.

Resonance is a phenomenon that occurs in physical systems with orthogonal storage modes. In electrical systems, these orthogonal modes are capacitive and inductive. As the frequency of the

voltage source increases, the capacitive impedance to the current decreases non-linearly while the inductive impedance increases linearly. Resonance occurs at the frequency where the capacitive impedance is equal but opposite to the inductive impedance resulting in minimum impedance to the voltage source. This is the series resonance. The opposite of series resonance is parallel resonance where the admittances related of the capacitor and inductor cancel and result in a maximum impedance to the voltage source. Both series and parallel resonance have been utilized in electrical engineering to create circuits that have found application in radios, tuners and even in the modeling of the transatlantic communication line. Due to the myriad uses of resonant RLC circuits in electrical engineering, translating the resonance phenomenon to microfluidics was a natural next step.

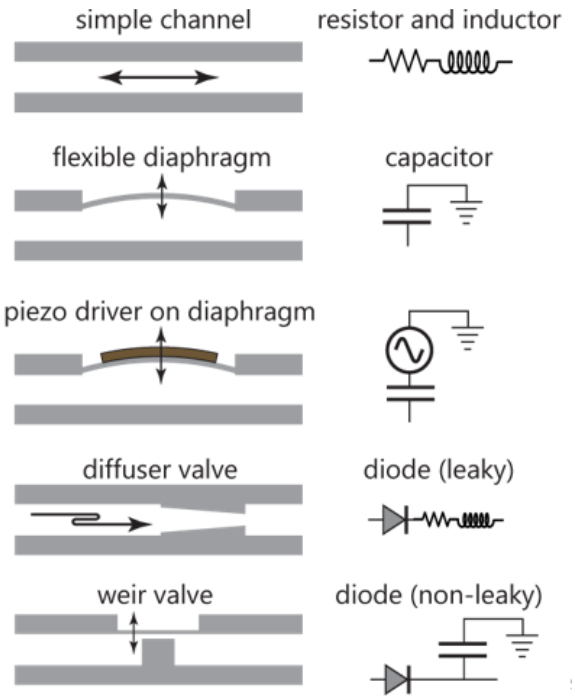

Figure 3.1. Microfluidic equivalents for common electrical circuit elements

The hydraulic-electric analogy has been leveraged to make microfluidic devices that find application in concentration gradient generation, series dilution, flow control and sample analysis

(review in [29]). A sub-class of these microfluidic circuits utilize a harmonic pressure source, like a voice-coil or a piezo buzzer, to create AC flow in the channels, which can be tuned through the frequency of the pressure source. This concept of frequency-tuned flow was introduced by the groups of Begley and Landers who utilized simple microfluidic channels (RL) with added deformable features like capacitors (C) and valves (diodes) to create pumps that can be activated by simply matching the actuation frequency to the series resonance frequency of the RLC network[30]–[32]. This dissertation work is built on the concept of extending the applications to include multi-channel RLC networks and to increase the operating frequency range such that multiple channel resonances can fit without overlap in the frequency response. The overall goal is to realize microfluidic pumps that can be controlled with everyday audio devices like an iPhone or mp3 player[33].

3.2 MICROFLUIDIC RESONANT CIRCUITS

This section outlines the theory, modeling, and design of microfluidic resonant circuits exhibiting series and parallel resonance phenomenon. Figure 3.2 shows an example resonant microfluidic device and its analogue electrical circuit representation. The piezo buzzer pressure source can be represented as a series combination of a sinusoidal pressure source (P_{AC}) and a capacitor accounting for the composite compliance of the piezo buzzer and the flexible diaphragm (C_p), to which the piezo buzzer was affixed. Using the classic electric-hydraulic analogy, the viscous drag and inertance of the fluid in the channel were modeled as a series connection of resistance and inductance, respectively. The broad, circular part of the channel (Figure 3.2 inset) was covered with a deformable Rohaglas film that flexes under pressure to store fluid, and therefore, was represented as a capacitor (C_c). The other side of the capacitor (C_c) was open to air (pressure reference), so it was considered connected to ground (electrical reference) in the electrical circuit

representation. After filling the device, the inlet left to the piezo buzzer was plugged (represented electrically as open-circuit). The inlet far from the piezo, on the right, may be left open to air (represented as a connection to ground - dashed wire in Figure 3.2).

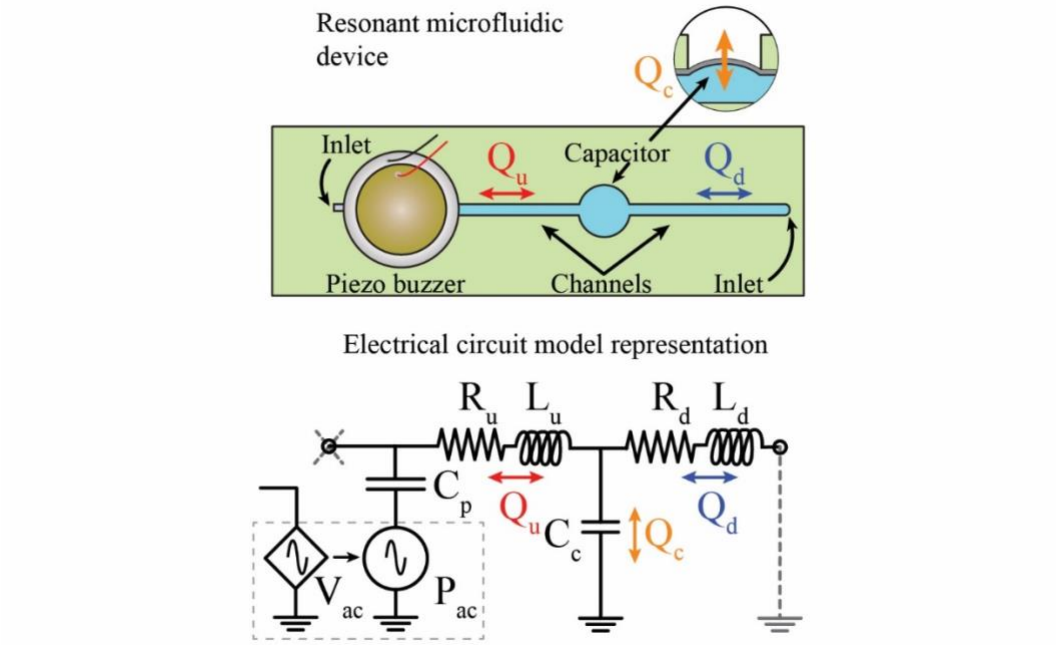

Figure 3.2. Schematic and electrical representation of an example microfluidic resonant circuit

Figure 3.2 **Extended Caption**: The piezo buzzer served as the on-chip pressure source and created AC flow in the upstream (Q_u), downstream (Q_d) channels and the broad compliant part separating the two channels, a capacitor (Q_c). Below the device schematic is the electrical circuit model representation with the piezo buzzer replaced by the AC pressure source and a series capacitor (C_p). The voltage (V_{ac}) to pressure (P_{ac}) transduction does not introduce a phase shift due to low-frequency operation (< piezo buzzer resonance, kHz), as is the case here[34], [35]. The channels were represented by a series connection of resistor and inductor, and the flexible diaphragm was shown as the capacitor (C_c). The inlet left of the piezo buzzer was plugged after filling the device. In the circuit model, this was depicted by a cross mark indicating open circuit, or no flow. The downstream inlet was left open to air and hence shown as a connection to the ground (dashed wire). The frequency-dependent resistance and inductance values (R, L) were derived using

the exact impedance solution of the Navier-Stokes equation for harmonic flow[36]. Capacitances (C) were estimated by fitting experimental data to electrical circuit model predictions. Both of these techniques are detailed in the Sections 3.3.1 and 3.3.2. The circuit can be solved for the AC flowrates at different actuation frequencies.

3.2.1 **Series resonance**

Figure 3.3 shows the frequency response of the flow magnitude and phase provided by the electrical circuit model from Figure 3.2. $\boldsymbol{f_o}$ is the series resonance frequency associated with the capacitor connected to the piezo buzzer (C_p) and sum-total inductance of the channels and is given by

$$f_o = \frac{1}{2\pi\sqrt{(L_u + L_d)C_p}}. \qquad (3.1)$$

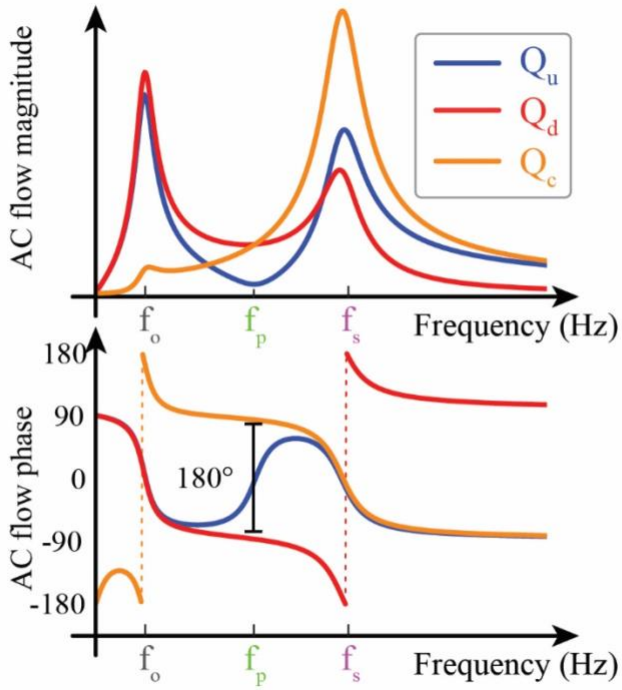

Figure 3.3. Frequency response of AC flow magnitude and phase for the example microfluidic resonant circuit

Since C_p and the sum of the inductances are large, small changes in inductance realized through changing the channel length alone does not considerably affect the resonance frequency $\boldsymbol{f_o}$. While $\boldsymbol{f_o}$ may have limited design appeal, the flow magnitude and phase relationship are worth noting. At this frequency, the upstream flowrate (Q_u, red arrow in device schematic in Figure 3.4) and downstream flowrate (Q_d, blue arrow) are almost equal and in-phase, which results in very small flow through the capacitor ($Q_u + Q_c = Q_d$; $Q_u \sim Q_d$ i.e. $Q_c \sim 0$).

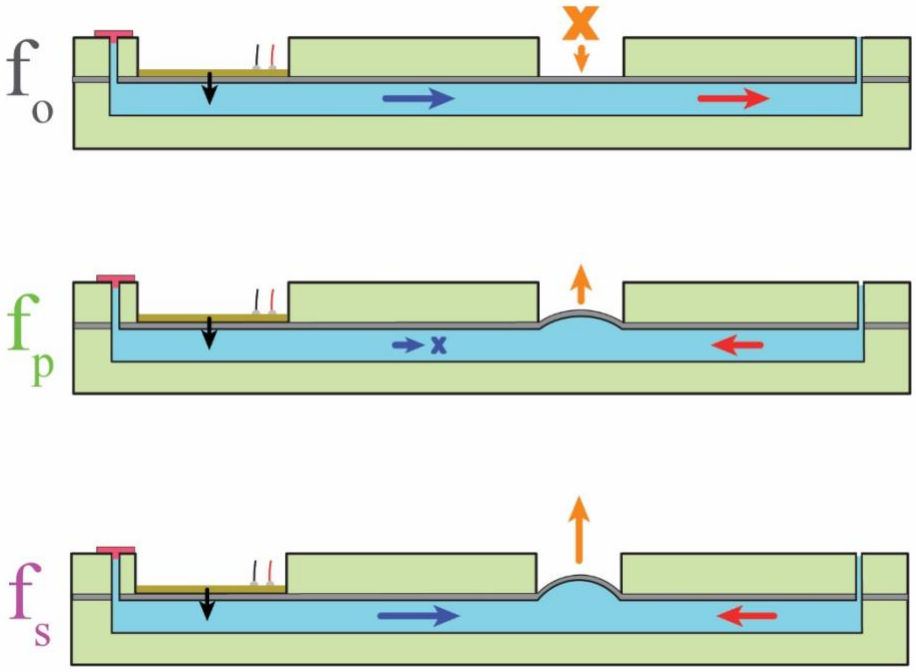

Figure 3.4. Flow directions in upstream and downstream channel at resonance frequencies

The series resonance frequency, $\boldsymbol{f_s}$, is commonly associated with resonance due to the peak in the flow magnitude, and it was the focus of frequency-selectable pumps in the previous work [30], [32]. This frequency depends on both the upstream and downstream channel impedances and the capacitor (C_c). The analytical expression for $\boldsymbol{f_s}$ is complex and includes the resistance and inductance of both upstream and downstream channels and the capacitances of the piezo buzzer (C_p) and capacitor-diode (C_c). Unlike the parallel resonance, at this series resonance frequency,

the upstream and downstream flowrates (blue and red arrows, respectively) add constructively to make up the capacitor flowrate (yellow arrow), as shown in the lower device schematic in Figure 3.4 (for $\boldsymbol{f_s}$).

3.2.2 **Parallel resonance**

The next frequency point of interest is the parallel resonance $\boldsymbol{f_p}$ – the valley in the frequency response of the upstream flowrate (Q_u). Here, the flowrate downstream (red arrow) is nearly equal in magnitude and opposite in phase to the flowrate in the capacitor (yellow arrow), as illustrated in the middle device schematic in Figure 3.4 (for $\boldsymbol{f_p}$). Conservation of mass requires that the upstream flowrate approach zero under this condition. Electrically, this results from the parallel combination of the downstream inductor (L_d) and the capacitor (C_c) producing a maximum impedance to upstream flow at $\boldsymbol{f_p}$. Not surprisingly, the parallel resonance frequency is dependent only on these two elements and is simply given by

$$f_p = \frac{1}{2\pi\sqrt{L_d C_c}}. \qquad (3.2)$$

Figure 3.4 shows that even simple microfluidic resonant devices exhibit complex behaviors in their magnitude and phase responses. While these responses are fully-expected based on the electrical circuit models, there has been a basic quantitative characterization of the magnitude response, and the phase relationships have not been measured prior to this dissertation work. In Chapter 4, two independent methods to measure magnitude and phase of the AC flow are presented. The measurements validate the complex behaviors predicted by the electric-hydraulic analogy.

3.3 MODELING OF MICROFLUIDIC RESONANT CIRCUITS

In this dissertation work, AC flow is represented as back-and-forth motion of an incompressible fluid. The physics does not involve standing or traveling pressure waves as in Helmholtz resonators[37] or acoustofluidics[38]. While fluidic systems have additional complexities that do not exist in electrical systems (e.g., no-slip boundary condition, see below; secondary flows at transitions[39]), the simplest connectivity between components was used to construct equivalent electrical circuit models that can be analyzed using undergraduate-level circuit methods.

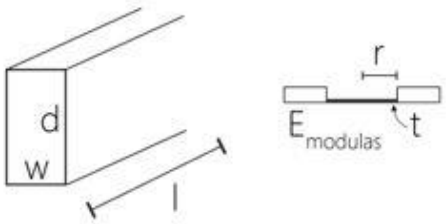

Figure 3.5. Simplified expressions for microfluidic equivalents of common electrical circuit elements

3.3.1 **Resistance and inductance**

Simplified expressions have been reported for fluidic resistance and inductance for flow in rectangular channels. For a rectangular channel, as shown in Figure 3.5, Resistance and inductance can be estimated as

$$R = 12\mu l/(d^3 w)\,, \qquad (3.3)$$

$$\text{and } L = \rho l/(dw)\,. \qquad (3.4)$$

where l is the channel length, w and d are the channel half-width and half-height, ρ is the fluid density, and μ is the fluid dynamic viscosity[30], [36], [40]. Collino, *et al* noted that the basic expressions do not include the Womersley effect, because of which operation at higher frequency

may be impacted due to rapidly increasing viscous effects compared to the inertial effects [32]. Thus, for all models presented in this dissertation work, the exact analytical expressions for R and L in rectangular channels driven by rectilinear sinusoidal oscillations, which quantitatively accounts for the Womersley effect in both R and L were used. R and L are the real and imaginary components, respectively, of the complex impedance (Z) given by[36]

$$Z = \frac{ul\pi^2}{32b^4}\left[\sum_{n=0}^{\infty}\frac{1}{(2n+1)^2 f^2}\left(\frac{a}{b}-\frac{\tanh(f.a/b)}{f}\right)\right]^{-1}, f = \sqrt{\left(ib\sqrt{\frac{\omega}{\nu}}\right)^2+\frac{(2n+1)^2\pi^2}{4}}, \quad (3.5)$$

where ω is the frequency in radians, and ν is the fluid kinematic viscosity. Unlike the simplified expressions, both R and L have a modest dependence on driving frequency[41], [42].

3.3.2 **Capacitance**

Flexible diaphragms serve as capacitors by accepting and expelling fluid in response to pressure oscillations. A simplified expression for capacitance is provided in literature as[30]

$$\mathrm{C} = 16r^6/3\mathrm{E}t^3, \quad (3.6)$$

where *r* is the radius of the (circular) diaphragm (as shown in Figure 3.5), *E* is the elastic modulus of the diaphragm material, and *t* is the thickness of the diaphragm. Prior work in frequency-tuned flow suggested that the simplified expression for capacitance in equation 3.6 are not accurate for microfluidic implementation[32]. Therefore, the capacitance was determined by fitting the RLC circuit model to data using C as a fitted parameter and compared between experiments to verify consistent fitted values. This approach was used to create a library of capacitance with radii varying from 2 mm to 4.5 mm, thicknesses from 0.254 mm (10 mil) and 0.381 mm (15 mil) and made of Rohaglas and Mylar material (Table 3.1).

Table 3.1. Library of fitted diaphragm capacitance (bold marks commonly used values in this work)

Radius (mm)	**Material**	**Thickness (mm)**	**Capacitance (mm^3/kPa)**
2.0	Rohaglas	0.254	0.00083 ± 0.0002
	Rohaglas	0.381	0.00021 ± 0.0001
	Mylar	0.254	0.00019 ± 0.0005
	Mylar	0.381	0.00012 ± 0.0002
2.5	Rohaglas	0.254	0.00103 ± 0.0002
	Rohaglas	0.381	0.00081 ± 0.0001
	Mylar	0.254	0.00076 ± 0.0002
	Mylar	0.381	0.00064 ± 0.0004
3.0	**Rohaglas**	**0.254**	**0.00230 ± 0.0017**
	Rohaglas	0.381	0.00153 ± 0.0011
	Mylar	0.254	0.00149 ± 0.0022
	Mylar	0.381	0.00132 ± 0.0019
3.5	**Rohaglas**	**0.254**	**0.00748 ± 0.0022**
	Rohaglas	0.381	0.00622 ± 0.0031
	Mylar	0.254	0.00543 ± 0.0032
	Mylar	0.381	0.00452 ± 0.0013
4.0	**Rohaglas**	**0.254**	**0.01560 ± 0.0095**
	Rohaglas	0.381	0.01145 ± 0.0073
	Mylar	0.254	0.01092 ± 0.0082
	Mylar	0.381	0.00914 ± 0.0095
4.5	**Rohaglas**	**0.254**	**0.02760 ± 0.0130**

	Rohaglas	0.381	0.02201 ± 0.0121
	Mylar	0.254	0.01929 ± 0.0102
	Mylar	0.381	0.01745 ± 0.0080

While single-sided capacitors, like that shown in Figure 3.4, remain the most common capacitor in this dissertation work, double-sided capacitors were also created by allowing the diaphragm to flex through the cutout on both the top and the bottom of the channel. This change doubled the capacitance and improved the performance of an optical sensor (to be discussed later) by creating a lens-effect[43]. When the weir was added under a single-sided capacitor, the capacitance was reduced to half and the combination results in a fluidic diode[44].

3.3.3 **AC motive**

A piezoelectric disk attached to a circular diaphragm created a mechanical bimorph that allowed fluid to be driven with sinusoidal oscillations. The driver was represented as a pressure source (P_{AC}) acting through a capacitor (diaphragm, C_p). P_{AC} and C_p were determined by fitting model predictions to experimental observations across a range of device designs to ensure a consistent fit.

Table 3.2. Values for fitted piezo buzzer capacitance and pressure

Radius (mm)	**Mouser Part#**	**C_p (mm^3/kPa)**	**P_{AC} (kPa)**
5 mm	81-7BB-10-6L0	0.0547 ± 0.005	0.05 ± 0.01
10 mm	81-7BB-20-6L0	0.1320 ± 0.004	0.20 ± 0.03

3.3.4 **AC flowrate**

Electrical charge is analogous to molecules of fluid volume, and current is analogous to volumetric flowrate. However, unlike electrical circuits, fluidic circuits are complicated by the non-uniform flow profile due to the no-slip boundary condition at channel walls[45]. In addition, oscillating (AC) flow deviates from the familiar parabolic flow profile of steady (DC) flow. At sufficiently high oscillation frequency, flow in the channel center assumes an approximately uniform "plug-like" oscillation[36], [39], [46], and velocity gradients are largely confined to a thin Stokes layer near the walls (Stokes layer thickness, $\delta_{AC} = (\nu/\omega)^{1/2}$).

The plug-like oscillating flow near the channel center was visualized using tracer particles. Under the conditions tested here, the plug-like flow occupied the majority of the channel cross-section; e.g., for 100 Hz, d=0.125 mm, and ν=0.01 cm^2/s, the plug-like flow occupies $2d - 2\delta_{AC}$ = 170 um of the channel centerline region (70% of total channel depth, $1 - \delta_{AC}/d$), and the region expands as frequency increases[39]. Thus, measurement of particle streaks near the channel center was not sensitive to error in placement of the measurement location.

Oscillation in the plug-like flow near the centerline follows $X_{cent}(t) = \frac{1}{2} \cdot S_{cent} \cdot \sin(\omega t)$, where S_{cent} is the measured particle streak length[39], and centerline AC velocity follows $V_{cent}(t) = dX_{cent}/dt = \frac{1}{2} \cdot S_{cent} \cdot \omega \cdot \cos(\omega t)$. Calculating AC flowrate from the product of centerline AC velocity (V_{cent}) and channel cross-sectional area ($2w \cdot 2d$) would overestimate the flowrate due to since it does not account for slower flow near channel walls. An analytical relation for the magnitude of center-to-mean velocity for oscillating flow in a rectangular channel[40] was applied to obtain the mean AC velocity, V_{mean}. The magnitude of AC volumetric flowrate (Q) was calculated as $2w \cdot 2d \cdot V_{mean}$, which is the direct fluidic analogy to electrical current reported by the circuit model. The center-to-mean velocity ratio for sinusoidal pressure driven flow in rectangular channels was

given by O'Brien[40] (note that the original reference contained an error – the second tanh term in the denominator was mistakenly printed as sech – this is corrected below)

$$\frac{W^*(0,0)}{\{W^*\}} = \frac{1-2\sum_{n=0}^{\infty}(-1)^n p_n^{-1}[\mathrm{sech}(\zeta_n)+\mathrm{sech}(\mu_n)]}{1-2\sum_{n=0}^{\infty} p_n^{-2}\left[\frac{\tanh(\zeta_n)}{\zeta_n}+\frac{\tanh(\mu_n)}{\mu_n}\right]}, \quad (3.7)$$

$$p_n = \frac{2n+1}{2}\,\pi, \quad (3.8)$$

$$\zeta_n = \sqrt{p_n^2\left(\frac{w}{d}\right)^2 + \frac{i\omega d^2}{\nu}}, \quad (3.9)$$

$$\text{and } \mu_n = \sqrt{p_n^2\left(\frac{d}{w}\right)^2 + \frac{i\omega d^2}{\nu}}, \quad (3.10)$$

where w and d are the channel half-width and half-height, respectively, ω is the frequency in radians, and ν is the fluid kinematic viscosity. V_{cent} was calculated from measured particle streak lengths, and the magnitude of AC volumetric.

3.3.5 **Notation and units**

Fluidic analogies to electrical components are presented with consistent units: AC Pressure (P, kPa), AC Flowrate (Q, mm^3/s), Impedance (Z, kg/mm^4/s), Capacitance (C, mm^3/kPa), Resistance (R, kPa·s/mm^3), and Inductance (L, kg/mm^4).

3.4 FABRICATION OF MICROFLUIDIC RESONANT CIRCUITS

The schematic of a microfluidic resonant device is shown in Figure 3.6. Devices were fabricated by stacking laser-cut acrylic (McMaster Part# 8540K171, 1.5mm thickness) and Rohaglas parts (Sabic Polymershapes Seattle WA, Part#76017130-C, 0.254 mm in thickness), and pressure bonding them with PDMS tape (Adhesives Research ARclad 7876). Channels were defined as features in the acrylic part (light yellow). Channel depth was the same as the acrylic thickness (1.0 – 3.0 mm), and the channel width was kept fixed

at 0.8 mm for all devices. The channel lengths and capacitor sizes were varied as per resonance frequency requirements. The channels were capped by the deformable Rohaglas or Mylar film (yellow) on one or both sides (single or double-sided capacitor). A stiff acrylic cap was added to the top and bottom to stiffen the channels, except that circular areas above the diaphragm regions (piezo buzzer diaphragm and capacitor diaphragm) were cut out of the acrylic to allow the diaphragms to flex. The flexing allowed transient fluid storage, much like an electrical capacitor. The piezo buzzer (Mouser.com part# 81-7BB-20-6L0, 10mm radius) was affixed to the large diaphragm of the same size using the PDMS tape. Thus, the annulus capacitance observed in prior work[32] was not present here. Inlets were simply defined as holes (1 mm diameter) in the top (cap) acrylic layer (

Figure 3.6). Devices were filled with a glycerol solution (dynamic viscosity = 1.024 mPa·s[47], density = 1.05 g/mL) with suspended polystyrene fluorescent beads (Duke Scientific 5 μm nile blue, density = 1.05 g/mL). After filling the devices, the inlet close to the piezo buzzer was plugged using thick tape (scotch magic tape). Depending on the experiment goal, the inlet connected to the downstream channel were plugged or left open to the air, as shown in Figure 3.2.

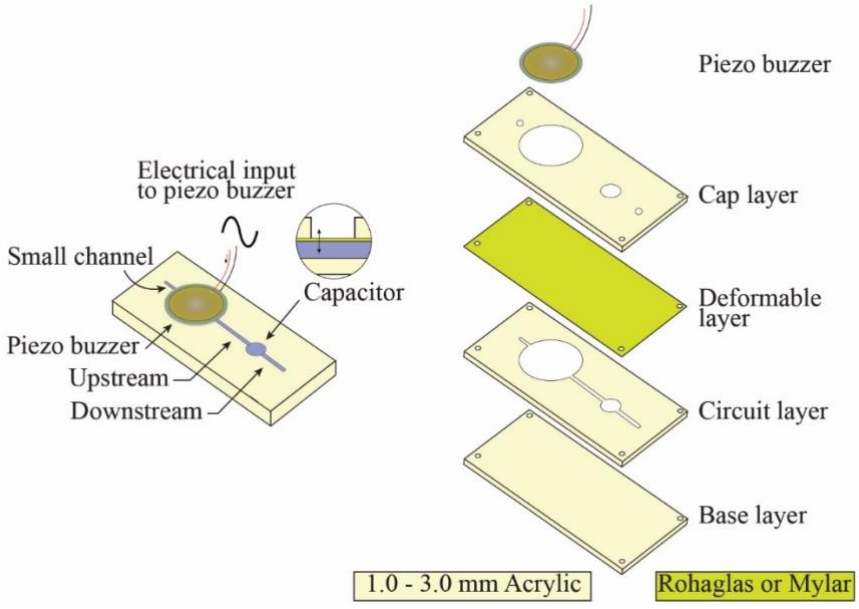

Figure 3.6. Fabrication of microfluidic resonant circuits

Chapter 4. ELECTRICALLY-INSPIRED FREQUENCY CHARACTERIZATION TOOLKIT

Frequency characterization of electrical RLC circuits is represented by pairs of current magnitude and phase (called Bode plots). However, prior to this dissertation work, microfluidic resonant RLC circuits have been characterized only by the AC flow magnitude measurements[30], [32]. While this was adequate to introduce the concept, flow magnitude alone provides only partial validation of the classic electric-hydraulic analogy. Hence, to further corroborate the analogy, this chapter presents the analytical tools and techniques for simultaneous measurement of both AC flow magnitude and AC flow phase applied to example series and parallel resonant microfluidic devices. This characterization technique is referred to as AC analysis in electrical engineering. In the continued spirit to derive inspiration from electrical engineering techniques, the Fourier and Step Analysis methods were developed for applications in microfluidics. Fourier analysis is more suitable for complex multi-channel geometries and provides flow magnitude at the specific frequencies of interest. Step analysis is capable of rapid measurement of the resonance frequency and is readily applicable to end devices where resonance frequency may be measured for quality control or sensing purposes. In the process of translating these three characterization techniques to microfluidic domains, it was demonstrated that the classic electric-hydraulic analogy advances beyond the microfluidic analogues for voltage, current and circuit components to functional properties, like resonance, linearity, and superposition.

4.1 AC ANALYSIS

This chapter details the two independent methods for assessing the magnitude and phase of harmonic flow in microfluidic networks with deformable features: 1. a custom stroboscopic epifluorescence setup for measuring flow in the channel via bead tracking, and 2. a novel diaphragm lens optical vibration sensor for estimating flow in the deformable feature. The results show that the magnitude and phase frequency responses quantitatively match model predictions for series and parallel resonant RLC microfluidic devices. In this chapter, the tools and techniques for simultaneous measurement of flow magnitude and phase in microfluidic resonant devices are presented.

4.1.1 **Device fabrication and filling**

Resonant microfluidic devices were fabricated using the materials and methods described in Section 0. The channel lengths and capacitor sizes used in this work were the following: Series resonant device – Upstream: 18 mm, Downstream: not present, capacitor radius: 3.0 mm. Parallel resonant device – Upstream: 4.2 mm, Downstream: 24 mm, capacitor radius: 4.5 mm. The channel connecting the piezo buzzer and the left inlet was short (2 mm) compared to other channels. All the channels were 1.5 mm deep and 0.8 mm wide. Devices were filled with a glycerol solution (dynamic viscosity = 1.024 mPa·s[47], density = 1.05 g/mL) with suspended polystyrene fluorescent beads (Duke Scientific 5 μm nile blue, density = 1.05 g/mL). After filling the devices, the inlet close to the piezo buzzer was plugged using thick tape (Scotch Magic tape). Depending on the experiment goal, the inlet connected to the downstream channel was plugged or left open to the air.

4.1.2 **Device operation**

Figure 4.1 shows a resonant microfluidic device mounted on a custom bracket attached to a micromanipulator (Sutter MP-285) and set on the epifluorescence microscope (Zeiss IM35 with Retiga 1300i cooled camera). A custom high-power (10W) blue LED strobe lamp was used as the light source for the microscope. The sinusoidal electrical actuation signal (V_{ac}) was generated using an NI DAQ (USB-6259). The signal was amplified using a custom amplifier (gain = 100, bandwidth = 60-4000Hz, negligible phase delay) and applied to the piezo buzzer on the microfluidic device. The AC pressure (P_{ac}) drives back-and-forth flow in the channels. This AC flowrate was calculated from imaging the trajectory (streak) of the suspended beads (Figure 4.1, imaging panel at the bottom). The bead trajectory (streak) was used to compute the volumetric flowrate magnitude. The bead location at different time points in the actuation cycle was compared to the actuation signal to evaluate the flowrate phase.

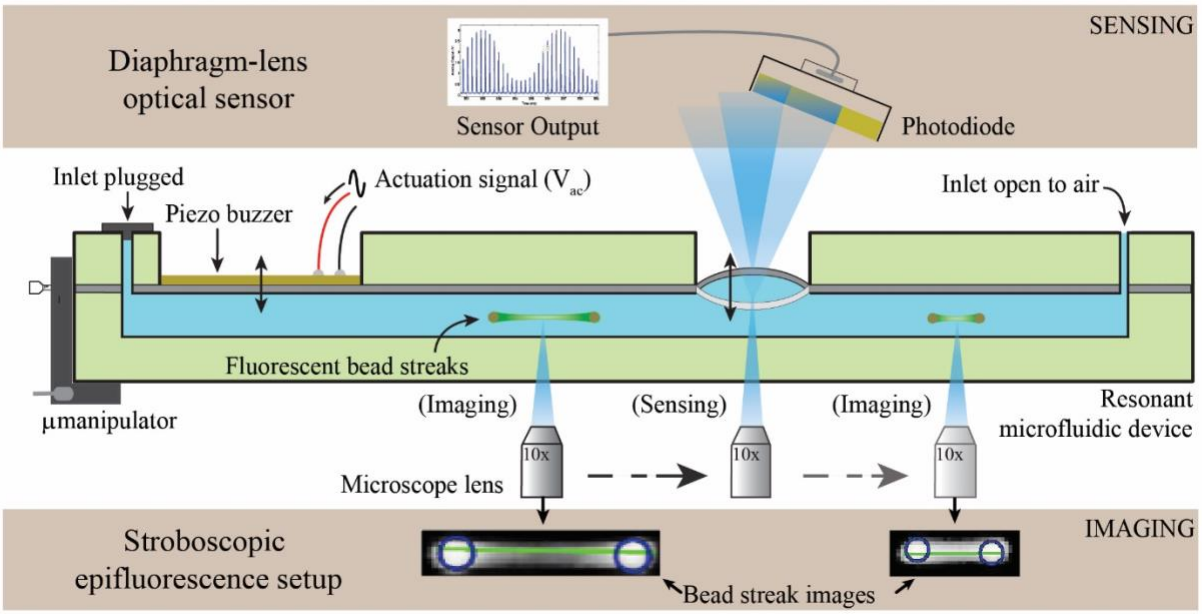

Figure 4.1. AC analysis experimentation setup

In the same setup, the vibrations of the deformable capacitor diaphragms were measured optically to estimate the AC flowrate in the capacitor (Figure 4.1, sensing panel at the top). Both techniques are described in more detail in the following sections. The micromanipulator, Retiga camera, LED light source and the DAQ were controlled and synchronized using a MATLAB (R2014b) program. The experimentation parameters, like the frequency range, imaging location in the channels, capacitor sensing location, strobe light parameters (frequency, intensity) and camera settings (exposure, gain) were inputs to the MATLAB program. The setup automatically captured bead streak images from the upstream channel (imaging), translated the device, so that capacitor vibration was measured by the photodiode (sensing), and then moved to capture the bead streaks in the downstream channel (imaging). The frequency of the actuation signal was changed, and the process was repeated for a range of actuation frequencies. Measurement errors due to setup, filling and mounting variations were avoided by performing the full set of measurements (flow magnitude and phase) in a single experimentation run.

The rich measurements presented in this work were made possible due to the automated nature of this experimentation setup which reduced measurement errors from setup, filling and mounting the device, as well as ensured perfect synchronization between equipment involved - a requisite for accurate phase measurements.

4.1.3 **Stroboscopic epifluorescence measurement**

Magnitude and phase of AC flow in the channel were measured using this technique.

4.1.3.1 Flow Magnitude

The magnitude of the AC flowrate in the channel was estimated by mapping the entire trajectory of suspended beads. This measurement required constant illumination (no strobe). The camera

exposure (400 ms) was long enough to illuminate the bead movement over multiple cycles. Images were acquired at the channel centerline and three different locations along the channel. Three images were acquired at each location, making a total of 9 images per frequency. MATLAB was used to programmatically: 1. segment the images for bright streaks-like objects in the black background, 2. locate the ends and body of the streak, and 3. measure the streak length as the distance between the ends (accounting for finite bead size). Figure 4.1 (imaging panel) shows the output of this program with superimposed ends (blue circles) and body (green line). The streak length was used to estimate AC flow velocity, which was then converted to the volumetric AC flowrate magnitude including full accounting for the non-linear flow profile, as described in Section 3.3.3. The process was repeated over the range of actuation frequencies.

4.1.3.2 Flow Phase

After the flow magnitude measurement, the device was translated to the capacitor sensing location and the illumination was set to a strobe pattern to fixate bead positions along the trajectory at different time points in the sinusoidal cycle. The strobe duration was set as 3% of actuation signal time-period (T). The strobe position (offset) relative to the zero crossing of the electrical actuation signal (V_{ac}) was varied from 0 to 3T/4 in steps of T/4. At each of the four offsets, the strobe was repeated for 80 cycles of the actuation signal to ensure bright image formation (total exposure >1s). It is important to note that for the low-frequency operation (<1 kHz), as here, the electrical actuation signal (V_{ac}) and the resulting pressure underneath the piezo buzzer (P_{ac}) are in-phase[34], [35].

Three images were acquired per phase offset for each frequency, in the following order: The first image was acquired in the absence of the actuation signal to capture the ‘rest’ position of the bead. The next image was acquired with the actuation signal turned ON with the strobe occurring

at the phase offset (0, T/4, T/2, or 3T/4). The last image captured the entire bead trajectory (the 'streak') by illuminating the channel with constant light over the same number of cycles (80) as the preceding measurement.

The three images acquired at each offset were combined to overlay the rest position and the offset position of the bead onto the bead trajectory (Figure 4.2 b-d). The position of the bead along its trajectory relative to the rest position was measured manually for each of the four offsets, and the relative bead position at the four offsets was fitted to a sum of sines function (Figure 8.1 in Supplementary Information Section 8.1). The fitted phase was considered a valid measurement if the fitted frequency was within ±10 Hz of the actuation frequency. The phase measurement was repeated for the entire frequency range to get the phase response (Figure 4.2 f and Figure 4.3 c). It should be noted that given the complexity of measurement and analysis, flow phase was acquired sparsely (50 Hz increments) compared to flow magnitude measurement (10 Hz).

The fitted phase using the procedure above was the phase difference of the bead position, x(t), compared to the actuation signal (electric V_{ac} or pressure P_{ac}, which were in-phase). Since position, x(t), and velocity, v(t), are related by a rate differential (v=dx/dt), there is a 90° phase shift when converting the fitted phase of bead positions to phase of the velocity/flowrate. When the bead is at the center of the trajectory, its position related to the 'rest' point is minimum (zero), but its velocity is maximum – much like a simple pendulum. At the extremes, the bead position is maximum, but the velocity becomes minimum as the bead comes to a stop at the end points of its trajectory. This was also evident in bead streak images with the ends appearing brighter than the rest of the streak. Figure 8.2 in Supplementary Information Section 8.2 illustrates this phase difference between bead position and bead velocity. To allow comparison to the electric circuit model, the bead position was converted to bead velocity by adding 90° to the fitted phase.

4.1.4 **Diaphragm-lens optical sensor measurement**

The flowrate into or out of the capacitor was measured by estimating the magnitude and phase of the deflection of the diaphragm that forms the capacitor. A novel diaphragm-lens optical sensor was developed for the task. Light from the microscope objective passed through the fluid and transparent diaphragm and was captured by the large active area photodiode (Hamamatsu S1226-8BKSi), as shown in Figure 4.1. As the diaphragm bends and flexes under the AC pressure, the lensing effect from the fluid and diaphragm causes the spot size (optical intensity) on the photodiode to change. This modulation in the intensity was amplified using a transimpedance amplifier (Melles-Griot 13AMP005), and the output voltage (V) was acquired using the DAQ at a high sampling rate of 44 kHz. The voltage (V) was converted to equivalent bead streaks (pixels) using a linear function obtained through calibration experiments (see Figure 8.3 Supplementary Information Section 8.3). The bead streaks were converted to AC flowrate magnitude using the method described above. The phase of the acquired signal was adjusted for the phase added by the transimpedance amplifier (180°). The measurement was repeated for the entire frequency range to get the magnitude and phase response (Figure 4.2 e-f and Figure 4.3 b-c). This measurement was performed more frequently (1-2 Hz increment) since it was quick and required minimal processing and analysis.

4.1.5 **Electrical circuit model**

Circuit models were constructed using the simplest interpretation of electrical circuit elements for the piezo driver, channels, and capacitors. Resistance (R_u, R_d) and inductance (L_u, L_d) were calculated from the exact impedance solution of the Navier-Stokes equations for harmonic flow. Capacitor values (C_p and C_c) and the AC pressure source (P_{ac}) were derived by fitting the electrical

circuit model to experimental data using the capacitance and the pressure source as fitted parameters. A separate set of calibration devices were used to perform these fitted measurements independently. The fitted result from the replicate devices (n=3) was averaged and used in the predictive model (Figure 4.2 b-c and Figure 4.3 e-f). A library of capacitances (varying sizes, thickness, and materials) and pressure sources was created using this method (Table 3.1).

The circuit was completed by treating any plugged inlet as an open circuit, while an inlet open to the atmospheric pressure (air) was represented as a connection to ground. Electrical network mesh analysis was used to solve for flow magnitude and flow phase compared to the pressure source (P_{ac}) as a function of the actuation frequency. Analytical expressions for resonance frequencies were derived by minimizing (or maximizing) the impedance functions for series (or parallel) resonant circuits; the expressions are provided in Supplementary Information Section 8.4. It is important to note that the model predicts flow phase compared to the pressure source (P_{ac}), and measurements of phase in this study were made with respect to the electrical actuation signal (V_{ac}), but since P_{ac} and V_{ac} were in-phase, the model prediction to the experimental phase measurements can be simply compared.

4.1.6 **Results**

Simple series and parallel resonant devices were designed and the flowrate magnitude and phase in the channel(s) and the capacitor were measured. The measurement obtained using the two independent techniques described in the Sections 4.1.3 and Section 4.1.4 closely track the electrical circuit model prediction, thereby confirming that the complex flow magnitude and phase interactions in microfluidic circuits are predicted using the classic electric-hydraulic analogy.

4.1.6.1 Series resonance device

The simplest resonant device consists of a piezo buzzer and a single channel connected to the capacitor. Such a device schematic and equivalent circuit model are shown in Figure 4.2 (a). After filling the device, both the inlets were plugged as depicted in the circuit model with 'X' marks. The model represents a classic electrical series resonant circuit where the resonance frequency is simply dependent on the total inductance (L_u) and the total capacitance ($C_t \sim C_c$ since $C_t = C_pC_c /(C_p + C_c)$ and $C_p >> C_c$), and is given by

$$f_s = {}^{1}\!\Big/\!_{2\pi\sqrt{L_u C_c}} \quad . \qquad (4.11)$$

Since the upstream channel and capacitor are series-connected, and the fluid has no other escape path, it was expected the flowrates in the upstream channel (Q_u) and capacitor (Q_c) to be identical in both the magnitude and phase. The flowrate magnitude frequency response should only have one peak – $\boldsymbol{f_s}$ – at the model-predicted resonance frequency. By definition, at this peak flowrate frequency, the pressure source and the flowrate should be in-phase. For frequencies below the resonance frequency (pre-resonance), it was expected that the flow lags the pressure source P_{ac} (capacitive regime), and above the resonance frequency (post-resonance), the inductance of the circuit dominates resulting in the flow leading the pressure source (P_{ac}).

Figure 4.2 b-d illustrates the process of estimating the phase of flowrate in the channel compared to the electrical actuation signal (V_{ac}), as described in the Section 4.1.3.2. The first of the two images on the left in Figure 4.2 (b) (phase at a pre-resonance frequency) depicts the bead before the actuation signal was applied (yellow, rest position). The bead was found close to this rest position after the actuation signal was turned on (magenta, denoted as t=0). The blue pixels represent the complete trajectory of the bead and were used to fixate the traversing bead at different offsets. In the next image on the right, the bead was located at the top extreme position (magenta)

and moving back towards the rest position (yellow). Bead positions at the two time points, 0 and T/4, and their anticipated direction of movement are illustrated in the bead streak to the right. The location of the bead with respect to the rest position was fitted to a sum of sines function and compared to the electrical actuation signal V_{ac} (far right, Figure 4.2 b). The phase difference between the fitted signal and the actuation signal was the phase of the bead position, in this case about 0°. After accounting for the position to flowrate conversion (see Section 4.1.3.2), the phase was adjusted by +90°, which is expected of a resonant circuit at low frequencies where the capacitance of the circuit dominates. While only images from t = 0 and t = T/4 are shown in Figure 4.2 (b-d) for simplicity, in the actual analysis, the data from the bead positions at all the four phase offsets (0, T/4, T/2, 3T/4) were used in the fit (Figure 8.1 in Supplementary Information Section 8.1).

Hence, at a low frequency, the bead location at t = 0 was same as the rest position. The bead moved away (up in Figure 4.2 b) and reached the top extreme by t = T/4. The fitted function on the right is sinusoidal and is in-phase with the electrical actuation signal (V_{ac}). In converting the bead position to flowrate, 90° was added and estimated the flowrate phase as +90°, which indicates capacitance of the circuit dominates the flow behavior.

At the resonance frequency, as shown in Figure 4.2 (c), the bead (magenta) was at the bottom of its trajectory at the start of the actuation cycle (t = 0) and made it to the rest position by the next imaging offset (t = T/4). The fitted sine wave on the right is a negative cosine function, which lags the sinusoidal actuation signal by (-)90°. After accounting for the position-to-flowrate conversion, it was determined that compared to the electrical actuation signal (V_{ac}) the flow was indeed in-phase (- (− 90° + 90° = 0°) at the resonance frequency.

At a high frequency beyond resonance (Figure 4.2 d), the bead started at the rest position at t = 0 but moved down and to the bottom extreme by t = T/4. This behavior appears reversed compared to the low frequency (Figure 4.2 b). Fitting revealed a negative sine wave, i.e., 180° phase difference compared to the actuation signal. After correction, the flowrate phase was estimated to be -−90° (180° + 90° = 270° = -−90°), confirming that the inductance of the circuit dominated post-resonance.

Figure 4.2 (e) shows that the flow magnitude in the upstream channel (Q_u) measured by observing the bead streaks in the channel and the capacitor (Q_c) estimated through the deflections of the diaphragm match remarkably well considering the two independent measurement methods. The flow magnitude peaks at a single frequency (600 Hz) and rapidly decreases away from the resonance frequency. Figure 4.2 (f) shows that the flowrate phase values measured independently in the upstream channel (Q_u) and the capacitor (Q_c) also match the model prediction for a series resonant circuit. At low frequencies, the impedance was dominated by the capacitance (scales as $1/f$), and therefore the flow leads (positive) the actuation signal by 90° (as seen with classic capacitor behavior). As frequency was increased, the inductive impedance (scales as f) increased and canceled the capacitive impedance at the series resonance, which is the frequency of least impedance, and therefore peak flow. Since the reactive part of the impedance was canceled at this frequency, the purely resistive impedance resulted in flow being in-phase with the electrical actuation signal (V_{ac}). Finally, as frequency was increased, the inductive impedance dominated, which led to a reduction in flow magnitude and flow lagging (negative phase) compared to the electrical actuation signal (V_{ac}). As noted above, the flow phase remains the same when compared to the pressure source (P_{ac}), since V_{ac} and P_{ac} were in-phase. The key take away is that the simple

series microfluidic resonant circuit behaves exactly like its electrical counterpart, and both flow magnitude and phase exhibit behavior typical of resonant electrical circuits.

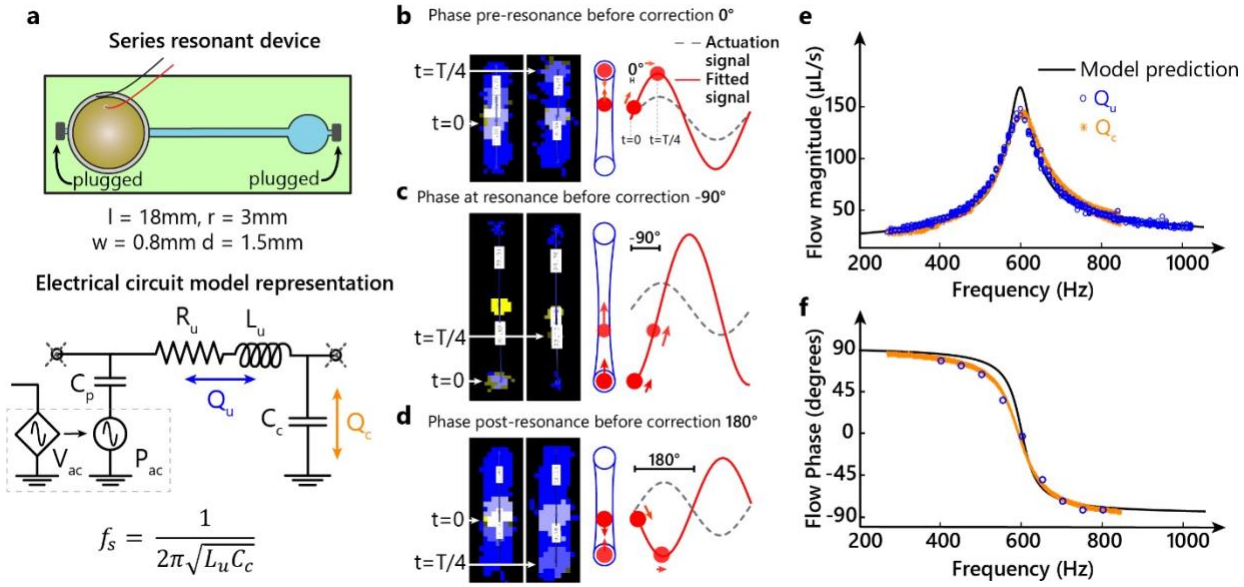

Figure 4.2. AC analysis of a series resonant device

Figure 4.2 **Extended Caption a**. Schematic and electrical circuit equivalent of the series resonant device. This is the simplest resonant device and features a piezo buzzer connected in series to a single channel and a capacitor. Device dimensions show the length (l), width (w) and depth (d) of the channel and the radius of the capacitor (r). Both the inlets were plugged after filling the device, which is depicted as an open circuit in the electrical circuit model. P_{ac} = 0.2 kPa was used for all model calculations. Since the piezo capacitance C_p (= 132 x 10^{-3} mm^3/kPa) and the capacitor C_c (= 4.02 x 10^{-3} mm^3/kPa) are series connected, the circuit could be represented by an equivalent capacitance, which in this case was just C_c as $C_p >> C_c$. The model accounts for the frequency dependence of the inductance and resistance. To get a rough estimate of the resonance frequency, the inductance was averaged over the frequency range (0-1000 Hz) to get L_u = 17.2 µkg/mm^4. Using the classic formula shown, the resonance frequency $\mathbf{f_s}$ was estimated as 607 Hz. **b.-d.** Illustrate the process of estimating phase through tracking beads suspended in the channel. **b.** Shows the phase shift calculation for the series resonant device at a pre-resonance frequency (400 Hz). Bead position (magenta) with respect to the rest position (yellow) were fitted to a sum of sines function. The fitted phase, in this case about 0°, was adjusted for position-to-flowrate conversion (+ 90°) to obtain the corrected phase of the flowrate. **c.** Shows phase

calculation at resonance which yielded the expected phase difference of 0° after correction. **d.** Phase calculation shows the flow lagging the actuation signal by about 90° at a post-resonance frequency (800 Hz). **e.** Flowrate magnitude obtained from the channel and the capacitor both show a peak at 600 Hz, which is comparable to the analytical calculation for resonance performed earlier. The full model response also shows remarkable adherence to the prediction **f.** Flowrate phase response show in-phase flow at resonance and capacitive (leading) and inductive (lagging) behavior pre- and post-resonance respectively, as expected from the classic electrical circuit theory. Representative data from a single device is shown here. Two replicates of the device exhibited similar magnitude and phase behavior at a resonance frequency of 610 Hz and 600 Hz respectively.

4.1.6.2 Parallel resonance device

While series resonant circuits are more common, another class of resonant devices employs the parallel connection between the inductance and capacitance to realize frequency dependent circuit behavior. In this work, the downstream channel formed a parallel connection to the capacitor, and this topology was utilized to create the valley in the upstream flowrate frequency response. The upstream channel length was made much smaller compared to the downstream channel, which reduced the total impedance, and the resulting increase in the resonance frequencies was compensated by enlarging the capacitor. The device schematic and equivalent circuit model are shown in Figure 4.3 (a). After the device had been filled, the inlet next to the piezo buzzer was plugged, and the inlet connected to the downstream was left open to the air, as depicted in the device schematic and the circuit model.

Figure 4.3 (b-c) shows the model-predicted and experimentally-measured frequency response of flow magnitude and phase. The flow magnitude response shows a sharp dip in the upstream flowrate (Q_u), which was especially apparent because f_p (250 Hz) was designed to be close to the peak flow frequency f_s (310 Hz). At f_p, the flow (Q_u) in the directly-driven upstream channel was substantially reduced compared to the downstream channel (Q_d), which was further away from the

pressure source. This interesting phenomenon was even more apparent in the flow images shown in Figure 4.3 (d-e). Shorter bead streaks in the upstream channel indicate considerably smaller flow compared to the downstream channel (Figure 4.3 e) at f_p = 250 Hz. While the flow upstream was reduced, the frequency response shows a large magnitude flowrate that shuffled between the downstream channel and the capacitor. This equal and opposite (180°) in-phase flow between the downstream channel (Q_d) and the capacitor (Q_c) at f_p is evident in the flowrate magnitude and phase plots (Figure 4.3 b-c).

At the model-predicted f_o (80 Hz), the flowrates in the upstream channel (Q_u) and the downstream channel (Q_d) were comparable in magnitude and were in-phase. As a result, no measurable flow was observed through the capacitor (Q_c) around f_o. At the series resonance frequency f_s, all the three flowrates were significant, and the channel flowrates roughly added up to equal the capacitor flowrate. This flow addition was possible due to opposing directions of the flow in the upstream and downstream channels (as depicted in Figure 3.4) and was also observed in the phase response in Figure 4.3 (c). Hence, the flow magnitude and flow phase measurements validate the complex flow interactions predicted by the simple electrical circuit model predicted at the different resonance frequencies.

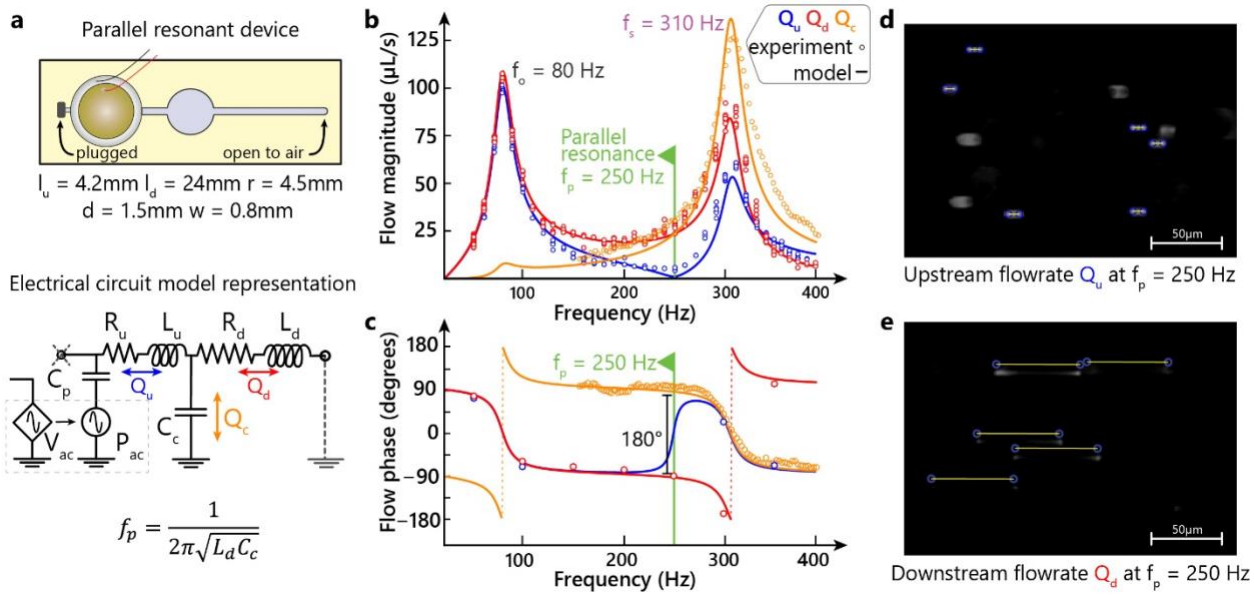

Figure 4.3. AC analysis of a parallel resonant device

Figure 4.3 **Extended Caption a**. Schematic and electrical circuit equivalent of the parallel resonant device. The upstream channel (Q_u) was designed to be much shorter than the downstream (Q_d) channel to emphasize the parallel resonance valley in the upstream flowrate. For a rough estimate of the parallel resonance frequency: the average downstream inductance L_d = 22.2 μkg/mm^4 and C_c = 20.1 x 10^{-3} mm^3/kPa resulted in f_p = 239 Hz using the classic formula shown. **b**. Flow magnitude depicts familiar peaks and valleys in the frequency response. The device was engineered to have a sharp dip at the parallel resonance, and the model and experimental data indicate that the goal was achieved. The flow magnitudes in the downstream channel (Q_d) and the capacitor (Q_c) matched at the parallel resonance (250 Hz), which coincides with the minimum in the upstream flowrate (Q_u). **c**. At f_p, the flow phase difference between the downstream channel (Q_d) and the capacitor (Q_c) was 180°, indicating that the flows are equal in magnitude but opposite in phase. Data points for upstream flow phase were missing where the flow magnitude was too small to resolve bead positions in the traverse. **d-e**. Flow images at f_p from the upstream channel showed shorter bead streaks indicating upstream flowrate was reduced, while at the same frequency in the channel further downstream featured considerable flow (longer bead streaks) The parallel resonance was predicted by the model and the experimental results validated the interesting phenomenon. Two replicates of the parallel resonance device exhibited comparable magnitude and phase behavior at the parallel resonance frequency of 230 Hz and 220 Hz, respectively.

4.1.7 **Discussion**

Of the two measurements performed in this work, flow phase can result in more accurate determination of resonance frequency than flow magnitude. Rather than sweeping for the unknown peak in flow magnitude, the frequency point where the phase of flow crosses zero can be an accurate indicator of resonance. This is based on a fundamental metrology principle that measurement accuracy is optimized when the quantity being measured (in this case, phase) crosses a fixed reference level (in this case, a zero crossing) at maximum slope. This is the same basic concept frequency and time period measurement in common multimeters. In addition, the slope of flow magnitude becomes minimum as resonance is approached, increasing the error of locating its maxima. Increments in frequency result in progressively smaller changes in flow magnitude. This may make the process of measuring the peak in flow magnitude subtle and more error-prone. On the contrary, the slope of flow phase is maximum at the point where it needs to be measured, making it the more accurate and preferred of the two measurements presented here.

Following up the note on accuracy, it is important to consider the time it takes to perform the measurement. Sweeping through the frequency range to map out the magnitude and phase response is essential to understand and compare against the electrical circuit model. However, given the power and computation requirements, this technique may be inefficient for low-resource settings, where lab-on-a-chip and microTAS devices have the potential to make the most impact. Therefore, measurement techniques inspired from electrical engineering like Fourier and Step Analysis should be investigated for rapid measurement of the frequency response of microfluidic resonant circuits.

4.1.8 **Conclusions**

The work presented in this chapter advances the field of frequency-tuned flow control by demonstrating the tools and techniques needed for simultaneous flow magnitude and phase measurement. Missing until now, the ability to quantitatively measure both magnitude and phase confirms that the core behaviors of RLC circuits hold well for these simple microfluidic circuits. This suggests that models can be used to design circuits with new functions including frequency-dependent fluidic control in microfluidic networks, or even circuits that change behavior depending on properties of the channel or fluid. In addition, circuits might be designed to allow analyte-mediated changes in fluidic properties (density, viscosity) to be detected as a shift in the resonance frequency. Regardless of the application, this work further verifies the electric-hydraulic by showing that complex magnitude and phase responses match predictions, and it provides tools that can be used to design advanced microfluidic circuits in the future.

4.2 FOURIER ANALYSIS

AC analysis is one classic method for system characterization, and the literature in electrical engineering is rich with a myriad characterization of special purpose techniques, each with a special use-case optimized for specific applications. The primary difference between these techniques is usually the input or the actuation signal. For example, in Fourier Analysis, the input is a composite of multiple frequencies. The frequency components expressed in the resulting complex output informs characterizes the circuit's response to the individual frequency components in a single measurement. Hence, Fourier Analysis is used to specifically probe the circuit response at frequency points of interest, rather than the entire bandwidth. In microfluidics, the Fourier approach is particularly attractive for characterizing multi-channel pump networks

where the design goal is for each channel to resonate at a specific frequency and have muted response at resonance frequencies of other channels. In a single flow measurement per channel, Fourier analysis can provide flow response at every pumping frequency, which would otherwise require multiple measurements using AC analysis. This work demonstrates the Fourier Analysis technique to characterize the frequency response characterize and estimate the cross-talk in a multi-channel microfluidic network and compare results to conventional AC analysis.

4.2.1 **Device fabrication and filling**

The microfluidic design is based on electrical circuit models, and the laminated fabrication of microfluidic resonant devices is described in preceding sections. A schematic of the multi-channel network used for Fourier analyses is shown in Figure 4.4. The channels (1, 2, and 3) were laser-cut out of acrylic sheets of different thicknesses (2 mm, 1.5 mm, and 1 mm, respectively). The three channels overlapped and connected at the large Rohaglas diaphragm to which a piezo buzzer was affixed to form the shared actuation source. The layers were pressure bonded with PDMS tape. The channel lengths, depths, and capacitor sizes used in the device pictured in Figure 4.4 (b) were as follows: Channel 1 – length 15 mm, depth 2 mm, capacitor radius 4.5 mm; Channel 2 – length 7 mm, depth 1.5 mm, capacitor radius – 3.5 mm; Channel 3 – length 7 mm, depth 1 mm, capacitor radius 3 mm. All the channels were 0.8 mm wide. Channels 1 and 2 had two-sided capacitors formed by flexible Rohaglas covering top and bottom of the channel. Channel 3 had a one-sided capacitor with flexible Rohaglas on top and a stiff acrylic cover on the bottom side, which effectively halved the capacitance. These channel and capacitor dimensions were chosen such that the resonance frequencies of Channel 1, 2, and 3 were 200, 600, and 1000 Hz, respectively, and the impedances of the channels at the respective resonances were matched.

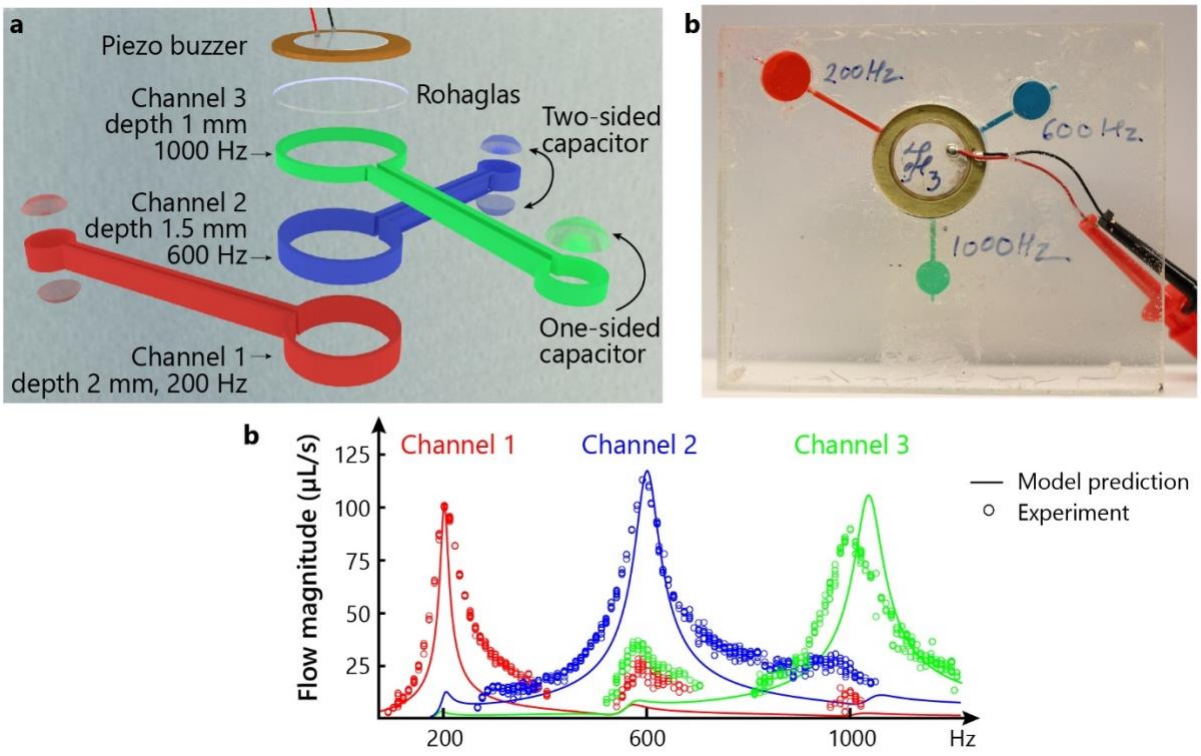

Figure 4.4. Schematic and characterization of multi-channel microfluidic device

Figure 4.4 **Extended Caption a.** Schematic of the device used for Fourier and Step Analysis. The channels were formed from laser cut sections in acrylic sheets. The piezo buzzer was affixed to the Rohaglas diaphragm of the same size and shared by the channels. Only the diaphragms were allowed to deform through cutouts in the layer above and/or below. The channel floor and ceiling were capped by stiff acrylic to reduce the parasitic capacitance. Inlets (not shown) for filling were added downstream of the capacitors in the channel, but they were plugged during operation. The viscous drop in pressure along the cylindrical piezo cavity (20 mm x 4.5 mm) was insignificant compared to the channels (1-2 mm deep x 0.8 mm wide), therefore it was expected that the same pressure was driving the channels. The schematic is not to scale. **b.** Photo of the device used for Fourier and Step Analysis. **c.** Frequency response of the flow magnitude (AC analysis) confirmed that each channel resonated at the designed frequency and the impedances were matched at the respective resonances, as shown by the comparable flow magnitudes. In addition, the model was known to undervalue inductance at high frequencies. Hence, Channel 3 was designed to overcompensate such that the experimental resonance frequency falls short of model prediction at 1000 Hz.

Figure 4.4 (c) shows the frequency response of the flow magnitude (AC Analysis) estimated by measuring the bead streak lengths in the three channels. Inlets (not shown in the schematic in Figure 4.4) were added downstream of the capacitor in the three channels. Glycerol solution (dynamic viscosity = 1.024 mPa·s, density = 1.05 g/mL) with suspended polystyrene fluorescent beads (Duke Scientific, 5 μm nile blue, density = 1.05 g/mL) was used to fill the device. The device was filled by simultaneously injecting the glycerol solution using pipettes through any two inlets until the fluid started flowing out of the third inlet. All the inlets were plugged using thick tape (Scotch Magic Tape) after filling. Fourier and Step analysis experiments were performed three times with the device emptied and re-filled with every run to account for filling errors. The averages of these measurements were used in the analyses.

4.2.2 **Device operation**

The preceding Section 4.1.3 details an automated stroboscopic epifluorescence experimentation setup for measuring AC flow magnitude and phase in a microfluidic channel. This same experimentation setup and methods were utilized for Fourier characterization of the multi-channel microfluidic network with two key differences: 1) Actuation signal: Instead of single-frequency actuation, the input signal was synthesized by adding weighted sinusoidal waveforms using MATLAB (Release 2017b, The MathWorks, Inc., Natick, Massachusetts, United States). The composite signal was generated on an NI DAQ (USB-6259) and was amplified using a custom amplifier (gain = 100, bandwidth = 60-4000 Hz, negligible phase delay). The amplified signal was applied to the piezo buzzer on the microfluidic device. 2) Phase offsets: In the preceding work (AC analysis), the flow phase was estimated by tracking the bead position in the back-and-forth traverse. A microscope strobe light was set to illuminate the bead position at four offsets t = 0, T/4, T/2 and 3T/4 (T is the inverse of the actuation frequency, f). This sampling duration (1/4f) was

smaller than the Nyquist duration (1/2*f*) required for the complete reconstruction of the harmonic bead traverse. In the Fourier analysis, the AC flow was expected to be made of multiple frequency components with the maximum being 1000 Hz. Therefore, in accordance with the prior work, the sampling rate was set to 1/4000 Hz^{-1} (1/4*f*) or a sampling duration of 0.25 ms. The bead positions at these phase offsets were fitted to a sum of sines function. The fitted magnitudes at the three frequencies were converted to volumetric AC flowrate including correction for channel cross-section area and non-linear flow profile as described in Section 4.1.3.

4.2.3 **Results and discussion**

The primary design goal for the multi-channel microfluidic device was a demonstration of the classic electrical characterization techniques of Fourier and Step Analyses (see Section 4.3). Fourier and Step Analyses were expected to translate well to fluidics because microfluidic resonant circuits, like their electrical counterparts, are linear time-invariant systems. Linear systems, along with other properties, obey the superposition principle, which dictates that the net system response to multiple inputs is the sum of responses that would be caused by the individual inputs. The research goal was to demonstrate superposition principle on the same multi-channel microfluidic device using the classic Fourier series examples of square and triangle waves. The latter design goal dictated that the resonance frequencies of three channels be related by odd harmonics (n = 3, 5). 200 Hz for Channel 1 was selected as the fundamental frequency; Channels 2 and 3 were designed for resonance at 600 Hz and 1000 Hz, respectively, to correspond to odd harmonics. In addition, the impedance (resistance) of the three channels was matched at the respective resonances to give matched AC flow magnitudes for each channel when driven at its respective resonance frequency or allowed to oscillate at its natural frequency. Since the microfluidic resistance increases with the actuation frequency, unlike the electrical counterparts, resistance

matching was performed by the numerical electrical circuit model described in Section 4.1.5. The AC analysis, shown in Figure 4.4, confirms that the design goals (resonance frequencies and matched impedances) were met. It is important to note that the characterization technique described through this demonstration can be generally applied to any microfluidic device; the choice of harmonically-related resonance frequencies and matched impedances were set to allow clear observation of results that further validate the electric-hydraulic analogy.

The Fourier analysis involved exciting the microfluidic device with complex harmonic actuation signals composed of weighted sinusoidal signals of frequencies corresponding to the resonance of individual channels. In the simplest case, the actuation signal was synthesized by adding 200 Hz, 600 Hz, and 1000 Hz sine waves with equal weights (1:1 composite in Figure 4.5 a). The goal of this experiment was to ascertain the cross-pumping between channels by deconstructing the harmonic flow for individual frequency components.

When excited by a complex harmonic signal containing individual resonance frequencies, it was expected that the AC flow in each channel would be dominated by the respective resonance frequency. The harmonic flow in response to the complex 1:1 composite actuation signal was recorded in the three channels by tracking suspended beads in their back-and-forth transverse. Figure 4.5 (b) shows the bead positions from the three channels fitted to a sum of sines function (lines). The fitted functions are plotted on the same time scale, which shows that the flow in Channel 1 was primarily composed of 200 Hz frequency (upper, red), Channel 2 was dominated by 600 Hz (middle, blue), and Channel 3 was dominated by 1000 Hz (lower, green), along with other harmonic components masked in the non-sinusoidal shape of the fitted curve. Thus, not surprisingly, each channel selected for its resonance frequency component from the actuation signal medley.

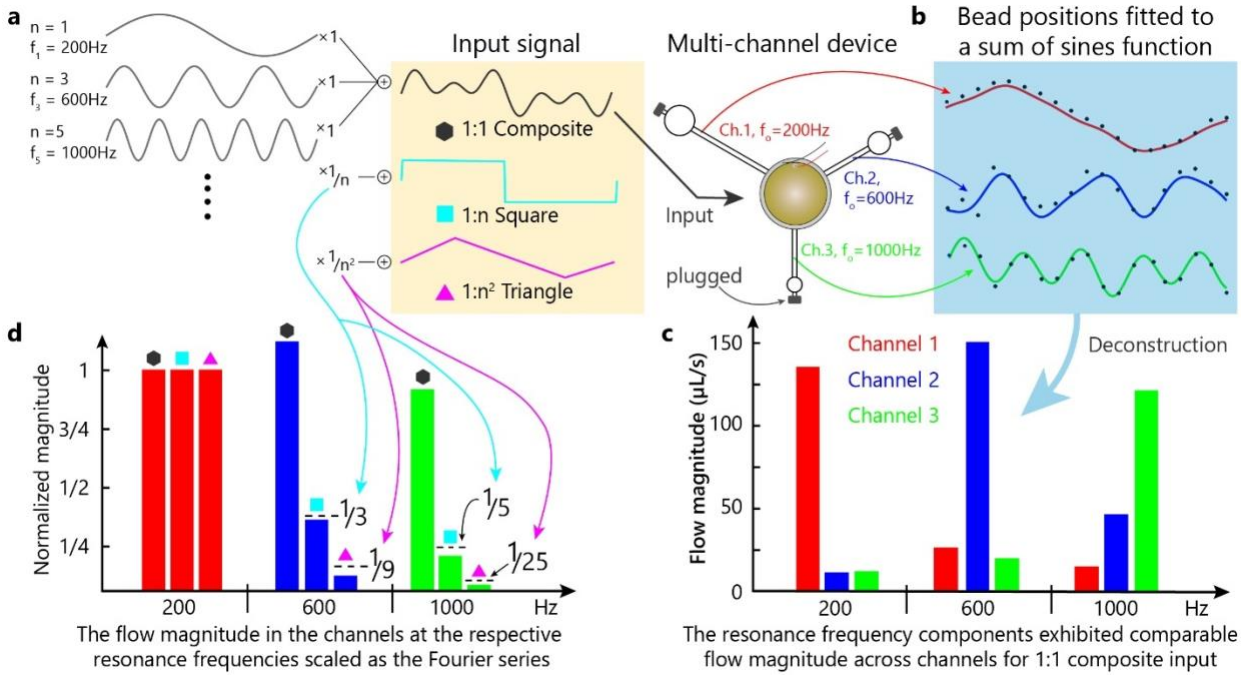

Figure 4.5. Fourier analysis of the multi-channel microfluidic resonant device

Figure 4.5 **Extended Caption a.** The input actuation signal was synthesized by adding weighted sinusoidal waves at the fundamental frequency (200 Hz, n=1) and its odd harmonics (n=3, 5,…). The composite signal was created by adding all the constituent frequencies equally. The harmonics were scaled as 1/n and $1/n^2$ for synthesizing the square and triangle signals, respectively. The input signal was applied to the piezo buzzer on the Fourier device filled with the fluorescent bead-laden glycerol solution and the inlets plugged. **b.** The channel flow responses to the stimuli were recorded as bead positions in the back-and-forth traverse. The bead positions fitted to a sum of sines function showed that the flow in Channel 1 (red) was predominately lower frequency than in Channel 2 (blue) and Channel 3 (green, highest). **c.** The frequency breakdown of the fitted output showed that the flow in the Channels was 1. dominated at the respective resonance frequencies (Ch1: 200 Hz, Ch2: 600 Hz and Ch3: 1000 Hz) and 2. comparable in magnitude. The cross-pumping between channels was represented by the smaller bars. Pumping at 1000 Hz (i.e. activating Channel 3) would result in most cross-pumping whereas Channel 1 activation was mostly immune to cross-pumping. **d.** Channel response at respective resonance frequencies to composite, square, and triangle actuation signals scaled as a Fourier series. The flow in Channel 1 was sustained while Channel 2 and Channel 3 flow magnitudes scaled closed to 1/3, 1/9 and 1/5, 1/25 to square and triangle wave actuations, respectively.

Since all channels have a comparable impedance at their respective resonance frequencies, the AC flowrate magnitude at resonance should reflect the magnitude of that frequency component in the input signal. Figure 4.5 (c) shows the frequency make-up of the harmonic flow in the three channels for the 1:1 composite input signal. Channel 1 (red bars) featured flow predominantly at 200 Hz, and the 600 Hz and 1000 Hz flow contributions were much lower. Similarly, the flow in Channel 2 (blue bars) and Channel 3 (green bars) was dominated by flow at their respective resonance frequencies (600 Hz and 1000 Hz, respectively). In addition, as expected the flow in the three channels at the resonance frequencies – Channel 1 at 200 Hz, Channel 2 at 600 Hz and Channel 3 at 1000 Hz – was comparable across the three channels. Thus, this measurement re-confirms the observations of the resonance frequency and matched impedances made in Figure 4.5 (c).

It was sought to estimate the flow in a channel at the off-resonance frequencies of the actuation signal (i.e. 600 Hz and 1000 Hz flow components in Channel 1). The non-dominant bars in Figure 4.5 (c) represent the magnitude of cross-pumping between channels as measured using the Fourier Analysis. For example, if Channel 3 was selected to pump (provided valves were added to create pumps) by setting the actuation frequency to 1000 Hz, substantial cross-pumping in neighboring Channel 2 and some in Channel 1 (see blue and red bars, respectively, for the 1000 Hz case) was anticipated. In comparison, Channel 1 pumping at 200 Hz and Channel 2 pumping at 600 Hz would be somewhat resilient to cross-pumping.

Quantitative pumping metrics, defined as the ratio of flow in a channel to total flow in the three channels at a fixed frequency, are listed in Table 4.2 alongside estimates from conventional AC analysis (in Figure 4.5 c) for comparison. Compared to AC analysis, which involves sequential actuation at each frequency of interest, the Fourier technique of estimating cross-pumping through

simultaneous actuation at the pumping frequencies can achieve similar accuracy (Table 4.2) with fewer measurements. In general, a multi-channel device with *m* channels and the same number of pumping frequencies would require a minimum of m^2 measurements to assess flow in the channels at all the frequencies. Using Fourier analysis, the same investigation would require one measurement per channel with a total of *m* measurements. For example, the device under consideration needed flow measurements at 200 Hz, 600 Hz, and 1000 Hz in Channel 1, 2, and 3 – a total of nine measurements listed in Table 4.1. With Fourier analysis, the table was populated from one measurement per channel. Hence, Fourier analysis offers an efficient alternative to AC analysis for characterizing multi-channel microfluidic resonant circuits.

Table 4.3. Comparing cross-pumping estimated through AC analysis and Fourier analysis

	200 Hz		**600 Hz**		**1000 Hz**	
	AC	**Fourier**	**AC**	**Fourier**	**AC**	**Fourier**
Channel 1	**1**	**0.85**	0.13	0.13	0.10	0.08
Channel 2	NA	0.07	**0.68**	**0.76**	0.20	0.26
Channel 3	NA	0.08	0.19	0.10	**0.70**	**0.66**
Total	1.00	1.00	1.00	1.00	1.00	1.00

Table 4.3 **Extended Caption** Comparing cross-pumping estimated through AC analysis (grey cells) and Fourier analysis (blue cells). The numerical value is the ratio of flow in a channel to the net flow in all the channels at a fixed actuation frequency. The bold cells indicate desired pumping – closer to unity is better. The rest of the cells represent cross-pumping and smaller values are ideal. Channel 2 and 3 are missing cross-pumping estimates at 200 Hz from AC analysis because the measurable flow was not observed as shown in Figure 4.4.

It is not surprising at all that when the individual inputs weighted equally to create the 1:1 composite actuation signal, comparable flow was observed in the three channels. So, to further corroborate the linearity of microfluidic resonant circuits, the input frequency components were scaled as 1/n and $1/n^2$, where n is the harmonic number, to synthesize the square and triangle signals, respectively, for use as actuation signals. Figure 4.5 (d) summarizes the channel responses at the three designed resonance frequencies. The response to the 1:1 composite signal from Figure 4.5 (c) is re-featured here (grey hexagon markers) for easy comparison. The flow magnitude values were normalized to the flow in Channel 1 at 200 Hz (n = 1, fundamental frequency) for the respective input. Similar to Figure 4.5 (c), the flow in the three channels at their resonance frequencies was comparable when all the constituent frequencies were weighted equally (1:1 composite input). When the weights were scaled as 1/n and added (i.e. $\propto .\ 200\,Hz + {}^{1}/_{3}.600\,Hz + {}^{1}/_{5}.1000\,Hz$), to create the square wave input, the channel responses adjusted proportionally as shown by the cyan-colored square markers. The response in Channel 1 at 200 Hz remained dominant, yet the flow magnitude in Channel 2 at 600 Hz and Channel 3 at 1000 Hz were measured just below the 1/3 and 1/5 marks. Similarly, the response to a triangle input (magenta triangle markers), where the frequency constituents were scaled as $1/n^2$ and added (i.e., $200\,Hz + {}^{1}/_{9}.600\,Hz + {}^{1}/_{25}.1000\,Hz$), showed scaling in flow magnitude near 1/9 and 1/25 for Channel 2 and 3, respectively, with Channel 1 at 200 Hz as the dominant flow. While these responses are expected from classic electrical circuit theory, the results demonstrate that the analogy of linear circuit elements holds for multi-channel microfluidic circuits.

4.2.4 **Conclusion**

In electrical engineering, Fourier Analysis is used to specifically probe the circuit response at frequency points of interest, rather than the entire bandwidth as in AC analysis. In microfluidics, the Fourier approach is particularly attractive for characterizing multi-channel pump networks. These pump networks by providing flow response at every pumping frequency in a single flow measurement per channel. This section describes the Fourier Analysis technique to frequency characterize a multi-channel microfluidic resonant device and compared results to conventional AC analysis.

4.3 STEP ANALYSIS

Step analysis is another classic electrical engineering characterization technique that also has a specific application in microfluidic circuits. In this technique, the transient response to a step change in input is used to characterize the circuit properties. In an RLC circuit, the transient response is an exponentially decaying sinusoidal signal, the frequency of which matches the resonance frequency of the circuit, and the decay factor represents the inertial and resistive losses (only for quality factors greater than unity). Step analysis provides rapid measurement of the resonance frequency and can be applied as a sensing technique in applications where resonance is linked to analyte-mediated changes in fluidic properties. The following section details the Step Analysis technique to frequency characterize the same multi-channel microfluidic network from the Fourier Analysis and compared the results to conventional AC analysis.

4.3.1 **Device operation**

In step analysis, the flowrate response in the channels to a step change in pressure applied by the piezo buzzer was measured. The step change in pressure was realized by gradually building up the

charge with a 120V DC input to the piezo buzzer and then providing a quick discharge path (1 Ohm, 5 W resistor, RC time constant 60 ns). The custom actuation circuit consisted of a DC power supply and FETs controlled by the NI DAQ (USB-6259). The actuation was repeated at 0.1 Hz to acquire multiple measurements. The resulting transient flow in the channels was measured optically at the capacitor using the diaphragm-lens optical sensor described in the previous sections. The sensor signal envelope was computed and fitted to an exponential function to estimate the decay rate of the sinusoidal signal. The frequency distribution of the sensor signal was calculated using a discrete Fourier transform. The frequency corresponding to the peak magnitude in the Fourier transform was denoted as the resonance frequency of the channel. All mathematical operations were performed using MATLAB.

4.3.2 **Results and discussion**

In the step analysis technique, the transient system response to a step change in input is used for characterization. For a second-order, under-damped, resonant system, like is the case here, the transient response to a step change is expected to resemble a decaying sinusoidal function. The frequency of the transient response is indicative of the resonance frequency and the exponential rate of decay ($e^{-R/2L}$) is a measurement of the viscous (R) and inertial (L) forces. Hence, Step Analysis is comparable to AC analysis in its information content (resonance frequency and quality factor = $\omega_r L/R$), but without requiring the input frequency to be swept.

In electrical engineering, the step response of series and parallel RLC circuits is a classic fundamental exercise method in circuit characterization. In this implementation, the voltage applied to the piezo buzzer was gradually increased to build a pressure (P_o) across the diaphragm capacitor (C_o). Then, the piezo buzzer was rapidly discharged (short-circuit) allowing the charged diaphragm capacitor to dump the stored energy into the inductor (L_o), and vice-versa, until the

energy was lost to the viscous drop represented by the resistance (R_o). This circuit model is shown in Figure 4.6 (a) along with the equation for the transient flow (Q_o) in the capacitor showing the exponential decaying sinusoidal response[48].

Figure 4.6 (b) shows the step characterization of the multi-channel network device used for the Fourier analysis. The flow response to the step actuation was optically recorded as the deflection of the diaphragm capacitor. The optical responses from the capacitors, shown after amplification and filtering in Figure 4.6 (a), depict decaying sinusoidal signals. The timescales, shown in Figure 4.6 (b), indicated that the frequency of the decaying sinusoidal signal matches the resonance frequency of the respective channel. The FFT analysis, shown in Figure 4.6 (c), confirmed that the dominant frequency in the optical response was the resonance frequency of the channel. The exponential fit to the extracted envelopes of the decaying sinusoidal signals in Figure 4.6 (b) are tabulated in Figure 4.6 (d). The decay factors from step response represent the ratio of resistance and inductance and are comparable to the model estimates computed at the resonance frequency of the channel. The discrepancy may be attributed to the fact that the transient flow equation, depicted in Figure 4.6 (a), does not consider the frequency dependence of R and L present in the fluidic domain. Therefore, even without the correction for frequency dependence, the rich information provided by step analysis can be used for frequency characterization of microfluidic

resonant circuits.

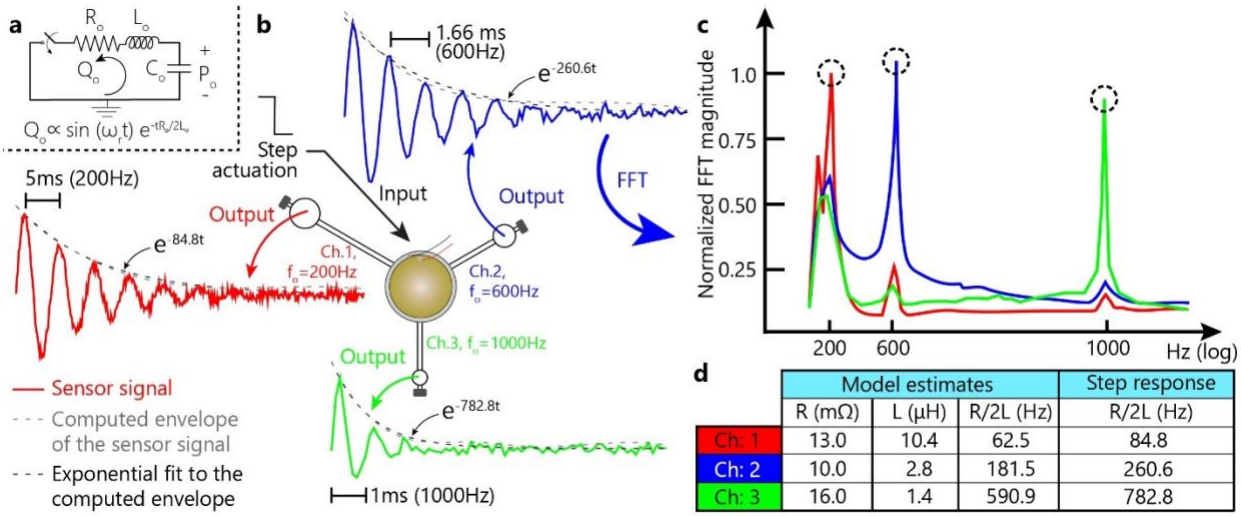

Figure 4.6. Step analysis of the multi-channel microfluidic resonant device

Figure 4.6 **Extended Caption a.** Circuit model for the derivation of transient flow in response to capacitor discharging in a series RLC circuit **b.** A step change in pressure was generated by rapidly discharging the bent piezo buzzer. The transient flow response to the step input in a channel was measured optical through the connected diaphragm capacitor. The sensor signal was a characteristic decaying sinusoidal with the time-period characteristic of the resonance frequency of the channel. The decay constant was computed by fitting an exponential function to the extracted envelope. **c.** The peak frequency in the FFT magnitude (circled) of the sensor signal matched the expected resonance frequencies of the channels. The first peak in the FFT response was the 120 Hz noise from ambient lighting. **d.** Exponential decay factor calculated using the RLC circuit model compared to the decay factor from step analysis showed a reasonable association.

Step analysis may find application when the resonance frequency or the decay factor needs to be measured rapidly and routinely. An example is a microfluidic lab-on-a-chip device where the presence of an analyte is tied to a fluidic property and manifests as a shift in resonance frequency or change in transient decay or both. The concept of linking the resonance frequency and/or damping to an analyte through the fluidic properties opens an alternate class of assay transduction

chemistries, like catalase-based bubble generation, polymerization, coagulation, and agglutination, for application in LOC devices.

4.4 CONCLUDING REMARKS

The analyses presented in this chapter are intended to illustrate that classic electrical circuit behaviors apply to their fluidic counterparts. As in electrical circuits, they offer different tradeoffs in information content and measurement overhead. Since the instrumentation can be re-purposed between characterization techniques, the choice simply depends on the experiment goal. If the aim dictates granularity in the data, which is often expected in the initial characterization phase with a new platform, AC analysis is more suitable. AC analysis provides rich data in form of flow magnitude and phase for the frequency range of interest but requires more computational resources using the method performed here. Fourier analysis is well-suited for the next design phase when the understanding and trust in the platform allows for probing only at the points of interest, like in the multi-channel network example here. Further, Step analysis could be a simple way to rapidly measure resonance frequency for quality control application or to monitor resonance frequency changes as a sensor on a LOC device. Beyond the extended characterization toolkit, the authors are confident that this work will inspire novel research directions utilizing the classic analogy to created improved frequency-tuned pumps and detection technique for application in LOC devices.

Chapter 5. FREQUENCY-TUNED MICROFLUIDIC PUMPS

Lab-on-a-chip and microTAS applications require methods to control fluids without relying on conventional bench-scale pumps. Piezoelectric micropumps were among the first integrated flow control methods for lab-on-a-chip devices[49]. Classic micropumps are micromachined silicon channels with two or more passive valves and a piezo-driven diaphragm as a harmonic pressure source. The pressure creates back-and-forth (AC) fluid motion, the valves provide partial AC-to-DC flow rectification, and the pumping direction is determined by asymmetric valve geometry. Pumping is maximum at the mechanical resonance frequency of the piezo-diaphragm (tens of kHz); it drops drastically when driven off-resonance and the microfluidic channels and valves minimally affect this frequency response.

In contrast, the groups of Landers and Begley demonstrated a different class of microfluidic pumps in which the frequency response of pumping depends on the channel and fluid properties, in addition to the pressure source. The approach exploited the electric-hydraulic analogy in which fluid conduits (channels or tubes) act as resistors (R) and inductors (L), and deformable features act as capacitors (C), allowing design of microfluidic circuits that mimic classic RLC electrical circuits in their resonance behavior when driven by harmonic (AC) pressure[30]–[32]. The Lutz group aimed to build on this work to engineer integrated pumps with resonance (pumping) frequencies in the audible range with a goal to enable flow control by common audio devices (e.g., iPhone)[33]. The devices used passive diffuser valves, like those from early piezo-driven micropumps, except that the resonance frequencies were governed by the channel properties rather than the piezo properties. Thus, a single piezo driver could be used to selectively excite individual channels (pumps) in an interconnected network. Using these passive valves, the resonance

frequencies were accurately predicted by simple RLC circuit models, and maximum DC pumping occurred at this same frequency.

In the follow-up work, the diaphragm-based fluidic diodes described by the Landers and Begley groups[30], [32] were used because they provided some degree of 'check-valve' function to limit cross-contamination in multi-channel networks needed for many biomedical applications. Since the goal was operation in the audible frequency range, stiffer material for the diaphragm and millimeter-sized channels were used to increase the resonance frequencies above 100 Hz. When testing these microfluidic pump devices with the diaphragm-based fluidic diodes, it was found that devices with slightly different designs exhibited the DC flow in opposite directions, and at frequencies that sometimes matched the model-predicted series RLC resonance frequency, but in other cases did not. It was necessary to understand how the DC flow direction and peak frequency were related to the RLC resonance frequency points and to use that knowledge to design microfluidic pumps that allow the DC flow to be reversed by switching the driving frequency.

5.1 DEVICE DESIGN

The schematic of a microfluidic pump device is shown in Figure 5.1 (a). Devices were fabricated by stacking laser-cut acrylic and Rohaglas sheets and pressure bonding them with PDMS tape. The acrylic sheet (light yellow) that defined the channels was capped by the deformable Rohaglas film (grey) on both sides. A stiff acrylic cap was added to the top and bottom to stiffen the channels, except that circular areas above the diaphragm regions (both the driver diaphragm and diode diaphragm) were cut out of the acrylic to allow the diaphragms to flex. The flexing allowed transient fluid storage, much like an electrical capacitor. A piezo buzzer was affixed to the larger diaphragm on the left to form the on-chip pressure source. The smaller passive diaphragm separating the upstream and downstream channels had a weir underneath it (Figure 5.1 (a) inset),

which acted as a fluidic diode for converting oscillating (AC) flow to steady (DC) flow[30], [32], [50].

In the implementation of Collino, *et al.*, the fluidic diode did not appear to contribute towards the frequency response; instead, the resonance frequency-determining elements (actuator tube, and capacitor) were upstream of the fluidic diode and off-chip[32]. DC flow in their devices was driven away from the pressure source, through the fluidic diode to the outlet. In the integrated devices, the fluidic diode plays an active role in affecting the frequency response, but there was no reason to expect a change in flow direction. The DC flow was expected in the same direction as Collino, *et al.* – away from the piezo buzzer[32].

For some devices, like the one shown in Figure 5.1 b (Device 1), DC flow in the expected direction was observed. Fluid moved away from the piezo buzzer pressure source, emptying Port 1 and filling Port 2. This work will refer to this direction (Port 1 to Port 2) as "forward". Peak forward DC flow was noted at the RLC-circuit-model-predicted series resonance frequency (650 Hz) predicted by the RLC circuit model. In another device of comparable dimensions (Device 2, Figure 5.1 (b) left); however, it was observed that the DC flow was in the opposite "backward" direction (Port 2 to Port 1). In addition to the opposite flow direction, the device demonstrated peak DC flow at a frequency (350 Hz), lower than the model-predicted series resonance frequency (510 Hz) predicted by the model. The RLC circuit model was used to understand the contrasting flow and frequency behavior from dimensionally and fluidically similar devices.

Figure 5.1 (c) shows a microfluidic device with its analog electrical circuit. Using the classic electric-hydraulic analogy, the piezo buzzer pressure source was represented by an equivalent electrical AC voltage source (P_{ac}) and the composite capacitance of the piezo buzzer and the diaphragm (C_p). Viscous drag and inertance of the fluid in the channel were represented as a series

combination of a passive resistor and inductor. The frequency-dependent resistance and inductance values (for example, R_u and L_u) were calculated using the exact impedance solution of the Navier-Stokes equation for harmonic flow.

The diaphragm above the weir is represented by the capacitor C_c in the electrical circuit model, and the weir and the capacitor combination is shown as a bi-directional diode. The diaphragm capacitance (C_c) was found by fitting the model to the observed AC flowrate peak frequency in devices without the weir, as shown in previous sections. Here, adding the weir reduces the effective diaphragm capacitance by preventing inward deflection and it was estimated as $C_c/2$. This assumption was verified by measuring the frequency response from two devices, one with the weir ($C_c/2$) and one without the weir (C_c), but otherwise similar. The decrease in the resonance frequency for the weir device matched model predictions using $C_c/2$ as the capacitance (see Supplementary Information Section 8.5).

Individual circuit elements were connected to create the RLC network model shown in Figure 5.1 (c). Atmospheric pressure points were considered analogs to electrical ground. Fluid ports at both ends of the device were sufficiently large in diameter to avoid affecting the circuit frequency response (see Supplementary Information Section 8.6). Mesh analysis was used to solve for the AC flowrate amplitude and phase for the frequency range of 0-1000 Hz. Throughout this paperwork, the AC flowrate 'amplitude', or just AC flowrate, refers to the time-independent, maximum magnitude of AC flowrate; it is denoted by Q and is the key value compared between the model and experiment. In contrast, the term 'magnitude' is used in specific cases to highlight time-dependent AC flowrate at a time point in the sinusoidal cycle, or to characterize DC flow. Subscript notations are used to denote AC flowrate amplitude in the channels, like in the case of upstream channel (Q_u), the downstream channel (Q_d), and the capacitor-diode (Q_c). Mass

conversation conservation requires that the three flowrate amplitudes add up to zero (*i.e.*, $Q_u + Q_d + Q_c = 0$) at the fluidic diode. The small channel connecting Port 1 to the piezo buzzer is parallel to the rest of the device, and therefore, the two branches can be treated independently. The further discussion will be focused on the right branch with the upstream, downstream channels and the diode.

Figure 5.1 (d) (left) shows the model-predicted upstream and downstream AC flowrate amplitude (Q_u and Q_d) for a range of actuation frequencies in a representative device. The preceding sections report that the circuit model accurately predicts the measured AC flowrates across this frequency range. The lowest frequency point of interest, f_o, is the series resonance associated with the large capacitor (C_p) connected to the piezo buzzer, and the small channel inductance (L_s); it can be calculated as $f_o = 1/(2\pi\sqrt{L_s C_p})$. In this work, C_p and L_s were kept essentially constant, thus f_o did not vary considerably (150-200 Hz). At this frequency, the flowrates upstream (blue arrow) and downstream (red arrow) are matched in magnitude and phase, resulting in no flow to through the capacitor-diode (black arrow), as illustrated in Figure 5.1 (d) right (for f_o), suggesting a possible reason why DC flow at f_o was not observed.

The series resonance frequency, f_s, is associated with the capacitor-diode C_c and the channel inductances L_u and L_d, and this is the location of the peak DC flow seen in previous work noted above[30], [32], as well as Figure 5.1 (Device 1). At a series resonance f_s, the total impedance to the pressure source becomes minimum, and the flowrates combine constructively to create a peak in the AC flowrate response. For example, in the device schematic in Figure 5.1 (d) (for f_s), the upstream AC flowrate magnitude (blue arrow) and downstream AC flowrate magnitude (red arrow) are equal in magnitude and opposite in phase, and add up to become the capacitor-diode AC flowrate magnitude (black arrow). While the depicted case shows the upstream AC flowrate

magnitude greater than downstream, in general, the relative flowrates are dependent on the upstream and downstream channel dimensions. The analytical expression for f_s is complex and includes resistance and inductance of both upstream and downstream channels and the capacitances of the piezo buzzer (C_p) and capacitor-diode (C_c). Simplified expressions for the special case of a large piezo capacitor ($C_p >> C_c$, as is the case here) are provided in the Supplementary Information Section 8.4. As a prominent peak in the AC flowrate response, the series resonance at f_s makes an ideal candidate for pumping due to its large AC flowrate amplitude, sharp roll-off, and ability to tune f_s via the capacitor-diode C_c and the channels.

The valley between the two peaks (f_o and f_s) is an interesting feature called the parallel resonance (f_p). Unlike a series resonance, where the impedance is minimum at resonance, at f_p, the impedance to the flow is maximum, which results in the upstream AC flowrate (Q_u) reducing to a minimum. Fluidically, this results from the flowrate magnitude downstream (red arrow) being equal and opposite to the flowrate magnitude in the capacitor-diode (black arrow), as shown by the middle device schematic in Figure 5.1 (d) right (for f_p). The interesting feature is that the downstream channel has a higher AC flowrate amplitude than the upstream channel that is directly driven by the pressure source. While this fluid-shuffling phenomenon ($Q_c = Q_d > Q_u$) may seem unphysical, it is an expected feature of the RLC circuit (see Supplementary Information Section 8.7), and the flowrate amplitude relationship ($Q_d > Q_u$) was observed experimentally in the device (see below). The most apparent effect of parallel resonance can be seen in the upstream channel ($Q_u \sim 0$), yet the resonance behavior originates from the parallel connection (hence the name) of the downstream inductance (L_d) and the capacitor-diode (C_c). Therefore, the parallel resonance frequency is simply given by $f_p = 1/(2\pi\sqrt{L_d C_c})$. Since, the parallel resonance manifests as a

valley (in contrast to a peak) in the AC flowrate response, it is easy to overlook, and at the face value does not appear to be a strong candidate for driving the DC flow.

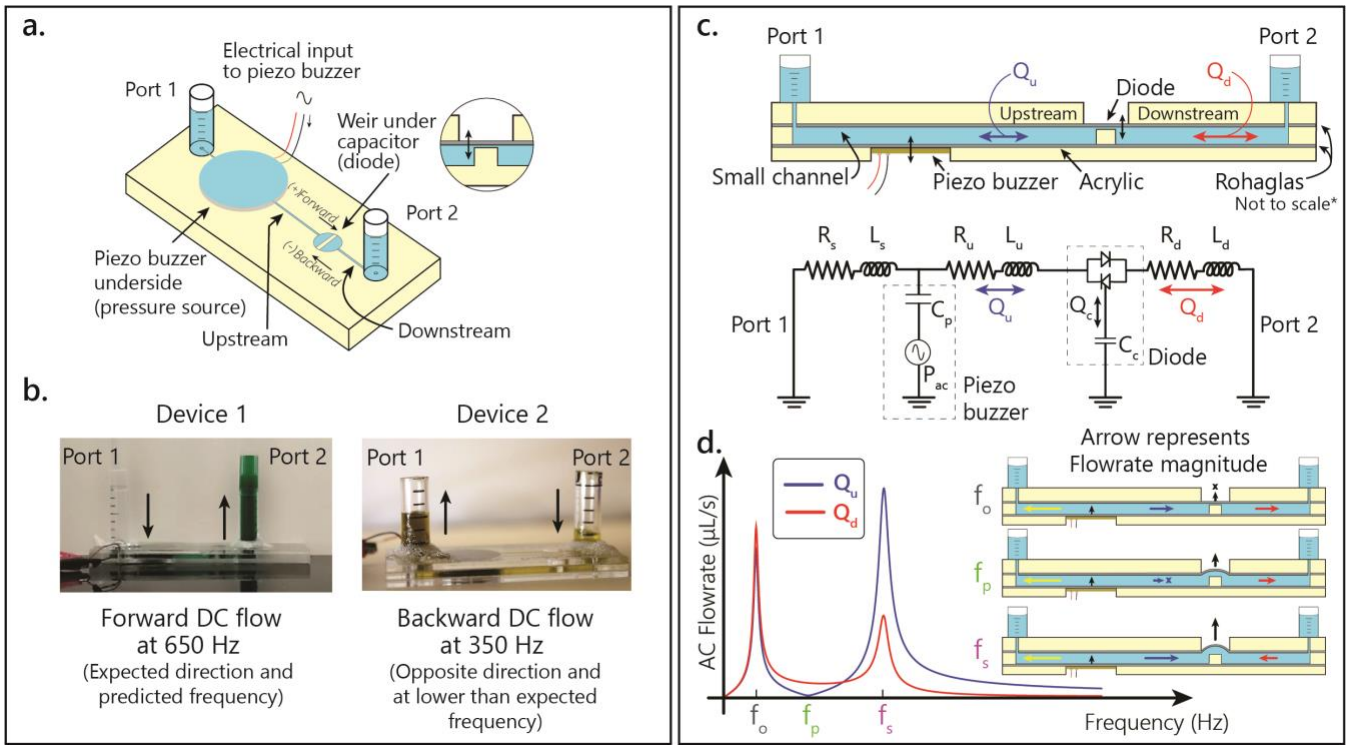

Figure 5.1. Microfluidic pump device: schematic, observed behavior, circuit model, and frequency response

Figure 5.1 **Extended Caption a.** Microfluidic pump device schematic (not to scale). Devices were made from stacking laser cut acrylic (light yellow) and Rohaglas (grey) parts. The middle acrylic part defined the channels (blue). Capacitors were the large circular parts of the channel with cutouts in the acrylic for the Rohaglas film to flex (inset). A piezo buzzer was affixed to the bigger capacitor to form the integrated AC pressure source. A weir was placed symmetrically under the smaller capacitor to make the fluidic diode. Ports at the either end of the device were made of cut pieces of 5.6 mm diameter serological pipettes (15 mL). Across all the devices, channels were 0.8 mm wide, and 1.5 mm deep, and the channel connecting Port 1 and the piezo buzzer was only 4 mm in length. The length of the upstream and downstream channel and the radius of the capacitor varied between devices. **b.** (left) DC flow in Device 1 was observed from Port 1 to Port 2 – "forward" direction. Maximum DC flow was observed at 650 Hz, which matched the electrical circuit model-predicted (series) resonance frequency. In Device 2, DC flow was observed in

the opposite, "backward", direction with peak flow at 350 Hz. The electrical circuit model predicted peak flow at the resonance frequency of 510 Hz, which did not match experiments and spawned this investigation. **c.** Side view of a microfluidic pump device and the corresponding electrical RLC circuit model. Upstream, downstream, and capacitor-diode AC flowrate amplitudes (indicated through bi-directional arrows) are denoted as Q_u (blue), Q_d (red) and Q_c (black), respectively. **d.** (left) Shows the AC flowrate amplitude frequency response (Q_c omitted for simplicity). The device schematics on the right are snapshots at varied time points during a sinusoidal cycle and are intended to qualitatively illustrate flow interactions at resonance frequencies. f_o is the series resonance and remained relatively unchanged between device designs; upstream and downstream flowrates were equal in magnitude and phase at any given time (directional arrows in device side view on right), resulting in no flow through the capacitor-diode. f_p, the parallel resonance frequency, manifests at the minimum in upstream channel due to fluid shuffling between the downstream channel and the capacitor-diode. f_s is the series resonance frequency; upstream and downstream flowrates add up to become the capacitor-diode flowrate. The yellow arrow is the flow lost to the Port 1; the AC flow to Port 1 remains relatively constant beyond f_o.

5.2 DEVICE FABRICATION

Microfluidic pump devices were fabricated by stacking laser-cut acrylic and Rohaglas parts and pressure bonding them with PDMS tape. The piezo buzzer was affixed to the large diaphragm of the same size using the PDMS tape. Thus, the annulus capacitance observed in prior work[32] was not present here. Channels were defined as features in the acrylic part. Channel depth was the same as the acrylic thickness (1.5 mm), and the channel width was kept fixed at 0.8 mm for all devices. The channel lengths and capacitor-diode sizes were the following: Device 1 – Upstream: 14 mm, Downstream: 10 mm, capacitor radius: 3 mm. Device 2 – Upstream: 12 mm, Downstream: 8 mm, capacitor radius: 4 mm. Bi-directional device – Upstream: 15 mm, Downstream: 10 mm, capacitor radius: 4.5 mm. The weir width was 2 mm and height 1.5 mm, and it was placed directly underneath the capacitor-diode. The fluid ports were sealed with super cyanoacrylate glue (Loctite #1363589).

5.3 DEVICE OPERATION

Devices were filled with saline solution (density = 1.05 g/mL) until the fluid ports on either side were a few millimeters in height. Food coloring was added as a visualization aid. A function generator (Wavetek Sweep Generator Model 134, Aeroflex Inc., Plainsville, NY, USA) supplied a sinusoidal electrical signal that was amplified to 50 V_{pp} by a custom audio amplifier (gain = 100, frequency range = 60-4000 Hz) for applying to the piezo buzzer.

5.4 DC FLOWRATE AND PRESSURE MEASUREMENT

Video was recorded using a Canon T3i DSLR camera. The DC flowrate was measured by programmatically estimating the time to pump 100 μL of the fluid (resolution of the serological pipette forming a fluid port). For measurement of stopped-flow DC pressure, at each frequency point, the DC flow was allowed to continue until the flow stopped due to the pressure head between the two ports. The stopped-flow DC pump pressure was measured as the difference between fluid heights of the Port 1 and Port 2.

5.5 AC FLOWRATE VISUALIZATION

Devices were filled with the same saline solution density-matched with suspended polystyrene fluorescent beads (Duke Scientific 5 μm Nile blue). The pump device was placed on an epifluorescence microscope (Zeiss IM35 with Retiga 1300i cooled camera). Images were captured after the stopped-flow DC pressure condition was achieved due to the forward or backward DC flow. Images were recorded near the channel centerline, and the exposure was made long enough to capture bead travel over many cycles of input sinusoidal signal. The images are programmatically analyzed in MATLAB to locate and measure the bead streak lengths.

5.6 RESULTS AND DISCUSSION

5.6.1 **Directional pumps**

The model-predicted frequency response of AC flowrate can be used to resolve the observation of opposite DC flow direction in the dimensionally-similar devices from Figure 5.1 (b). For Device 1 (the forward pumping device), the peak DC flowrate of 2.5 μL/s was observed at 650 Hz (Figure 5.2 a), which matches the model-predicted series resonance frequency f_s (650 Hz, Figure 5.2 b), as seen in the previous work[30], [32]. DC flow was not observed at f_p, nor at the resonance frequency associated with the piezo buzzer, f_o. A key observation from the model prediction is that at f_s, where the DC flow occurs, the upstream AC flowrate is much larger than the downstream AC flowrate ($Q_u >> Q_d$), while at f_o and f_p, where no DC flow occurs, the upstream and downstream AC flowrate amplitudes are comparable ($Q_u \sim Q_d$) or negligible ($Q_u \sim Q_d \sim 0$), respectively.

This prediction was experimentally tested by measuring the upstream and downstream AC flowrates by imaging fluorescent bead streaks at stopped-DC-flow conditions; at f_s (Figure 5.2 c), the measured upstream AC flowrate amplitude was much larger than the downstream AC flowrate amplitude ($Q_u >> Q_d$) as predicted by the model (see Supplementary Information Section 8.8 for measurements at f_o and f_p, which confirms the expected AC flowrate relationships for both frequencies). These observations suggest that a differential AC flowrate across the capacitor-diode may be a necessary condition for the net DC flow.

For Device 2, the peak DC flowrate of -−4.2 μL/s (negative indicates backward direction) occurred at 350 Hz (Figure 5.2 d), which is very close to the model-predicted parallel resonance frequency f_p (340 Hz, Figure 5.2 e). The model shows that at the parallel resonance in this device, the upstream AC flowrate is sharply reduced, but the downstream AC flowrate remains strong ($Q_u < Q_d >> 0$, see inset for s zoomed-in view). As the frequency increases to the series resonance f_s

(510 Hz), the upstream AC flowrate rises steeply and becomes comparable to the downstream AC flowrate ($Q_u \sim Q_d$). DC flow was not observed at f_s nor at f_o.

AC flow visualization images verify the flowrate relationship ($Q_u < Q_d >> 0$) at parallel resonance (Figure 5.2 (e); see Supplementary Information Section 8.8 for measurements confirming $Q_u \sim Q_d$ at f_o and f_s). Stationary beads upstream indicate no AC flow, while there is substantial AC flow in the downstream channel further away from the pressure source. Fluid shuffles back-and-forth between the capacitor-diode and the downstream channel, while the upstream channel nearest the pressure source shows no measurable AC flow. The seemingly unphysical behavior is predicted by the model (see phase response in Supplementary Information Section 8.7 for the complete picture) and is directly observed in experiments. These observations suggest that the direction of AC flowrate differential across the capacitor-diode (high to low) may determine the direction of the DC flow.

To reiterate, Device 1 exhibited peak DC flow in the forward direction at the series resonance and no flow at the parallel resonance. In contrast, Device 2 showed backward DC flow with the peak at the parallel resonance and no flow at the series resonance. These observations suggest that a differential in the AC flowrate across the capacitor-diode may be necessary to generate the DC flow, and the direction of the DC flow may follow the direction of the AC flow differential (high to low). To test the hypothesis, the circuit model was involved employed to design a single device that was predicted to have large AC flowrate differentials in opposite directions at the series and parallel resonance frequencies. The result was the bi-directional pump device.

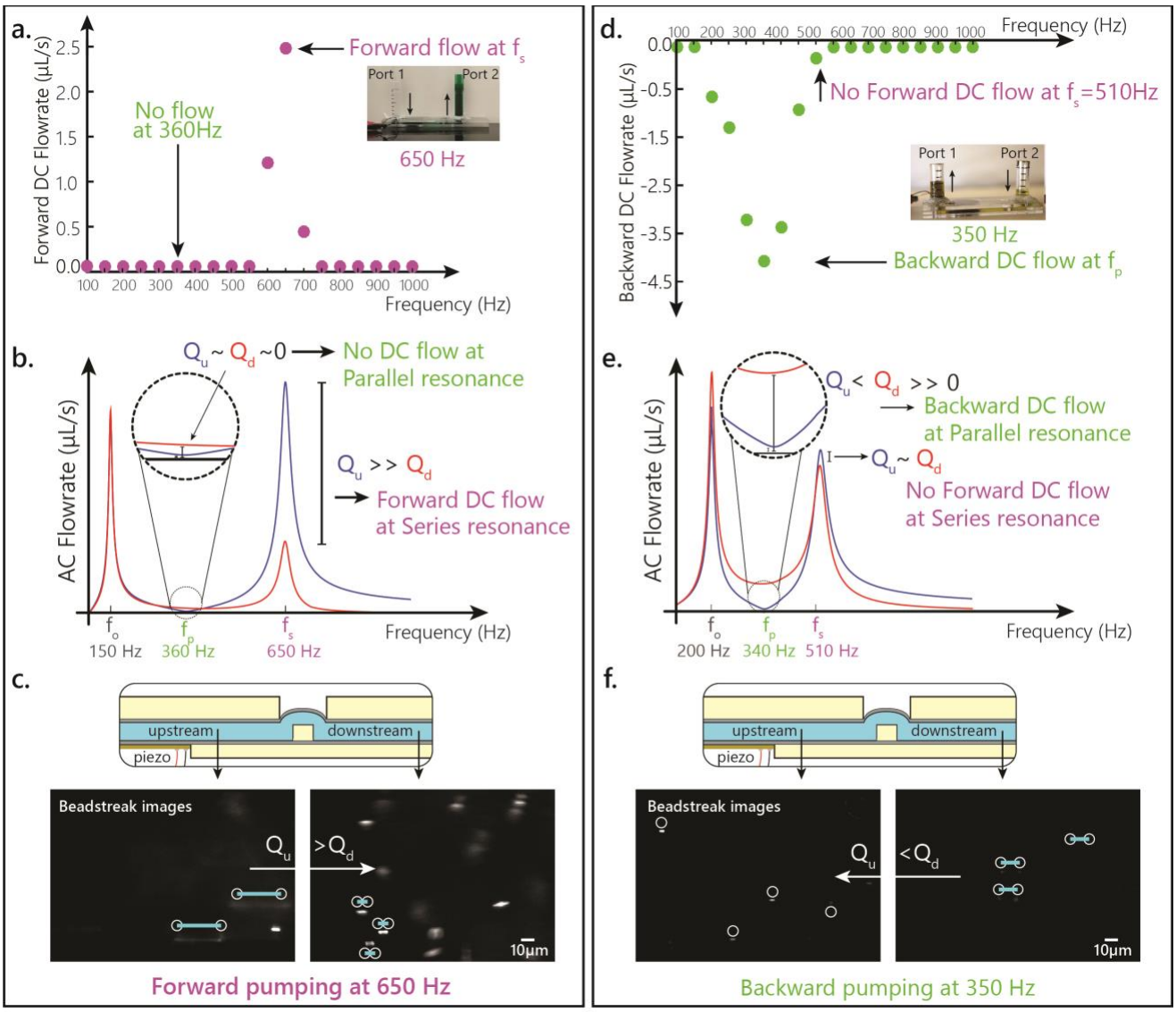

Figure 5.2. Directional pumping devices

Figure 5.2 **Extended Caption a.** DC flow in Device 1 was observed in the forward direction (Port 1 to Port 2). The peak DC flow frequency was at 650 Hz. The inset shows the stopped-DC pressure (18.4 mm H_20, see frequency response in Supplementary Information Section 8.9) due to the forward flow at 650 Hz. **b.** The model AC flowrate frequency response shows the series resonance f_s at 650 Hz with a greater AC flowrate amplitude upstream compared to downstream ($Q_u > Q_d$). **c.** The AC flow visualization images validated the model prediction by showing higher AC flowrate amplitude upstream (longer bead streaks) than downstream at the series resonance f_s. No DC flow was observed at f_o (150 Hz) and f_p (360 Hz). The model AC flowrate frequency responses show $Q_u = Q_d$ at f_o and $Q_u \sim Q_d$

~ 0 at f_p (inset). (right pane) **d.** In Device 2, backward DC flow (negative magnitude) in the direction Port 2 to Port 1 was noted. The inset shows stopped-DC pressure (4.9 mm H_20) due to backward flow at the peak DC flow frequency (350 Hz). **e.** In this case, f_s (510 Hz) did not coincide with the peak DC flow frequency. Instead the peak DC flow was observed about the parallel resonance (340 Hz). Unlike Device 1, here the parallel resonance valley was steep, and while the flowrate upstream reduced around f_p, flow downstream was maintained ($Q_u < Q_d$, inset) **f.** The model-predicted AC flowrate relationship was validated through the AC flow visualization images obtained at 350 Hz. The upstream channel had stationary beads (no flow), while there was substantial AC flow amplitude in the downstream channel. DC flowrate plots (a. and d.) were generated from one measurement in each device, and are presented as observational cases that led us to the design hypothesis for bi-directional pumps. Pumping videos for the two devices are included in the publication[43].

5.6.2 **Bi-directional pumps**

To test the design hypothesis for a bi-directional pump, an optimization model in MATLAB (ver. 2014b, The Mathworks Inc., Natick MA) with the objective to independently maximize Q_d/Q_u at f_p (to provide backward flow) and maximize Q_u/Q_d at f_s (to provide forward flow) was setup. The inputs to the solver were expressions for the flowrates in terms of resistance and impedance of the channels and expressions for resonance frequencies. Analytical expressions for the resonance frequencies were derived by minimizing (or maximizing) the corresponding impedance functions for the series (or parallel) resonant circuits (see Supplementary Information Section 8.4). Constraints were set as the range of resistance and inductance available through varying only the channel length (channel depth and width fixed at 1.5 mm and 0.8 mm respectively). The optimization model output was resistance and inductance values for upstream and downstream channels, which were used to back-calculate the length of the upstream and downstream channels.

The resulting AC flowrate response from the circuit model reflected the goals of the optimization model (Figure 5.3 a). At the model-predicted f_p (300 Hz), the upstream AC flowrate

is smaller than downstream ($Q_u < Q_d$). Similarly, experiments (Figure 5.3 b) show some AC flow downstream (bead streaks), but no measurable flow upstream (stationary beads). At the model-predicted f_s (480 Hz), the AC flowrate differential is reversed ($Q_u > Q_d$), and this was confirmed by experiments (Figure 5.3 b, longer streaks noted in the upstream channel). Thus, the designed device successfully combines the two AC flowrate conditions observed separately in the forward and backward directional pumps (Device 1 and Device 2), and it was expected to be able to select the backward DC flow or forward DC flow from the same device by operating at f_p and f_s, respectively.

Figure 5.3 (c) shows the DC flowrate response for a designed bi-directional pump (a total of three identical devices were fabricated and tested). The peak backward DC flowrate of -−2.2 μL/s was seen at 280 Hz (model-predicted f_p = 300 Hz). The peak forward DC flowrate of +3.5 μL/s was seen at 490 Hz (model-predicted f_s = 480 Hz). The difference of few tens of Hz between the model prediction and the observed frequency is common in these devices due to fabrication differences; the match between the model-predicted frequencies and peak DC flowrates is remarkable. While the model does not allow prediction of the shape of the DC flowrate peaks, the experiments show that the two peaks are distinct and show no overlap. Importantly, this result showed that the phenomenological relationship identified above allows prediction of the existence and frequency dependence of DC flow reversal in a single device.

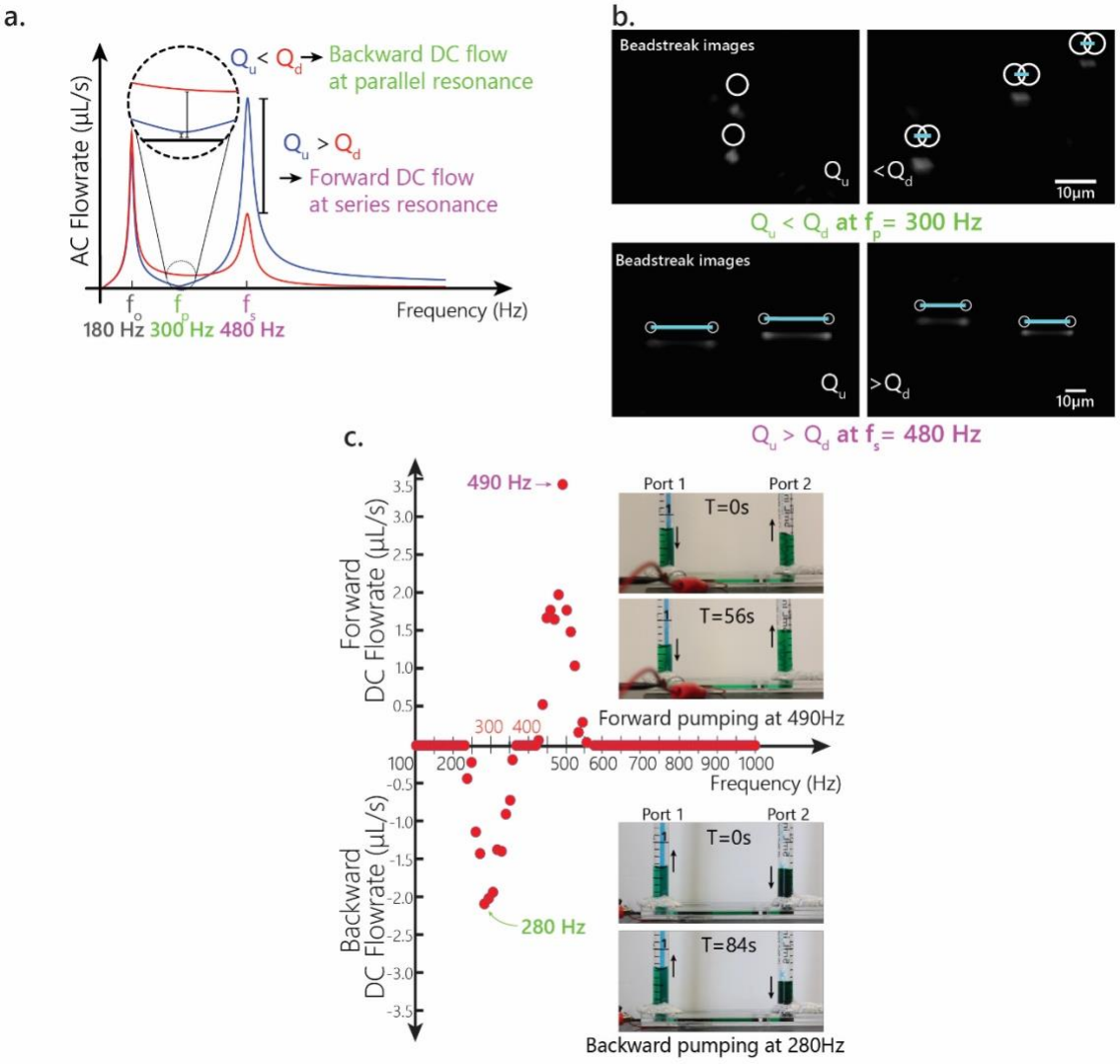

Figure 5.3. Bi-directional pumping device

Figure 5.3 **Extended Caption a**. Model-predicted AC flowrate depicts a large difference in Q_u and Q_d at f_p (300 Hz) and f_s (480 Hz). The AC flowrate differential is opposite at the two frequencies indicating opposite DC flow direction at the two resonance frequencies. **b.** AC flow images verified the model-predicted AC flow relationship at f_p ($Q_u < Q_d$) and f_s ($Q_u > Q_d$). **c.** Three devices of the same design were fabricated and tested, and a single curve is plotted here for clarity. In three identical devices, peak backward pumping was observed at frequencies of at 280 Hz, 320 Hz and 330 Hz (model predicted f_p = 300 Hz) with the peak backward flowrates of -2.2 µL/s, -1.8 µL/s and -2.4 µL/s, respectively. The peak forward pumping frequencies were 490 Hz, 500 Hz and 490 Hz (model predicted f_s = 480 Hz) and peak forward flowrates were of 3.5 µL/s, 2.5 µL/s and 2.9 µL/s. Insets show changes in fluid level in the

ports with the DC flow. Before every run, the fluid levels were allowed to hydrostatically balance (t = 0). The frequency was applied until the flow stopped due to the difference in the fluid columns. Forward flow at 480 Hz stopped at t = 56 secs (difference in fluid column, or stopped-flow DC pressure = 3.8 mm H_2O). Backward flow at 290 Hz stopped at t = 84 secs from a stopped-flow DC pressure of 4.2 mm H_2O. The images are from the same device run. The color difference in the two fluid columns, particularly apparent in the backward flow images, eventually faded as the fluids mixed due to pumping.

5.7 CONCLUSION

To the author's knowledge, there are at least two accounts of reversed flow in piezo-driven micropumps[51], [52]. In both cases, the behavior was briefly noted but not explained, and the information presented is insufficient to test against the author's observations. In addition, those pumps were driven at ultrasonic frequencies, where fluid compression and standing/traveling pressure wave are created, so the physical process in those devices may be completely different than from that observed here (low-frequency oscillatory flow of an incompressible fluid).

It was demonstrated here that a hypothesis based on observations could be used to design a device to give the backward DC flow at parallel resonance and the forward DC flow at series resonance. If the design hypothesis is true – that the DC flow direction follows the direction of AC flowrate differential – then devices could be designed to give flow reversal with the opposite frequency arrangement. Specifically, devices could be designed for $Q_u < Q_d$ at the series resonance to drive backward flow, and $Q_u > Q_d$ at the parallel resonance to drive forward flow (but only with smaller channel dimensions than possible to fabricate by the methods disclosed here; see analytical solution in Supplementary Information Section 8.10).

Here it was reported that frequency tuning can control the magnitude and direction of the rectified DC flow in microfluidics networks with a fluidic diode and passive features. A simple, qualitative connection between the observed direction of the DC flow and the AC flowrate

differential in the channels separated by the fluidic diode was provided. This knowledge was utilized to demonstrate bi-directional, frequency-tuned pumps. On-demand flow direction switching using simple hardware like a piezo buzzer could be useful for lab-on-a-chip applications. For example, flow reversibility might be used in flow-through PCR devices to shuffle sample back and forth between the hot and cold zones, in surface-capture-based processes such as binding arrays or sample processing where multiple passes and mixing could increase capture efficiency, or for manipulation of droplets or cells in cytometry operations.

The qualitative connection and the electrical model should serve as a sufficient design tool, yet further research is needed to design efficient directional pumps. Understanding the physical origin of the flow directionality is one such opportunity. It is the understanding of the author that flow directionality is derived from the phase difference between the flows in the fluidic diode and the flexing of the diaphragm that makes the diode. For someone seeking to validate this theory, the electrical circuit model presented here provides a useful starting point. Measurements of the phase of the flow through the channels and the capacitor-diode can be obtained using particle velocimetry in conjugation with an optical or capacitive vibration sensor respectively. Also, since fluidic diodes are known to exhibit a non-linear pressure-flowrate relationship[50], there may also exist a rectification threshold (like electrical diodes), related to the AC flowrate differential in the channels separated by the diode, below which the DC flow is not realized. The complex solid-fluid dynamics at play in the fluidic diode may be the key to understanding this behavior.

To summarize, this chapter: (i) describes the series and parallel resonance behavior in microfluidic pump devices using a predictive electrical circuit model, (ii) connects the resonance frequencies to the different DC flow directions through the AC flowrate differential in the channels separated by the diode, and (iii) utilizes an optimization approach capitalizing on the AC flowrate

differential to design a bi-directional, frequency-tuned, microfluidic pump. The findings and approach presented here provide a novel pathway to miniaturize the flow magnitude and direction control for lab-on-a-chip and microTAS applications.

Chapter 6. COUPLING ELASTIC CHANGES IN BLOOD CLOTTING TO RESONANT BEHAVIOR

Blood coagulation is a dynamic biological process that stops bleeding. When a blood vessel is injured, it is vital that the site be sealed with a clot. This blood clot prevents further loss of blood as well as preventing protects against entry of foreign pathogens into the circulatory system. The clotting process is complex feedback system with a multitude of enzymes (clotting factors), cells, cellular derivatives, and adhesion proteins that maintain a delicate balance between clot initiation, formation, strengthening, contraction, and lysis. The individual components of the coagulation system influencing these clotting processes can be measured either through biochemical tests, like immunoassays that provide activities and levels of clotting factors or platelets, or functional tests, like Thromboelastography (TEG) and Rotational TEG (ROTEM), that measures the viscoelastic changes as the blood clots[53]. The viscous and elastic measures of blood clotting are functionally indicative of the rheological progress of hemostasis. Since functional tests provide a system response, they tend to be more clinically relevant than activity assays, which often are a victim of their specificity. An example is the Factor VIII (FVIII) activity assay currently used in the monitoring of the expensive FVIII substitution therapy in hemophilia (FVIII-deficiency) patients. The activity levels from the chromogenic immunoassay underestimate the impact on overall hemostasis as measured by functional, viscoelastic tests[54]. This has resulted in the common clinical practice of over-prescribing the substitution FVIII therapy than what is needed for restoring normal blood clotting[55]. A simple correction factor relating FVIII activity to normalize hemostasis has been proposed, however its efficacy has been debated due to the varying individual clotting phenotypes[56]. Therefore, there is a clinical need for POC viscoelastic functional test.

An immediate application for such a test could be in monitoring of FVIII activity in hemophilic patients undergoing FVIII substitution therapy.

6.1 OVERVIEW OF BLOOD COAGULATION SYSTEM

Blood coagulation has evolved as vital defense mechanism against bleeding and subsequent pathological infections. Under normal conditions, the complex coagulation system is balanced in favor of anticoagulation. The coagulation system is instantly triggered in response to an endothelial injury that exposes blood to extravascular tissue. The leaking of blood through the endothelial initiates two processes: activation of platelets through exposure to collagen in the extravascular tissue and plasma FVII activation through the contact of sub-endothelial tissue factor, which ultimately leads to fibrinogen-fibrin conversion. Fibrin is the primary structural protein in blood clots and provides the scaffold for wound repair[57]. Fibrin polymerizes and provides the elasticity and stiffness to the clot to plug the leak while withstanding the forces exerted by the flowing blood and the embedded cells[58]. The crosslinking reaction between polymerized fibrin fibers assisted in the presence of platelets results in contraction and increased rigidity of the clot. In parallel to clot formation and maturation, the regulatory process of fibrinolysis prevents the blood clot from growing and becoming problematic. Even a slight imbalance between the complex processes involving clot formation and degradation from genetics, acquired immunity, pharmacological factors, trauma and surgery may result in a coagulopathic bleeding[59].

6.1.1 **Coagulation cascade**

The intrinsic pathway of the blood coagulation system is triggered by the activation of FXII on negatively charged foreign surfaces[60]. Activated FXII serves as a catalyst of a series of chemical reactions that results in eventual conversion of prothrombin to thrombin as shown in Figure

6.1[61]. The intrinsic pathway plays a minor role in hemostasis as evidenced by lack of bleeding disorder in patients with deficiency of FXII[62]. Instead, the intrinsic pathway is more involved in immune response and inflammation[63].

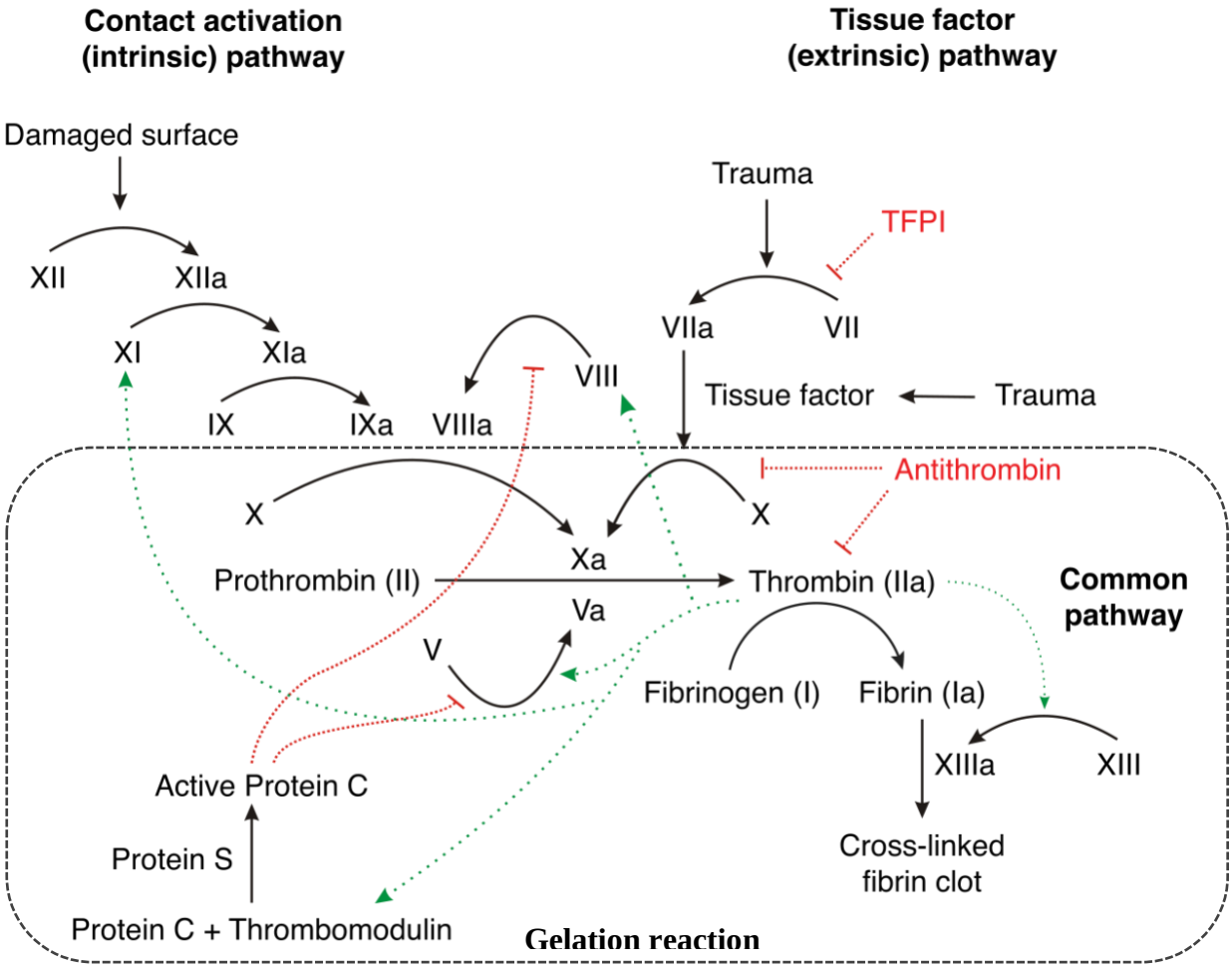

Figure 6.1. Coagulation cascade (adapted from [64])

On the other hand, the extrinsic pathway is initiated by FVII and tissue factor (TF). Following a trauma, such as an injury to a blood vessel, FVII comes into contract with TF and forms the TF-FVIIa complex. The complex activates FX and its co-factor FVa which forms the prothrombinase complex. The prothrombinase complex then sequentially catalyzes the conversion of prothrombin to thrombin. Thrombin is essential for conversion of fibrinogen to fibrin as well for activation of

other components of the coagulation cascade including FVIII and further activation of FV. FVIII is usually bound to Von Willebrand factor (vWF) and gets released in the activated form in presence of Thrombin. FVIIIa is the co-factor for FIXa and together they form the complex which further initiates the intrinsic pathway for FX activation and eventual thrombin generation through the common pathway. Thrombin also activates the FXIII, which is essential to the mechanical strength to the fibrin clot. Fibrin monomers are covalently crosslinked in presence of FXIIIa which results in a mechanically stable clot[65]. The covalent crosslinking of fibrin monomers in presence of FXIII manifests as an increase in the elastic modulus of the fibrin clot[66]. Platelets also interact with the coagulation cascade. Activated platelets provide an alternate to the intrinsic pathway that bypasses FXII[67]. Platelets are also known to form pseudo-crosslinking with fibrin fibers, which increases the rigidity modulus of the clot (output of TEG) and clot retraction[68]. Tissue factor pathway inhibitor (TFPI) and antithrombin are the two most active regulators that keep the coagulation cascade in check. Antithrombin is the key factor modulated by anti-coagulation drugs like heparin. Once the blood clot has served its purpose of providing a platform for wound repair, the clot is slowly resorbed through the process of fibrinolysis. The primary enzyme ins fibrinolysis is plasmin which is generated by proteolytic cleavage of plasminogen protein generated by the liver.

6.1.2 **Common coagulation disorders**

Deficiency of clotting factors or other components of the clotting cascade, like fibrinogen and prothrombin results in rare and inherited disorders. A comprehensive review of coagulation disorders is not provided in this work but available in the following reference[69]. Some common disorders are described in detail below.

Congenital afibrinogenemia is an autosomal recessive disorder associated with lack of Fibrinogen in the blood. The disease results in inability of blood to clot which results in an elevated Prothrombin time (PT). Conclusive diagnosis is based on family history and genetic testing. The disease is rare (1 in 1 million) and is treated through routine transfusions of blood plasma or cryoprecipitate.

Congenital Thrombophilia is the inborn condition that increases the risk to develop thrombosis. This most common type of this disorder arises from a mutation in Prothrombin. This results in a lack of regulatory effect of antithrombin. A PT test may be normal, therefore this disease is often diagnosed through viscoelastic tests like TEG and ROTEM, as they provide measures of clot strength and maturity, both of which would be elevated in patients with this disorder. The disorder could be fatal because the patients may suffer recurrent venous thrombosis and pulmonary embolism. Patients are managed through a high-dose heparin anticoagulant therapy. Heparin enhances the antithrombin activity and keeps the coagulation system in check.

The most common clotting factor deficiency is associated with lack of FVIII and is called Hemophilia A (HA). HA is inherited as an X-linked recessive trait, which causes increased bleeding. HA presents at a young age and usually affects males (1 in 5000). PT, which measures the speed of the extrinsic pathway of coagulation, does not detect HA. Activated partial thromboplastin time (aPTT or PTT) is the diagnostic test to evaluate the speed of the intrinsic pathway and results in elevated PTT for patients with HA[70]. Often genetic testing and family history is used for conclusive diagnostics. FVIII substitution therapy may be used to treat and prevent bleeding in patients with HA. Deficiency of FIX and FXI are called Hemophilia B and Hemophilia C respectively and are even more rare than HA.

Acquired Hemophilia A (AHA) is an auto-immune disorder caused by antibody generation to FVIII. AHA has an estimated incidence of 1.5 per million per year[71]. An estimated 3000 patients in the US suffered from AHA in 2015[72]. The disease commonly has high mortality and morbidity as it occurs in older patients with other underlying auto-immune disorders or with suppressed immune systems[73]–[75]. Patients show signs of bleeding, ranging from life to limb threatening, with no family history of bleeding disorders. The disorder does not affect PT time, but results in isolated prolonged aPTT. A prolonged aPTT may be due to deficiency of any factor (FVIII, IX, XI or XII) in the intrinsic pathway or indicate an inhibitory antibody, hence a confirmatory activity level assay needs to be performed[76]. Early recognition, rapid diagnosis and referral to a specialized hemophilia center is key to improved outcomes. Patients often receive immunosuppression therapy immediately after diagnosis. Since the optimal strategy of antibody eradication is not yet developed and tested, patients require routine substitution therapy for FVIII[73]. Patients undergoing FVIII substitution therapy are daily monitored on an outpatient basis that includes physical examination, hemogram, aPTT, and FVIII activity chromogenic assay. This often results in patients having to relocate temporarily closer to specialized hemophilia centers. Even though AHA is a rare but fatal disorder that affects the elderly, it is a major healthcare expense ($300k per patient per year in the US) because of the cost of substitution therapy and need for routine monitoring[74].

6.1.3 **Coagulation testing**

Blood clotting tests are used to assess the efficacy of the coagulation cascade or the hemostasis system. These tests are broadly classified into two categories 1. global tests and 2. local tests. Global tests are functional tests that evaluate the overall efficacy of the coagulation cascade. Viscoelastic tests like TEG, ROTEM, Sonoclot®, and ReoRox® are common measures that

provide the various measures of clotting efficacy like clotting time, dynamics, lysis and clot mechanical properties like rigidity (TEG/ROTEM) or viscosity and elasticity (ReoRox®). Local tests refer to the diagnostic tests that measure or evaluate the efficacy or speed of specific components of the coagulation cascade. Some examples are PT and aPTT which measure the speed of the extrinsic and intrinsic coagulation pathways respectively. Other examples of local tests are specific factor tests like thrombin generation test (TGT) and chromogenic assays like Coamatic FVIII®.

6.1.3.1 Global tests

Overall coagulation efficacy measurement is primarily performed in surgery, anesthesiology and trauma settings. Coagulation efficacy is measured as viscoelastic changes in blood clotting. The equipment resembles a crude version of plate and cone viscometer common in rheology testing facilities. TEG is one of the most common viscoelastic tests for hemostasis measurement. The basic principle has a small sample of whole blood is placed in a cup and rotated to imitate sluggish, venous flow and activate coagulation as shown in Figure 6.2 (a). A thin torsional wire is placed in the cup. As the blood clots, the rotational force exerted by the cup is coupled to the wire through the polymerized fibrin. The deflection of the wire measured through various means (magnetic, optical, strain) is plotted against time as shown in Figure 6.2 (b). ROTEM is another version of TEG in which the wire is replaced by the shaft and is rotated instead of the cup. A commercial TEG equipment (TEG 5000 by Haemonetics) is shown in Figure 6.2 (c).

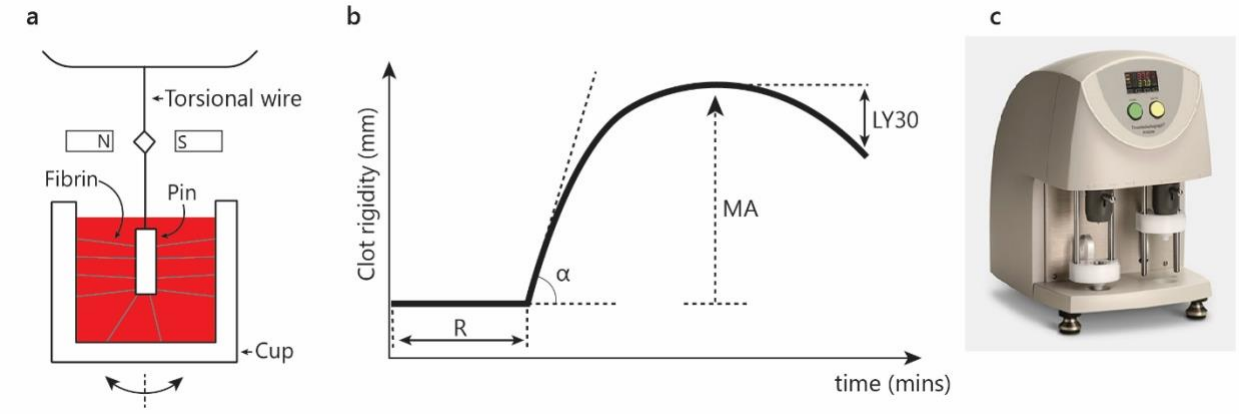

Figure 6.2. TEG: basic operating principle and sample plot

This macroscopic measure of clot formation provides four values of diagnostic importance as shown in Figure 6.2 (b). The R-value represents the time to clot initiation. Rheological investigations indicate that clot initiation in TEG marks the conversion of fibrinogen to fibrin monomer[77] and is a reflection of clotting factor activity. A prolonged R-value often requires plasma transfusion[78]. The alpha angle (α) is the angle between the tangent to the clot rigidity curve and the baseline activity. α is indicative of the clot kinetics as fibrin polymerizes and crosslinks in presence of FXIII. A depressed alpha angle may be treated with either cryoprecipitate or plasma. MA (maximum amplitude) is the measure of clot strength. By this time, the fibrin polymerization and crosslinking has completed (20% contribution) and platelets have further strengthened the clot through pseudo-crosslinking (80% contribution)[67]. Reduced MA indicates loss of clot integrity and may require treatment for FVIII substitution or platelet transfusion. Clot lysis is reported as % of clot lysed in 30 mins (LY30) as indicated by post-maturation loss in clot strength. An elevated LY30 suggests hyperfibrinolysis and may be treated with tranexamic acid (tPA)[79]. Parameters reported by ROTEM whole blood analyzer (Tem Innovations GmbH, Munich) are similar in the diagnostic information despite being named differently. A typical TEG runtime is 45-60 mins and costs $5-10 for disposables[80].

While traditional TEG is used for global assessment of the coagulation cascade, differential assays using specialized reagents have been developed for ROTEM to provide local diagnostic information pertaining to specific clotting factors and other components of the clotting cascade. For example, INTEM assay measures the clotting efficacy of the intrinsic pathway. Heparin is added to the sample to increase antithrombin activity and block the extrinsic pathway. EXTEM is the screening assay for extrinsic pathway and uses an anti-thrombin inhibitor (anti-heparin) to overdrive the extrinsic coagulation pathway. FIBTEM is an EXTEM derivative assay for measuring the fibrin gelation. FIBTEM uses platelet inhibitors in the sample to measure the clot strength (MA) due to fibrin polymerization and crosslinking. FIBTEM assays are used for confirmatory diagnosis of fibrinogen deficiency. APTEM is another EXTEM-based assay in which fibrinolysis is prevented by anti-fibrinolytic drug. A significant difference in the clot lysis between APTEM and EXTEM conclusively detect hyperfibrinolysis.

Compared to TEG and ROTEM viscoelastic tests, which offer a measure of the clot rigidity (modulus), ReoRox® (MediRox AB, Sweden) provides direct measurements of the viscosity and elasticity changes with blood clotting. The concept is based on an established industrial polymer characterization technique called free-oscillation rheometry (FOR). In this technique, the cup containing the whole blood sample is allowed to freely oscillate about a stationary torsional wire. As the blood clots, the change in natural (relaxation) frequency of the oscillation and increased dampening provides measure of elasticity and viscosity increase. Figure 6.3 compares sample output trace from ReoRox to ROTEM. COT1 and COT 2 mark the start and end of clotting as indicated by the change in viscous or loss modulus (G″) of the clot. The change in G″ is due to an increase in dynamic viscosity from the fibrinogen to fibrin conversion and subsequent polymerization of fibrin[66]. The increase in elastic modulus (G′) of the clot follows the viscous

changes and have been attributed to the crosslinking reaction between the fibrin fibers, which results in formation of a network. Elasticity of the clot further increases with lateral association of fibrin fibers[66]. Differential assays, like those for ROTEM, have been developed for ReoRox. Figure 6.3 (A) shows the difference in elastic modulus (G′) between Fibscreen1 (with platelets) and Fibscreen2 (platelets-inhibited) as compared to ROTEM assay EXTEM (with platelets) and FIBTEM (platelets-inhibited) in Figure 6.3 (B)[81]. The ReoRox output is not easily convertible to the conventional TEG-like traces, which are well recognized in the clinical community. Despite this limitation, ReoRox® has garnered significant clinical and research attention. However, a few studies have evaluated the correlation between ReoRox and TEG/ROTEM parameters and the results are mixed[81]–[83].

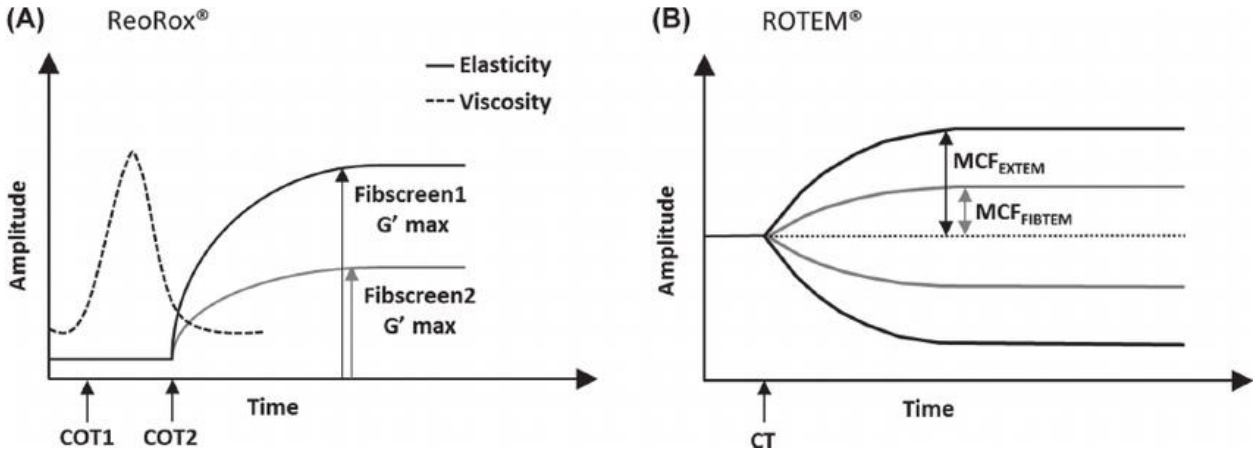

Figure 6.3. ReoRox compared to ROTEM (adapted from [81])

Viscoelastic measures of blood clotting are essential for functional testing of the coagulation cascade. TEG and ROTEM provide valuable clinical information in a surgery suite or a research lab, but these expensive, benchtop tools are simply not designed to be used in the field where most bleeding mortality takes place. A portable TEG system would have large impact for trauma care in the US, and the WHO has identified TEG as an “essential medical device” for global health[84].

6.1.3.2 Local tests (PT/INR and aPTT)

Clot-based tests provide a measure of the local coagulation function and are primarily used for routine monitoring of anticoagulation therapy. These simple tests are single-step, easy to perform, use minimum reagents, and instrumentation. The results of these tests include the prothrombin time (PT), activated partial thromboplastin time (aPTT), and activated clotting time (ACT). Out of ordinary values for these measures indicate that the patient may needs to adjust have the anticoagulation drug dosage adjusted.

PT is the most common measure for clotting activity of patients who take warfarin, the oral anticoagulant. PT measurement typically requires adding thromboplastin (plasma protein aiding in blood coagulation) and calcium citrate to blood plasma and measuring the time to clotting. Typical, PT values are between 10-14 secs[85]. Since thromboplastin reagents vary their activity due to different sources, each manufacturer is required to report an international sensitivity index for their batch, which is used to normalize the PT value and generate the international normalized ratio (INR). The clinical utility of aPTT is for patients undergoing an intravenous anticoagulation therapy of heparin. aPTT measures the intrinsic pathway of the coagulation cascade, whereas PT was measuring the extrinsic pathway[85]. The reagent used for aPTT is called partial thromboplastic, and it refers to the phospholipid in the reagent, which lacks tissue factor. aPTT is a multi-step assay that requires the addition of a surface activator and diluted phospholipid to citrated plasma, incubation, the addition of calcium and then the measurement of clotting time. Typical, aPTT values are between 22-40 secs[85].

ACT measurement is usually used in surgeries for monitoring anticoagulant therapies. Perioperative monitoring of blood coagulation is critical to reduce risk of hemorrhage during surgery, to guide hemostatic therapies and to prevent bleeding post-surgery. PT and aPTT

measurements have been shown to have limited diagnostic values in acute perioperative settings[86]. ACT assay can be complex, time-consuming and the advent of viscoelastic whole blood analyzers like TEG and ROTEM is slowly phasing out ACT from surgery rooms[87]. In addition to providing clotting times, TEG and ROTEM provide information about clot kinetics, integrity and fibrinolysis, which PT and aPTT lack. However, the diagnostic utility of these measurements is limited to trauma settings[88] and surgery rooms to evaluate transfusion requirements[89] and in diagnosis of rare diseases like the AHA[90] and acquired and inherited blood disorders[91]. The value of TEG and ROTEM measurements are in providing insights into clot growth and retraction, after the clot has already formed[54]. But, since the role of an anti-coagulation drug is in limiting clot formation, the information provided by TEG and ROTEM measurements are excessive for checking clotting activity alone. Hence, the utility of TEG and ROTEM measurements may not be needed for routine in-home testing of clotting activity.

PT, aPTT, and ACT measure clotting times after their specific reagents are added. Various methods have been developed to measure the clot presence like, optical transmission[92], reflectance[92], electromechanically[93] and impedance measurements[94]. There are also POC PT/INR monitoring systems that patients can use at home to monitor their coagulation activity in response to warfarin. These include the INRatio2®, Protime Microcoagulation System, and CoaguChek®. The INRatio2 uses capillary microfluidics to expose the whole blood sample to a pair of electrodes and measures the change in impedance with clotting[95]. The device itself can be battery powered or line-powered but costs hundreds to thousands of dollars. The line-powered Protime Microcoagulation System pumps blood back and forth through microchannels coated with dried reagents. The change in harmonic flow is detected using LEDs to measure clot formation. CoaguChek, a battery-powered handheld device, measures PT/INR by an electrochemical signal

generated during coagulation. The key point is that there are plenty of options available for at-home PT/INR testing.

6.2 RHEOLOGY OF BLOOD COAGULATION

Blood is a viscoelastic, non-Newtonian fluid. The viscosity of blood is shear-dependent and reduces with shear (shear-thinning), a property essential for efficient perfusion of micro-capillaries (Fahraeus-Lindquist Effect)[96]. The molecular origin of shear-thinning of blood stems from the ability of red blood cells (RBCs) to form aggregates at low shear rates and rearrange and orient as the shear rate increases. RBCs are also responsible for the elasticity of blood. RBCs stretch and align to provide channels for plasma to flow through the vessels. While whole blood is viscoelastic fluid, blood derivatives that are devoid of RBCs, like platelet-rich plasma (PRP), platelet-free plasma (PFP), plasma and serum, can be considered as viscous and Newtonian fluids for most practical purposes[97]. As these blood derivatives clot, the viscosity increases and the elasticity is introduced again through fibrin gelation and crosslinking. The crosslinking of fibrin monomers in presence of FXIII is essential to clot integrity and was the focus of the rheological investigation in this work.

6.2.1 **Fibrin gel mechanics**

Fibrin gels provide the mechanical strength to blood clots. These gels are the most resilient protein polymer structures in nature[98]. Rheological investigation of fibrin gels is usually performed using stress-controlled rheometers. A sample of fibrin gel is placed between parallel plates, one of which is driven in sinusoidal oscillatory motion of fixed amplitude and frequency. The force acting on the other plate is the proportional to the rigidity modulus ($G^* = G' + iG''$). The in-phase component of the stress response is the elastic modulus (G') and the out-of-phase component is

the viscous or loss modulus (G′)[99]. The moduli are mapped for a range of strain rates by varying the sinusoidal oscillatory frequency. Investigations have found that the fibrin gels are primarily elastic at physiological shear rates and store deformation energy as quantified by the elastic modulus G′. The elastic modulus G′ (solid symbols) is greater than the viscous modulus G″ (open symbols) for frequencies < 1000 rad/s as shown in Figure 6.4[100]. It is important to note that the microfluidic resonant devices disclosed in this dissertation operate below this upper frequency upper-limit. In addition to being the dominant energy storage mode, the elastic modulus G′ is constant through the range of frequency or strain rates. This means the elasticity of clot does not change with different physiological and pathological conditions that result in changes of blood flow rate. The stress rate changes tremendously depending on whether the injury site is in the arterial or venous system. Therefore, the clot elasticity remains relatively constant as expected physiologically[101]. In addition to bulk rheological investigations, microrheology studies using optical tweezers have found that the fibrin fibers behave as flexible, cross-linked bundles of protofibrils[100]. This cross-linking has been attributed as the primary reason for fibril gels to retain the elasticity with varying shear rates[100].

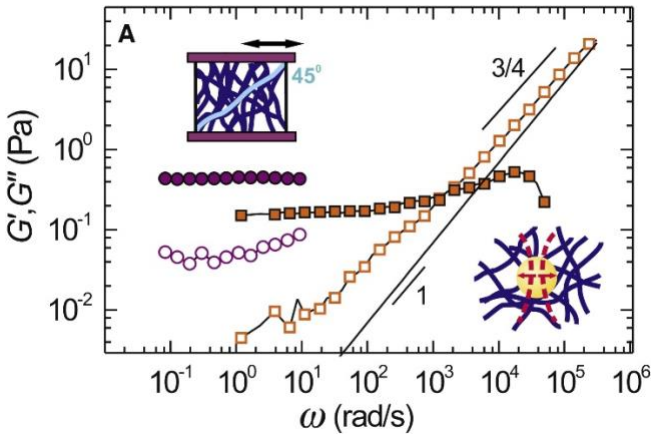

Figure 6.4. Frequency dependence of elastic modulus (solid symbols) and viscous modulus (open symbols) measured by rheometer (circles) and microrheology (squares). (adapted from [100])

6.2.2 **Cross-linking in fibrin gels**

Fibrin converted from fibrinogen can polymerize and finally form a three-dimensional network through covalent cross-linking. The elasticity and rigidity of networks formed by pure fibrinogen-fibrin gel (F-T) is very small as shown in Figure 6.5. On the other hand, in blood derivatives like platelet-free plasma (PFP) and platelet-rich plasma (PRP) covalent crosslinks are formed by the catalytic action of FXIII in plasma. The higher value of G' in plasma clots compared to that of F-T gel is due to the crosslinking. The values of G' is even higher for PRP clot because platelets get embedded in the growing fibrin gel and become the cross-linking regions[102]. The contractile protein, thrombosthenin, in the platelets exerts a contractile force on the fibrin network which reduces the size and increases the stiffness of the network over time, as evidenced by the decrease in elastic modulus for PRP sample in Figure 6.5. Thus, rheological investigations can provide insights into the molecular origins of the clot mechanical properties.

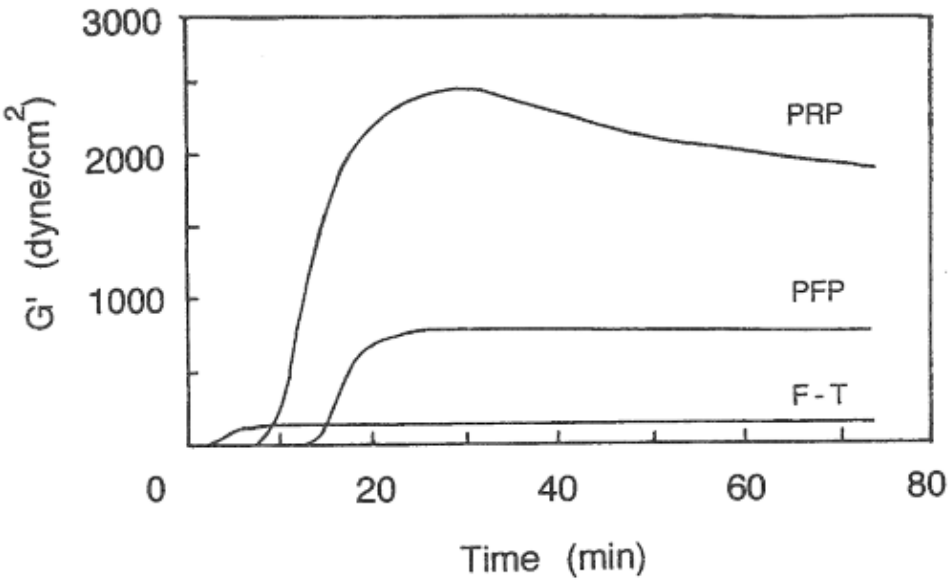

Figure 6.5. Change in elastic modulus (G′) during clotting of different blood derivatives (adapted from [97])

6.2.3 **FVIII efficacy assays**

The catalytic action of FXIII is the primary contributor towards the elastic modulus change in fibrin clots. As seen in Figure 6.1, the fibrin cross-linking enzyme, activated form of FXIII, is the last enzyme in the coagulation cascade. Any upstream deficiency or defect may hamper the activation of FXIII and result in low elastic modulus and mechanical strength of the fibrin clot. FVIII is one such coagulation factor that directly affects the activation of FXIII[54]. Inherited or acquired deficiency of FVIII causes hemophilia A (HA) or acquired hemophilia A (AHA), respectively. The consensus recommendation for treatment of AHA requires routine monitoring of FVIII activity when underdoing the expensive FVIII substitution therapy. Chromogenic immunoassays for FVIII activity are intensive and require specialized laboratory setups. In addition, these platelet-free immunoassays miss the significant contribution of platelets in fibrin cross-linking depicted in Figure 6.5[103], [104]. This results in over-prescription of an already expensive drug. Thus, cell-based coagulation tests, like TGT, or functional tests, like TEG, are recommended to determine the appropriate FVIII substitution dosage needed to recover the individual hemostatic effect [54].

The TGT for FVIII activity is performed using a PRP sample mixed with TF in a microwell plate. The reaction is started by adding a chromogenic substrate solution containing $CaCl_2$. The time course of the fluorescent signal is used to derive the time-to-peak and the total thrombin generation (the area under the curve). Total thrombin generation is reported as the endogenous thrombin potential (ETP). The protocol is detailed by Hemker *et al*[105]. TEG uses whole blood as the sample and report the rigidity of the clot as the maximum amplitude (MA). The area under the TEG curve (AUC) is calculated to compare with ETP metric from TGT. Figure 6.6 shows the results comparing TGT from PRP and TEG from whole blood for a 40-patient cohort suffering

from AHA and undergoing FVIII substitution therapy. While the authors do not provide a statistical measure of correlation, it is evident from the figure that the TGT and TEG are comparable in performance for FVIII activity monitoring. The key point is RBCs in whole blood do not confound FVIII activity measurement and therefore for simplicity purposes PRP may be an acceptable sample to perform the FVIII activity assay.

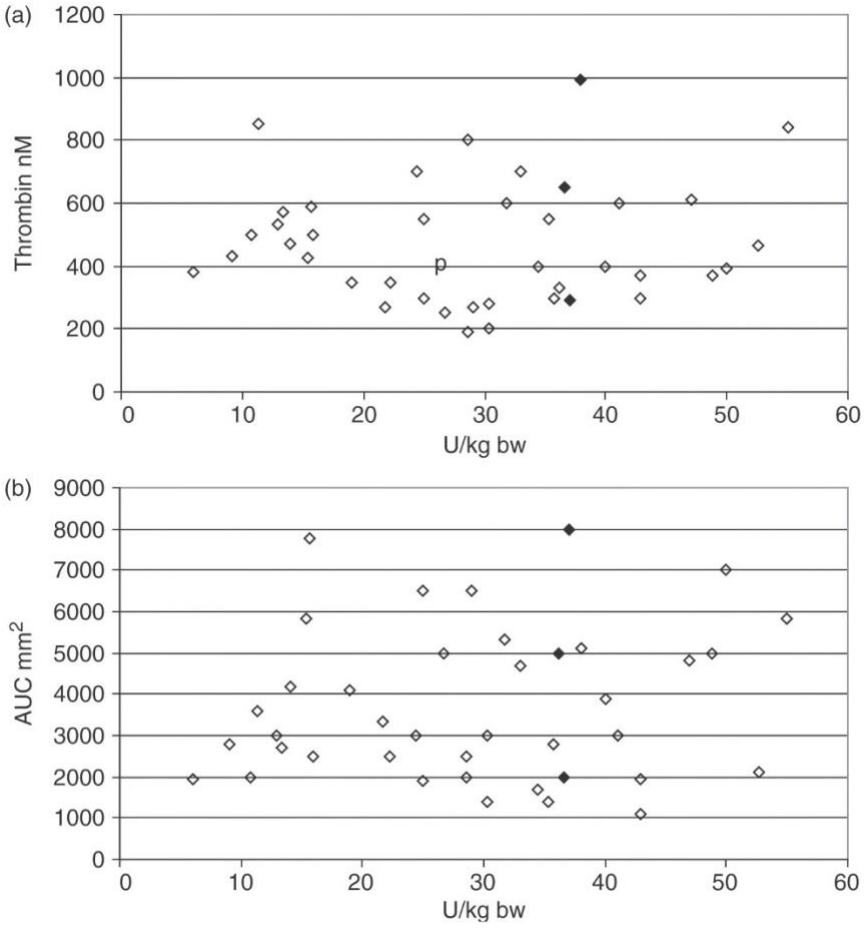

Figure 6.6. TGT and TEG measures for FVIII activity post-substitution therapy in a 40-patient cohort (adapted from [54])

Note: three patients received identical dosage of FVIII as indicated by the filled symbols.

The current clinical management of FVIII substitution therapy is primarily based on empirical data and clinical expertise. The dosage is determined by body weight, baseline FVIII activity

determined by the Coamatic FVIII assay and the clinical situation. The clinical relevance of aPTT and chromogenic assay is debated because of the absence of platelets. Additionally, the procoagulatory effect of platelets is highly individualized[103], [104], [106]. A few studies have provided evidence that even low FVIII activity levels (30%) are sufficient to restore hemostasis as assessed by TGT or TEG[54], [107], [108]. Despite the growing amount of evidence, Chromogenic assays continue to be used to measure FVIII activity. FVIII substitution is provided until the activity is restored to high levels as determined by the Coamatic FVIII assay which results in over-prescription of an already expensive drug. Therefore, a POC functional test for FVIII activity that accounts for individualized platelet activity could potentially saves millions of dollars in wasted medication.

6.3 COUPLING RHEOLOGICAL CHANGES TO MICROFLUIDICS

The resonance frequency of a series resonant microfluidic device was especially sensitive on to the diaphragm capacitor as discussed in Section 3.2.1. When a plasma clot forms over the diaphragm, it adds another elastic capacitor on series to the existing diaphragm capacitance. The net effect was an increase the resonance frequency by hundreds of Hz. This device design was utilized to perform a functional titration assay for FXIIIa activity.

6.3.1 **Proof-of-concept testing with pig plasma**

In this preliminary investigation, it was sought to measure the end-point shift in resonance frequency due to pig plasma clot formed on top of the diaphragm capacitor.

6.3.1.1 Device design

The schematic of the device used to measure the frequency shift with clotting is shown in Figure 6.7. Microfluidic device design with the sample cavity on top of the diaphragm capacitorFigure 6.7. The device is dimensionally similar to the device used for AC analysis of a series resonant device in the Section 4.1. Instead of the capacitor open to the air, in this case a 1mm cavity was laser-rastered over the capacitor (Figure 6.7 inset). Pig plasma mixed with the clotting activator (Neoplastine) was pipetted into the cavity. The elastic gel formed by the plasma on top of the capacitor acts as a series capacitor to the existing diaphragm capacitance. The reduced effective capacitance manifests as an increase in the resonance frequency.

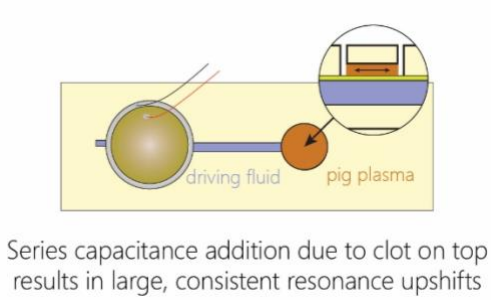

Figure 6.7. Microfluidic device design with the sample cavity on top of the diaphragm capacitor

6.3.1.2 Device operation

The device was filled with glycerol solution in the driving fluid layer before filling the sample cavity with plasma devoid of clotting ability. After the baseline resonant frequency was obtained using the diaphragm-lens sensor, the sample layer was emptied and refilled with the premix of plasma and Neoplastine. The resonant frequencies were obtained at 3 min, 15 min, and 30 min from the time the two fluids were mixed outside the device. Four runs were completed with each device. Three replicate devices were made.

6.3.1.3 Preliminary results and discussion

The resonance frequency measured using the diaphragm-lens vibration sensor shows a significant increase due to clotting, as shown in Figure 6.8. The unclotted measurement was made right after the pre-mix sample is introduced into the cavity over diaphragm. The clot measurement was made at t = 3 mins. Three devices were each tested for each depth of the cavity (d = 1.5 mm and 0.381 mm). N represents the number of repetitions of the same device. Statistically frequency shifts were noted in the device with the narrower cavity and requiring less sample (right pane). (preliminary data collection, courtesy of undergraduate mentee Doan Dinh)

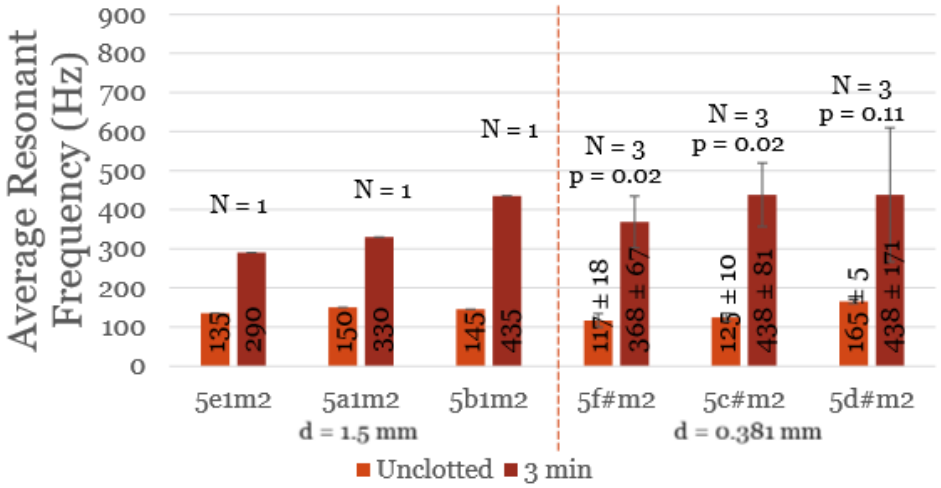

Figure 6.8. Resonance frequency shift due to plasma clotting in devices of two different cavity depths

Increased resonance frequency of this magnitude after clotting indicated a decrease in total capacitance. It was considered that the elastic clot may acts as an additional capacitance in series to the channel capacitor. The two capacitors must have connected in series to reduce the total capacitance of the system and resulted in an increase in resonance frequency. Since the elastic clot was formed in a cavity, which prevented any normal (in the same direction same as the diaphragm

capacitor) deformation of the clot, the lateral elongation of the disc must be contributing towards the increased elastic deformation of the capacitor-clot composite.

To test these hypotheses in a more controlled model, Fibrinogen-Thrombin (FT) system was used to form clots instead of Plasma clots. FT clots are often in study of Fibrin gel mechanics[109]. Compared to Plasma clots, FT clots take longer to develop through crosslinking. The extended time to gelation provided the opportunity to study the time dynamics of clotting through resonance frequency measurement. In addition, the crosslinking responsible for inducing elasticity to the clot can reduced through FXIIIa inhibitor. This provided an additional control knob to affect the elasticity and therefore the resonance response of the microfluidic resonant circuit.

6.3.2 **Fibrinogen-Thrombin gelation system**

6.3.2.1 Device design

Figure 6.9 shows the device used for testing the resonant response with FT gelation. The channel was 6 mm length, 1.5 mm depth, and 0.8 mm wide. The capacitor was 3.5 mm in radius and made of Rohaglas. The cavity on top of the capacitor was 3.75 mm in radius (r) and 0.381 mm (15 mil) in thickness (t). Inlets were defined as 0.8 mm holes on either side of the cavity. The electrical circuit model for this device represents a simple series resonant circuit as shown in Figure 6.9. The model predicted resonance frequency for this device was 650 Hz when filled with the glycerol solution (dynamic viscosity = 1.024 mPa·s[47], density = 1.05 g/mL) as the driving fluid. The FT clot adds an additional capacitance (C_{clot}) in series to the existing $C_{diaphragm}$. The total is reduced due to the series combination which would result in an increase in resonance frequency of the simple series resonant device.

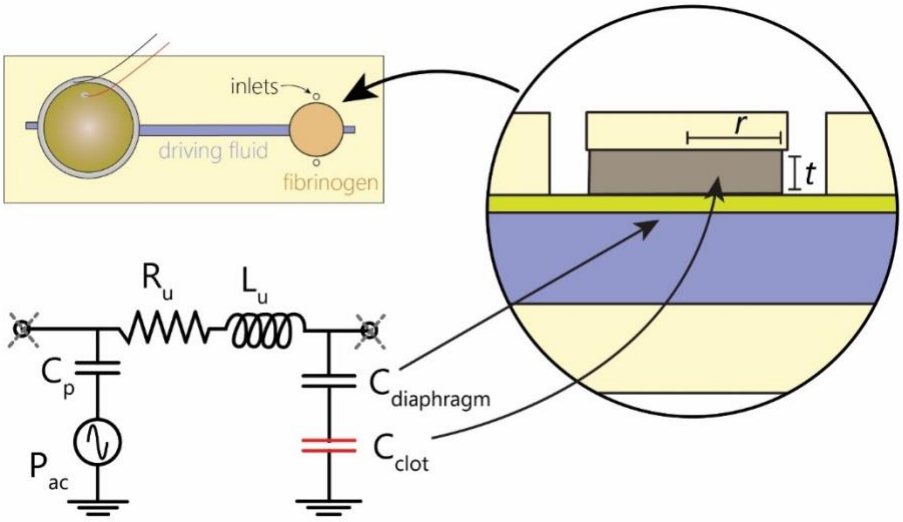

Figure 6.9. Microfluidic device and model used with FT gelation experiment

6.3.2.2 Clot expansion capacitance model

The clot formed on top of the capacitor can only expand lateral because the lateral expansion was prevented due to the cavity. This lateral mode of expansion of the elastic clot driven by the channel capacitor underneath is depicted in Figure 6.10. The right panel shows an example FT gelation in a petri dish.

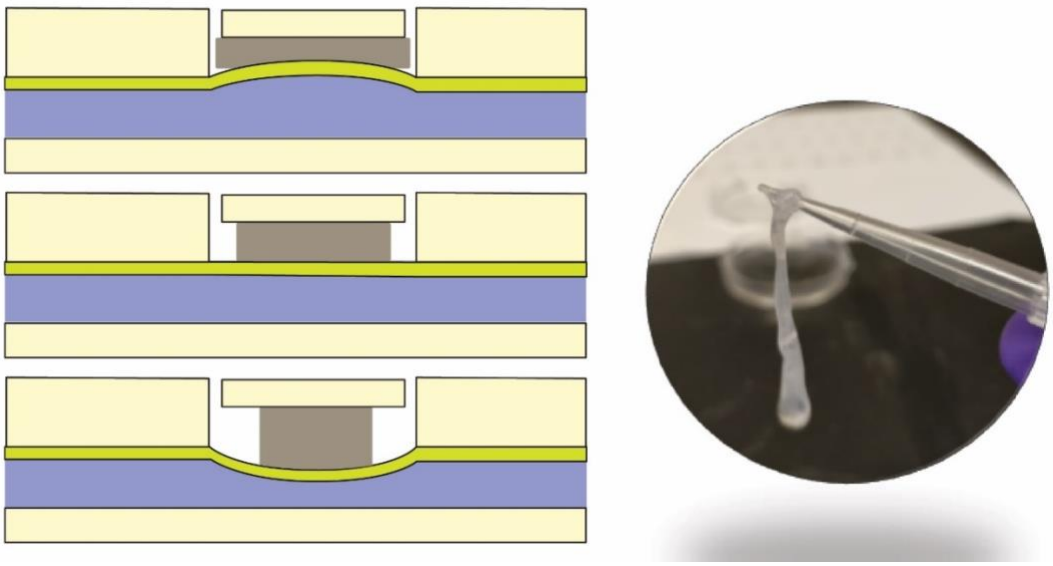

Figure 6.10. Lateral expansion of the clot adds to the total capacitance

An analytical expression for the capacitance (C_{clot}) due to the longitudinal expansion of the clot was estimated by evaluating:

$$C_{clot} = {\Delta V}/{\Delta P}\ , \text{(6.12)}$$

where ΔV is the volume change to a change in pressure ΔP. To estimate the volume change from lateral expansion of the FT clot, it was assumed that the diaphragm capacitor applied a constant force F. Therefore, the normal stress applied to the FT clot became:

$$\sigma_n = {F}/{A} = P. \text{(6.13)}$$

The elastic modulus relates the stress and strain in the normal direction as,

$$\varepsilon_n = {\sigma_n}/{E}\ . \text{(6.14)}$$

Now, since Poisson's ratio (ν) is the ratio of lateral to normal strain, the lateral strain was:

$$\varepsilon_{lat} = {\nu P}/{E}\ . \text{(6.15)}$$

Lateral deformation due to this strain was:

$$\Delta_r = \varepsilon_{lat} r\ . \text{(6.16)}$$

Under the assumption that the thickness is much larger than a change in radius Δ_r, the volume change due to lateral deformation became:

$$V = 2\pi r t \Delta_r\ . \text{(6.17)}$$

Substituting for Δ_r from Equation 6.16 provided an expression for the capacitance as:

$$C_{clot} = {\Delta V}/{\Delta P} = {2\pi r^2 t\nu}/{E}\ . \text{(6.18)}$$

The capacitance due to the clot was dependent on the dimensions of the clot as well as the Poisson's ratio and the elasticity of the clot. If the clot elasticity was decreased by preventing crosslinking through FXIIIa inhibition, the contribution of the clot in the total capacitance ($\propto 1/C_{clot}$) would

reduce thereby resulting in a smaller shift in resonance frequency compared to the uninhibited FT clot.

6.3.2.3 FT clot formation

FT clot formation protocol was adopted from the paper by Piechocka *et al*[109]. Human fibrinogen (part# F3879-250MG), α-thrombin (part# T9326-150UN) and Anti-coagulation FXIIIa inhibitor (part# SAB5500086-100UL) were obtained from Sigma-Aldrich (Milwaukee, WI). Fibrinogen solutions were made in a buffer of pH 7.4 containing 20 mM HEPES, 150 mM NaCl, and 5 mM $CaCl_2$. The protein concentration range was set to 4 mg/mL, which was the mid-range of the concentrations investigated in the work by Piechocka *et al*[109]. Polymerization and cross-linking was initiated by adding 0.5 U/mL thrombin. The networks were cross-linked by FXIIIa (present in the fibrinogen stock solution at a constant molar ratio of FXIIIa to fibrinogen). FXIIIa inhibitor was added to the fibrinogen aliquot before activating the clotting presence through thrombin addition.

6.3.2.4 Device operation

The activated Fibrinogen-Thrombin sample was immediately pipetted into the cavity using a 1 mL pipette. A sinusoidal actuation was applied to the device and the resonance frequency of the device was optically measured. Resonance frequency was recorded at five-minute intervals for the next hour. This end-point was chosen based on the observations made by Piechocka *et al*[109]. The device was placed in a 37° C incubator between measurements, which typically took 20-30 secs to perform. After the end of the experiment, the device was cleaned through ethanol and water washes and vacuum. The device was reused for next higher FXIIIa inhibitor concentration run. The driving fluid was emptied and refilled between runs.

6.3.2.5 Results and Discussion

Resonance frequency measurement over time for three identical devices (D1, D2, and D3) is plotted in Figure 6.11. Devices filled with fibrinogen solution were used for negative control (cornflower blue). Without the thrombin activation, clot was not formed and the resonance frequency remained unaffected. In the following run with the same devices, activated fibrinogen solution (without any FXIIIa) inhibitor was pipetted into the cavities. The resonance frequency response showed a significant and characteristic increase over time (denim). The curve resembles the characteristic shape of a TEG curve, which provides diagnostic information about clot initiation (kick-off), dynamics (slope), and maturity (saturation). This qualitative connection indicates that the same rick information may be present in this compact implementation. This demonstration marks a significant step in developing microfluidic technology to bring TEG and ROTEM measurement to point-of-care. It is important to note that clot retraction and lysis was not observed in these devices due to lack of platelets and fibrinolysis agents respectively.

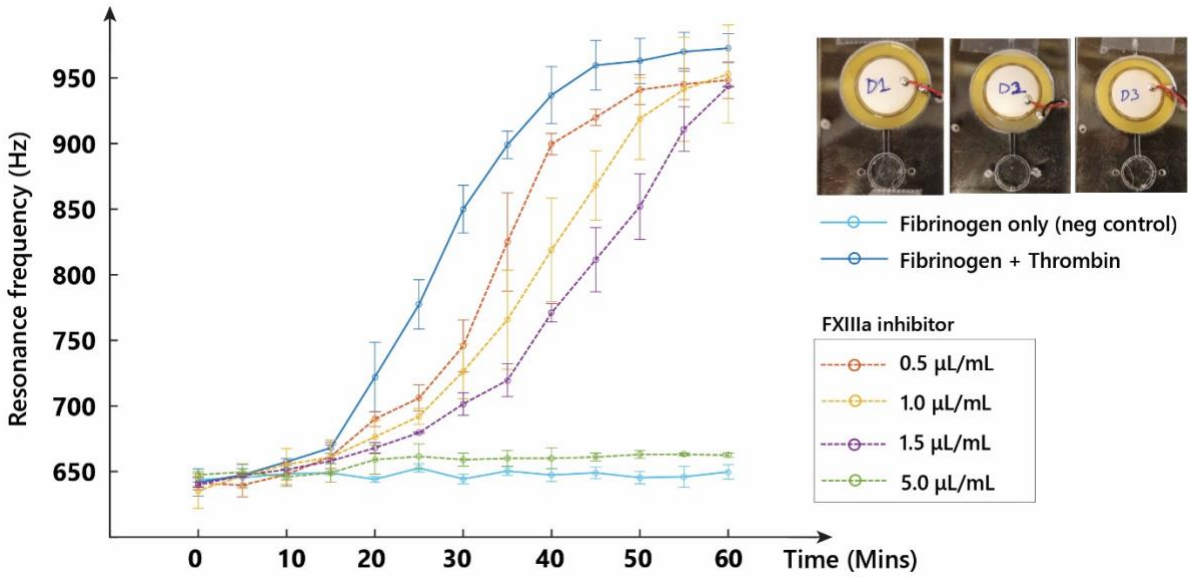

Figure 6.11. Resonance frequency shift with increasing FXIIIa inhibitor concentration

In the subsequent device runs, FXIIIa inhibitor was added to the fibrinogen solution prior to thrombin activation. The time development of resonance frequency (dotted curves) showed a trend towards decreased resonance frequency at any fixed time point (most apparent at t= 45 mins; paired t-test p-value < 0.07). The effect may be due to decreased FXIIIa activity in presence of the inhibitor. This hypothesis was tested by spiking in FXIIIa inhibitor at high concentration (5.0 µL/mL; Apple) in the fibrinogen solution. The resonant frequency remained changed suggesting that by preventing fibrin crosslinking, elastic changes in clotting were not observed.

The goal of this work was to introduce the concept of monitoring a biological process through changes in rheological properties of the sample. By coupling the elastic changes with clotting of plasma and fibrinogen-thrombin solution to the diaphragm capacitor, time development of clot formation (similar to TEG) can be measured in microfluidic devices. Moreover, the data is indicative that this clotting efficacy measurement is sensitive to potentially clinically-relevant levels of individual clotting factors and activators. More work is warranted to calibrate and validate the method using more complex sample types like platelet-rich plasma and whole blood.

6.4 OUTLOOK AND FUTURE WORK

This work marks the first demonstration of a TEG-like measurement in a microfluidic device. However, in order to completely characterize and calibrate this technique, side-by-side measurements with a TEG, ROTEM, or ReoRox are required. The design of the microfluidic device used in this work could potentially be optimized for resonance shift, driving fluid and sample volumes, and user steps involved. To maximize the frequency shift, in addition to the electrical circuit model investigation, research is needed to understand the solid-gel dynamics at play on top of the diaphragm capacitor. For someone seeking to further this work, the following

discussion could be considered a starting point because it lists preferred design choices planned and questions that could be readily answered through extensions of this work.

The clot expansion model shown in the Section 6.3.2.2 assumes that the clot and the diaphragm are identical sizes. It is possible that the capacitance equation may be missing a simple correction factor that accounts for area shared by the clot and diaphragm. This correction factor can be investigated by designing devices with differently sized clot and diaphragm capacitors and use this experimental data to fit the capacitance model equation with the overall area as a linear fitting parameter.

The vision to replace a lab-based TEG machine with a smartphone and plastic chip is depicted in shown in Figure 6.12. Audio-powered microfluidic technology is utilized to perform clotting efficacy measurement in a disposable plastic chip with pre-dried reagents and integrated heater. Such a plastic chip has onboard electronics to drive the piezo buzzer, controls the integrated heater (37° C) and process the photodiode sensor output. The new Texas Instruments DRV2700 chip with an integrated boost power supply (5V to 105V) is a possible transform-less power source for such a piezo driver. The datasheet suggests that the frequency response is flat down to 100 Hz, which should be acceptable for this application. An MSP430 microcontroller would be paired with this chip to provide the actuation control. An infrared LED is a prudent choice for the diaphragm-lens sensor as blood and blood derivatives are mostly transparent in the infrared spectrum. It is recommended that a photodiode array, like AMS TSL1401, be used instead of a single-pixel large active area diode to remove the need of perfect alignment in the integrated device.

While it would have been ideal if the device shown in Figure 6.9 did not require any additional steps beyond introducing the sample to the clotting cavity, it is likely that the bottom microfluidic channel may be filled by the user. Since the chemical properties of this driving fluid do not affect

the device response, tap water pipetted into the device through one of the inlet could suffice. Even this manual step could be prevented by pre-filling the device with the driving fluid. The possibility of pre-filling devices during mass manufacturing is a being actively researched[110].

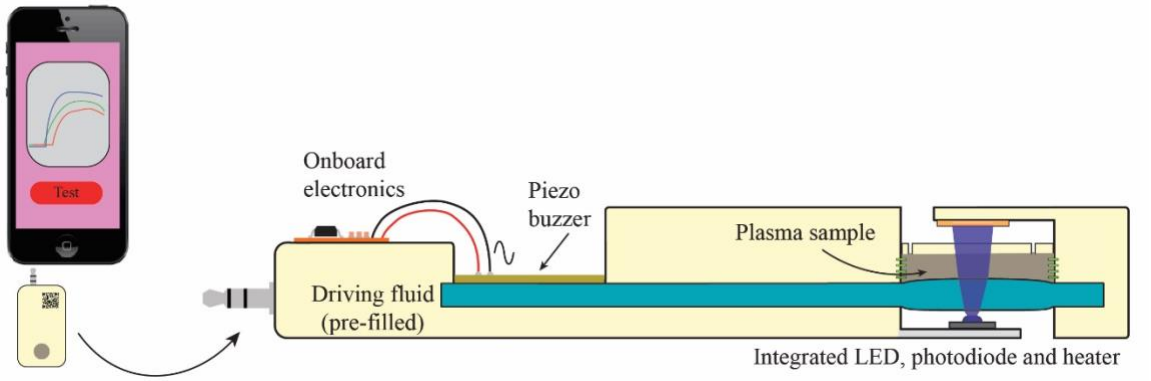

Figure 6.12. Vision of integrated microfluidic resonant device for FVIII activity monitoring

Chapter 7. CONCLUDING REMARKS

This dissertation work builds on the seminal work from the groups of Begley and Landers with the goal to extend the application and usability of the concept of 'frequency-tuning'[30-32]. The investigation began with addressing the shortcoming of the prior work. These were the requirement of off-chip components (pressure source, actuator tubes) and limited the operating frequency below the audio range (<100 Hz). Here, the off-chip pressure source was replaced by an integrated, bimorph piezo buzzer. The dangling actuator tubes that acted as inductance were removed and instead mm-sized channels were used to add inductance to the devices. Stiffer materials were investigated and tested for the diaphragm use. A laminated fabrication method was developed to assemble the devices with minimal variation between devices. The result was integrated microfluidic devices with resonant behavior in audio frequency range.

In order to understand the frequency behavior of flow magnitude and phase in microfluidic resonant circuits, an equivalent electrical circuit model was created. Using the classic electric-fluidic analogy, electrical counterparts of the microfluidic components were represented. The values of the some of the electrical components (R and L) in the equivalent model were frequency dependent and analytically calculated using the important work by Morris and Forster[36]. The remaining components (C_p, P_{ac}, C_c) were individually fitted to match the model prediction to the experimental response. The simple electrical model was found to be remarkably predictive of simple, as well as complex, multi-channel networks.

A significant focus of this dissertation work was on experimental characterization of the frequency response of the microfluidic resonant circuits. The goal was to improve the understanding of the nuances of the frequency response in order to engineer the resonant behavior. Two independent flow magnitude and phase measurement techniques were provided in this

dissertation work. The microscope-based bead tracking technique measured the flow magnitude and phase in channels. The general approach presented here can be extended to other microfluidic flow tracking applications. The capacitor flow measurement using the diaphragm-lens sensor was especially popular in academic conferences. This novel technique was developed as part of a graduate class and was simple to implement, robust, non-invasive (because it is optical), and amenable to integration into the final device. The two measurement techniques generated rich data which allowed for investigation of some of the complex flow behavior in these devices.

In addition to the providing accurate flow magnitude and phase data, the two measurement techniques enabled translation of a number of classic electrical characterization techniques to microfluidics. Frequency characterization using AC analysis, Fourier analysis, or Step analysis differed only in the choice of the input actuation signal, but the information provided varies widely by the characterization technique. The demonstration of these techniques showed that the classic electric-fluidic analogy extends beyond simple circuit elements to functional properties like linearity and homogeneity.

On the application front, the microfluidic resonant circuits were used to create frequency-controlled pumps. Pumping can be turned on/off by simply matching the actuation frequency to the resonance frequency of the underlying microfluidic circuit. Through the advanced flow characterization techniques developed in this work, it was identified that pumping is not just limited to series resonance, but can occur at the parallel resonance. Moreover, the pumping direction was switched at parallel resonance allowing for engineering the bi-directional, frequency-tuned pump operating in audio frequency range.

Beyond flow control, microfluidic resonant circuits were used to detect rheological changes with blood clotting. By physically coupling the clot to the existing diaphragm capacitor, elastic

changes with clotting were detected as shifts in resonance frequency. The fibrinogen-thrombin clot model used in this dissertation showed an increase in resonance frequency over time which matches the response from lab-based equipment for viscoelastic measurements of clotting. Additionally, by adding FXIIIa inhibitor to reduce crosslinking and elasticity, it was observed that the resonant response was affected in a meaningful way. This was an exciting development and may initiate a multitude of research avenues to take this work further.

In summary, the work presented here fits the broad research goal to enable novel applications of audio-responsive microfluidic circuits in lab-on-a-chip devices.

Chapter 8. SUPPLEMENTARY INFORMATION

8.1 COMPLETE BEAD POSITION FITTING RESULT FOR THE SERIES RESONANT DEVICE

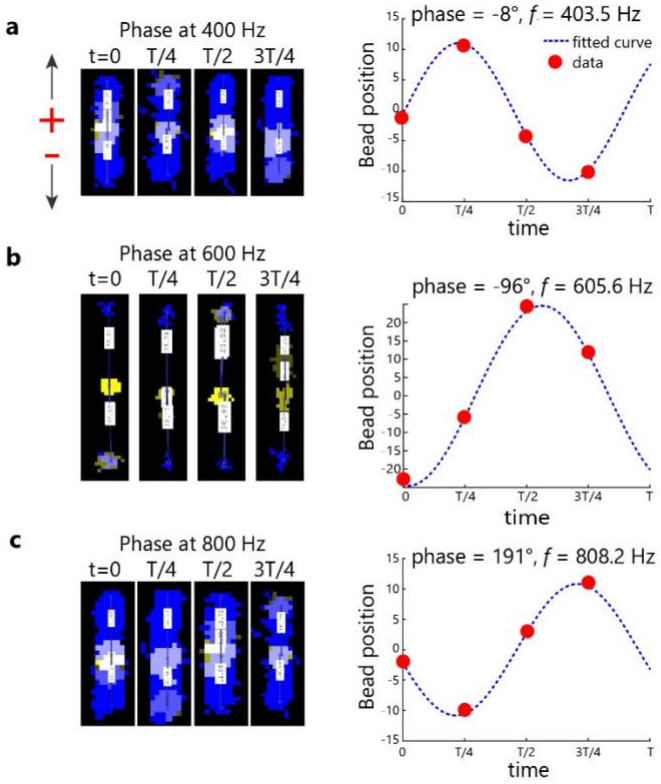

Figure 8.1. Phase calculation using bead position at the four offsets.

Figure 8.1 **Extended Caption**: **a.** Shows the bead traverse at 400 Hz. The bead position (red) relative to the 'rest' position (yellow) at the four offsets is plotted on the right. Positive and negative directions are indicated. Note that while it appears that at t=0 the bead was moving up (positive) - towards the top extreme, in the actual fit, the position was slightly negative because any drift in the center rest position across the four measurements was corrected. The dashed curve show the result of the sum of sines fit. The fitted phase and frequency of the fundamental frequency from sum of sines are shown. The fitted phase was adjusted (+90°) for the position-to-velocity conversion (see Section 8.2). The normalized magnitude of the harmonics were orders of magnitude (10^{-5}) smaller compared to the fundamental (*f*). **b.** and **c.** Show the bead positions and the fit for 600 Hz and 800 Hz respectively.

8.2 PHASE DIFFERENCE BETWEEN BEAD POSITION (X) AND VELOCITY (V)

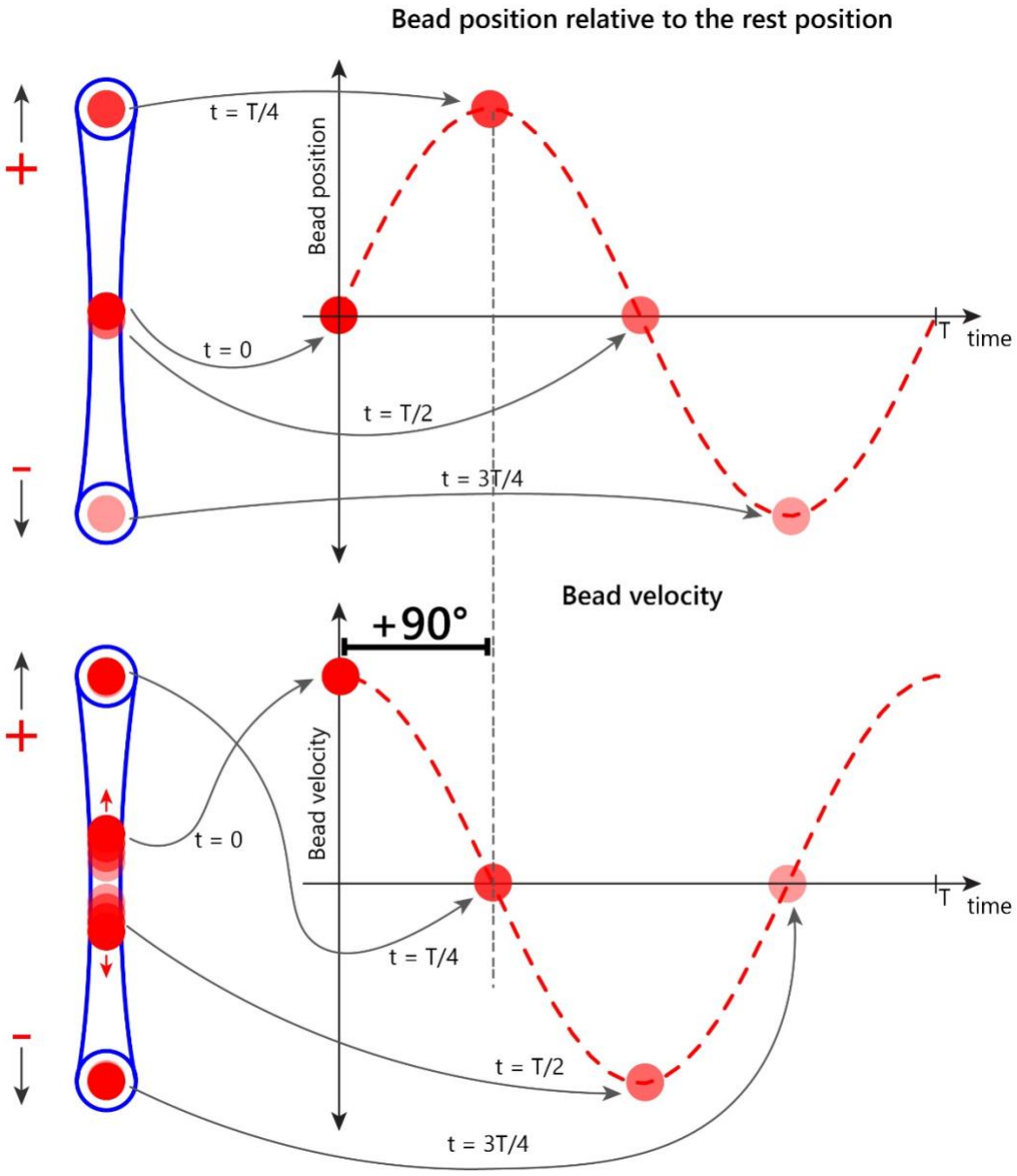

Figure 8.2. Phase difference between bead position (x) and velocity (v).

Figure 8.2 **Extended Caption**: Top panel shows bead position with respect to the center rest position at different time points. In this example, the bead starts from the center rest position (minimum position) and moves to the top extreme (maximum position) by T/4. By T/2, the bead is back to the center position but moving towards the bottom

extreme, which it reaches by 3T/4. The fitted curve for bead position reveals a sine wave with about 0° phase. The bottom panel shows the bead velocity for the same example. At t=0, when the bead is at the center rest position and moving to the top extreme, its velocity is maximum. When the bead reaches the extreme position, it comes to a stop, much like a pendulum. Hence its velocity is minimum. The plot of velocity versus time shows that the velocity (v) is shifted by $+90^{o}$ relative to bead position (x). Since the experiments here measured bead position, phase shift determined from bead position was shifted by $+90^{o}$ to allow direct comparison to phase shift of the AC flowrate provided as the output from the circult model.

8.3 VOLTAGE TO BEAD STREAKS CONVERSION FUNCTION

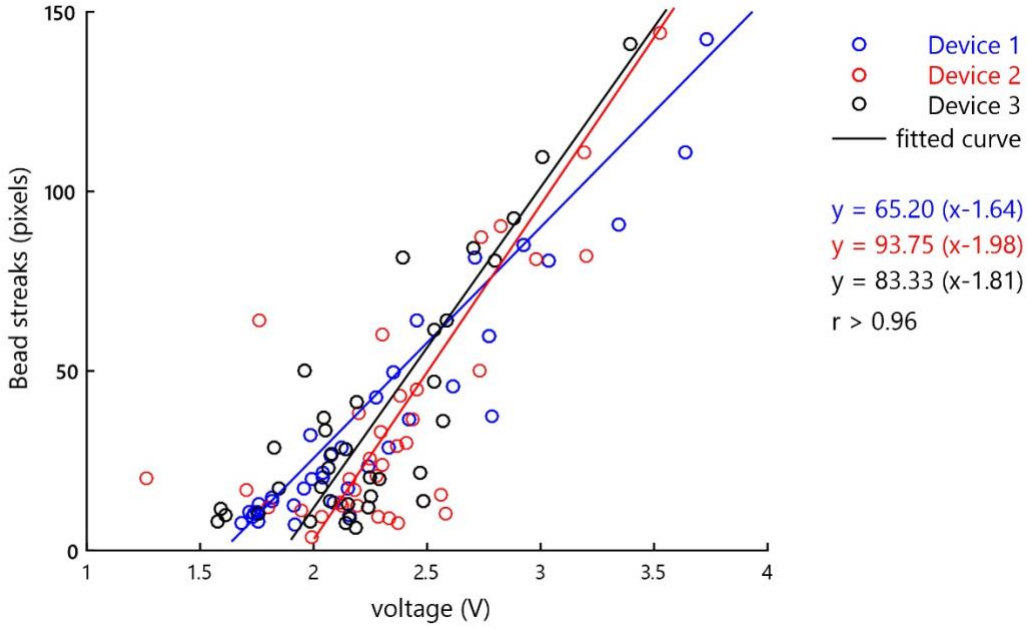

Figure 8.3. Voltage to bead streaks conversion function

Figure 8.3 **Extended Caption**: The linear function for converting sensor voltage to equivalent bead streak was calculated using a set of three calibration devices (series resonant device, f_s = 250 Hz, channel length = 16 mm, capacitor radius = 3.5 mm). Flow magnitude was measured using beads in the channel and through the capacitor. Since flowrate calculated by both methods should be equal in magnitude and phase, the bead streak length (pixels) measured using the images from the channel and the raw sensor voltage (V) from the diaphragm-lens sensor for the same frequency correlate linearly as shown in the plot. The fitted parameters (slope and intercept) from the three devices were averaged and the resulting function was used to convert future sensor measurements to equivalent bead streaks, which were used to calculate the flowrate using the same techniques as in the channel.

8.4 ANALYTICAL EXPRESSIONS FOR RESONANCE FREQUENCIES

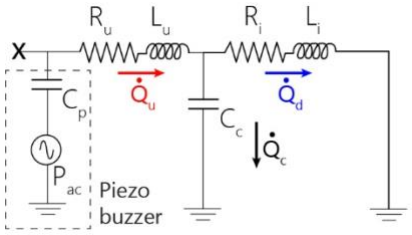

Figure 8.4. RLC circuit model for a generic microfluidic device with deformable features

Note: Arrows indicate positive flowrate magnitude (not to be confused with flowrate amplitude used in main text)

Referring to the circuit model in Figure 8.4, the impedance to the pressure source V_s as a function of excitation frequency can be calculated as series and parallel and combination of the channel and diaphragm impedances as

$$Z_{total} = \frac{1}{j\omega C_p} + (R_u + j\omega L_u) + \frac{\frac{1}{j\omega C_c}(R_d + j\omega L_d)}{\frac{1}{j\omega C_c} + (R_d + j\omega L_d)}$$

Separating Z_{total} into real and imaginary parts:

$$Z_{total}|_{Real} = R_u + \frac{R_d}{(C_c L_d \omega^2 - 1)^2 + C_c^2 R_d^2 \omega^2}$$

$$Z_{total}|_{Imag} = \omega L_u - \frac{1}{\omega C_p} + \frac{\omega(L_d - C_c R_d^2) - C_c L_d^2 \omega^3}{(C_c L_d \omega^2 - 1)^2 + C_c^2 R_d^2 \omega^2}$$

Now, at resonance frequency, $Z_{total}|_{Imag}$ is minimum. Before differentiating the expression, it must be noted that:

- $Z_{total}|_{Imag}$ is independent of R_u. Therefore, it was expected that the resonance frequencies will be independent of upstream resistant R_u.

- C_p only appears in the $Z_{total}|_{Imag}$ expression and as an independent term with no interactions suggesting that it may not play an important role in determining resonance frequency points.

At this point, the parallel resonance frequency can be estimated by seeking the expression for $Z_{total}|_{Real}$. At parallel resonance, the real part of the impedance is maximum. This requires the denominator in the expression for $Z_{total}|_{Real}$ to be minimum. Thus, the squared term in the denominator, $(C_c L_d \omega^2 - 1)^2$, should be equal to zero.

$$C_c L_d \omega_p^2 - 1 = 0$$

$$2\pi f_p = \omega_p = \frac{1}{\sqrt{L_d C_c}}$$

which is same as expression provided in the previous section.

Solving $Z_{total}|_{Imag} = 0$ using the symbolic math toolbox in MATLAB yielded three distinct roots. These are the resonance frequency points – f_o, f_p and f_s – shown in the sample AC flowrate frequency response in Figure 3.3. The expressions are too complex and long to include here.

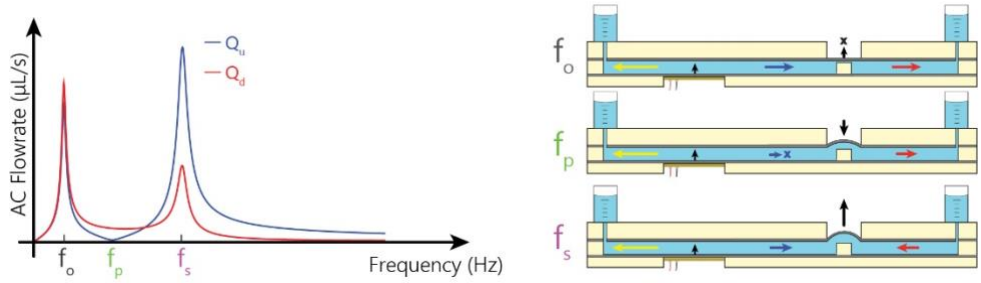

Figure 8.5. AC flowrate frequency response shows the three distinct resonance points

The expressions can be reduced for improved understanding using simple approximation. Since $C_p >> C_c$, the effect of the former can be ignored in the frequency range of operation. Not surprisingly, the expression for $Z_{total}|_{Imag} = 0$ reduces to provide only two frequency points – f_p

and f_s – further justifying the rationale that the piezo diaphragm capacitance does not affect the parallel and series resonance of the microfluidic network.

Under $C_p >> C_c$ the solution to $Z_{total}|_{Imag} = 0$ becomes

$$\omega = \sqrt{\frac{\pm(C_c L_u R_d^2 - L_d^2) + L_u^2 + 2L_u L_d - C_c L_u R_d^2}{2L_u L_d^2 C_c}}$$

'+' sign gives the same expression for $\omega = \omega_p$

$$2\pi f_p = \omega_p = \frac{1}{\sqrt{L_d C_c}}$$

'-' sign gives expression for ω_s

$$2\pi f_s = \omega_s = \sqrt{\frac{-C_c L_u R_d^2 + L_u^2 + L_u L_d}{C_c L_u L_d^2}}$$

Note that the expression for series resonance frequency ω_s is independent of R_u. An analysis like in previous section for series resonance frequency is difficult due to the complex nature of the ω_s expression.

At low frequencies, the diode diaphragm impedance is small ($\frac{1}{\omega C_c} \sim 0$). This is set to zero in the expression for $Z_{total}|_{Imag}$ to get the imaginary part of total impedance at low frequencies -

$$Z_{total}|_{Imag,\ low\ freq} = \omega L_u - \frac{1}{\omega C_p} + \omega L_d$$

Solving for $Z_{total}|_{Imag,\ low\ freq} = 0$ yields a single solution

$$2\pi f_o = \omega_o = \frac{1}{\sqrt{(L_u + L_d) C_p}}$$

which is expected. The resonance frequency f_o depends only on the series sum of channel inductances and the piezo diaphragm capacitance. f_o is primarily decided by C_p as it is orders of magnitude larger than the total inductance of the system. In practice, f_o was observed around 60 Hz across all the devices.

8.5 ESTIMATION OF CAPACITANCE DUE TO A WEIR PLACED UNDERNEATH

A device (BVD3, Figure 8.6 (a) top) was created identically to the Device 2 (backward flow) from the main text (Section 5.6.1), except that there was no weir under the capacitor diode. The device operation was same as described in the main text. Both inlets were left open to air. AC flowrate images were obtained about the center of the upstream channel for a range of frequencies. The images were programmatically analyzed to estimate the upstream AC flowrate frequency response (Figure 8.6 b) as described in Section 4.1.3.1.

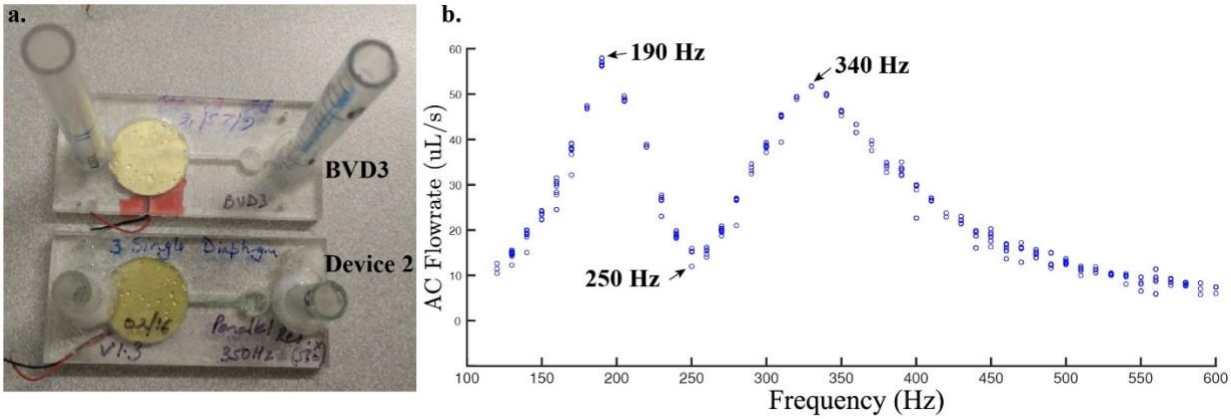

Figure 8.6. Estimation of capacitance with a weir underneath

Figure 8.6 **Extended Caption: a.** Backward pumping device from main text (Device 2, bottom) and an identical device (BVD3, top) without the weir. **b.** Upstream (channel connecting the piezo and the diode capacitor) AC flowrate frequency response shows f_o = 190 Hz, f_p = 250 Hz and f_s = 340 Hz.

Compared to Device 2 (f_o = 200 Hz, f_p = 340 Hz and f_s = 510 Hz), the parallel and series resonance frequencies for the weir-less device were lower (f_o = 190 Hz, f_p = 250 Hz and f_s = 340 Hz. The weir may impede the bimorph flexing of the diaphragm, thereby reducing the diode capacitance in half (*i.e.*, $C_{c,\text{ no weir}} = 1/2 * C_{c,\text{ weir}}$). The increase in capacitance results in lowering of the resonance frequencies (f_p and f_s). Since f_o does not depend on the capacitor diode (C_c), it remained roughly

the same between the two devices. Using the resonance frequency expressions provided in the previous section, the change in f_p and f_s due to change in diode capacitor C_c was estimated:

Model predicted ratio of parallel resonance f_p: $$\frac{f_{p,\ Device\,2}}{f_{p,\ BVD3}} = \frac{\frac{1}{2\pi}\sqrt{\frac{1}{L_d \frac{C_c}{2}}}}{\frac{1}{2\pi}\sqrt{\frac{1}{L_d C_C}}} = \sqrt{2} = \mathbf{1.41}$$

Observed shift in f_p is comparable: $$\frac{f_{p,\ Device\,2}}{f_{p,\ BVD3}} = \frac{340\ Hz}{250\ Hz} = \mathbf{1.36}$$

Model-predicted ratio of series resonance f_s: $$\frac{f_{s,\ Device\,2}}{f_{s,\ BVD3}} = \frac{\frac{1}{2\pi}\sqrt{\frac{-\frac{C_c}{2} L_u R_d^2 + L_u^2 + L_u L_d}{\frac{C_c}{2} L_u L_d^2}}}{\frac{1}{2\pi}\sqrt{\frac{-C_c L_u R_d^2 + L_u^2 + L_u L_d}{C_c L_u L_d^2}}}$$

Generally, $-C_c L_u R_d^2 \ll L_u^2 + L_u L_d$, thus $\frac{f_{s,\ Device\,2}}{f_{s,\ BVD3}} = \sqrt{2 \times \frac{(L_u^2 + L_u L_d)}{(L_u^2 + L_u L_d)}} = \sqrt{2} = \mathbf{1.41}$

Observed shift in f_s is also comparable: $$\frac{f_{s,\ Device\,2}}{f_{s,\ BVD3}} = \frac{510\ Hz}{340\ Hz} = \mathbf{1.50}$$

Thus, the decrease in resonance frequencies (f_p and f_s) can be attributed to the absence of the weir.

8.6 EFFECT OF FLUIDIC PORT ON FREQUENCY RESPONSE OF MICROFLUIDIC RESONANT CIRCUIT

Two simple series resonant devices were fabricated – one with the inlet and one without. In the bottom device in Figure 8.7 a (BVD2), a fluid port similar to the devices in the dissertation was added. The left inlet was plugged for the BVD1 device using Scotch® tape. AC flowrate frequency response (Figure 8.7 b) was obtained as described in Section 4.1.3.1.

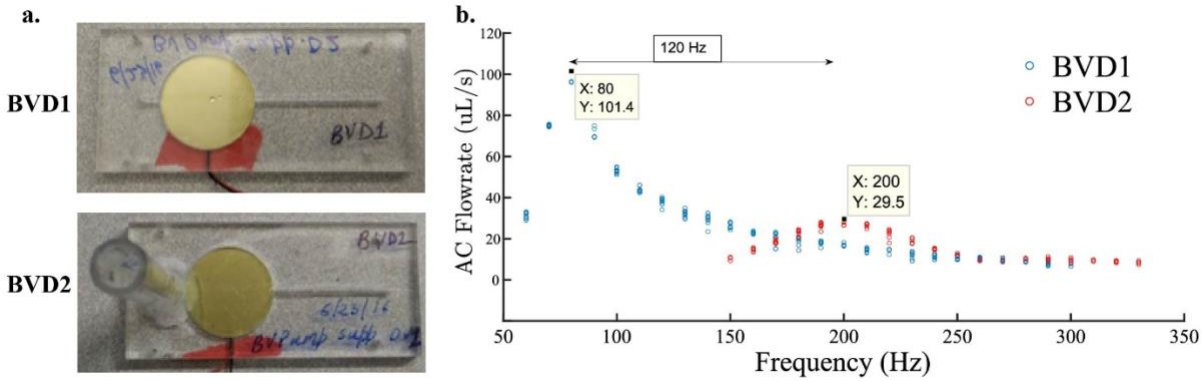

Figure 8.7. Comparison of frequency response from devices with and without fluidic port added

Figure 8.7 **Extended Caption a.** BVD1 and BVD2 were identical devices except that BVD2 had a port added to the left. **b.** The AC flowrate frequency response shows f_o series resonance frequencies of 80 Hz and 200 Hz for the BVD1 and BVD2 devices, respectively. Note the reduced magnitude at resonance for the BVD2 device due to the parallel port channel. Upstream channel length: 26.5 mm (model predicted average L = 30.5 μH, R = 0.2 mΩ), inlet channel length: 4.1 mm (L = 4.71 μH, R = 0.1 mΩ) and capacitor radius: 10 mm radius (C_p = 0.132 F). Note: 1 H = kg/mm^4, 1Ω = kPa-s/mm^3 and 1 F = mm^3/kPa.

Calculations: Validating model prediction with BVD1

$$f_{o\,BVD1}\,(\text{model}) = {}^{1}\!/_{2\pi\sqrt{L_u C_p}} = {}^{1}\!/_{2\pi\sqrt{30.5\mu \times 0.132}} = 79.3\ \text{Hz}$$

$$f_{o\,BVD1}\,(\text{observed}) = 80\ \text{Hz}$$

Calculating the unknown port inductance (L_p) by equating model prediction to the observed f_o for BVD2

$f_{o\ BVD2}$ (model) $= {1}/{2\pi\sqrt{L_{eff}C_p}}$ where $L_{eff} = \frac{L_u(L_i+L_p)}{L_u+L_i+L_p}$

Since the upstream channel is much longer ($L_u \gg L_i + L_p$)

$L_{eff} \sim L_i + L_p$

Now, $f_{o\ BVD2}$ (observed) $= 200$ Hz $= {1}/{2\pi\sqrt{L_{eff}C_p}}$

$L_{eff} = 4.79\ \mu$H $= L_i + L_p = 4.71 + L_{p,}$, therefore $L_p = 0.08\mu$H

The port inductance is small compared to other channels in the device (0.08 µH vs 4.71 µH and 30.5 µH). Therefore, the effect of the port on the resonance frequencies of device is small and can be ignored.

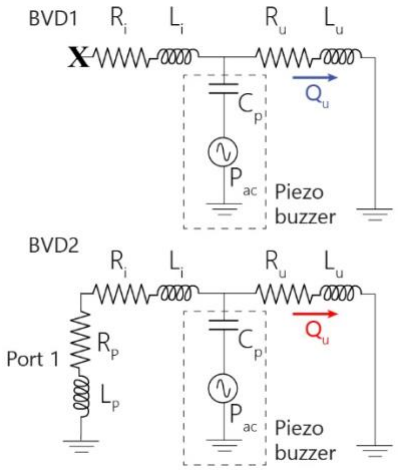

Note, L_s and R_s from the main text are made up of the inlet channel impedances (subscript i) and the port impedances (subscript p).

Figure 8.8. Electrical circuit model for the BVD1 and BVD2 devices.

8.7 AC FLOWRATE AMPLITUDE AND PHASE RESPONSE AT PARALLEL RESONANCE

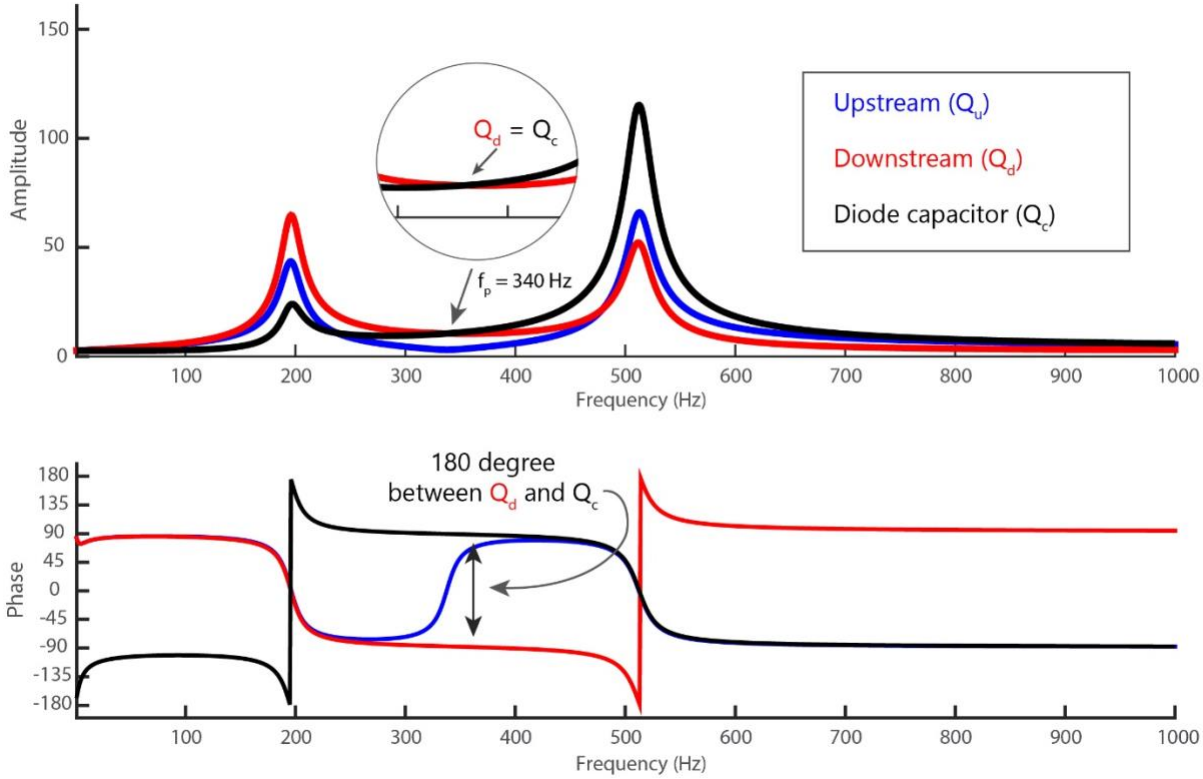

Figure 8.9. Model-predicted AC flowrate amplitude and phase frequency response for directional pump devices in Section 5.6.1 (Device 2)

Note: At f_p = 340 Hz, AC flowrate in the downstream channel and the diode-capacitor are equal in magnitude (top, inset) and opposite in phase (180-degree difference in phase, bottom plot).

8.8 AC FLOW IMAGES AT NON-PUMPING FREQUENCIES

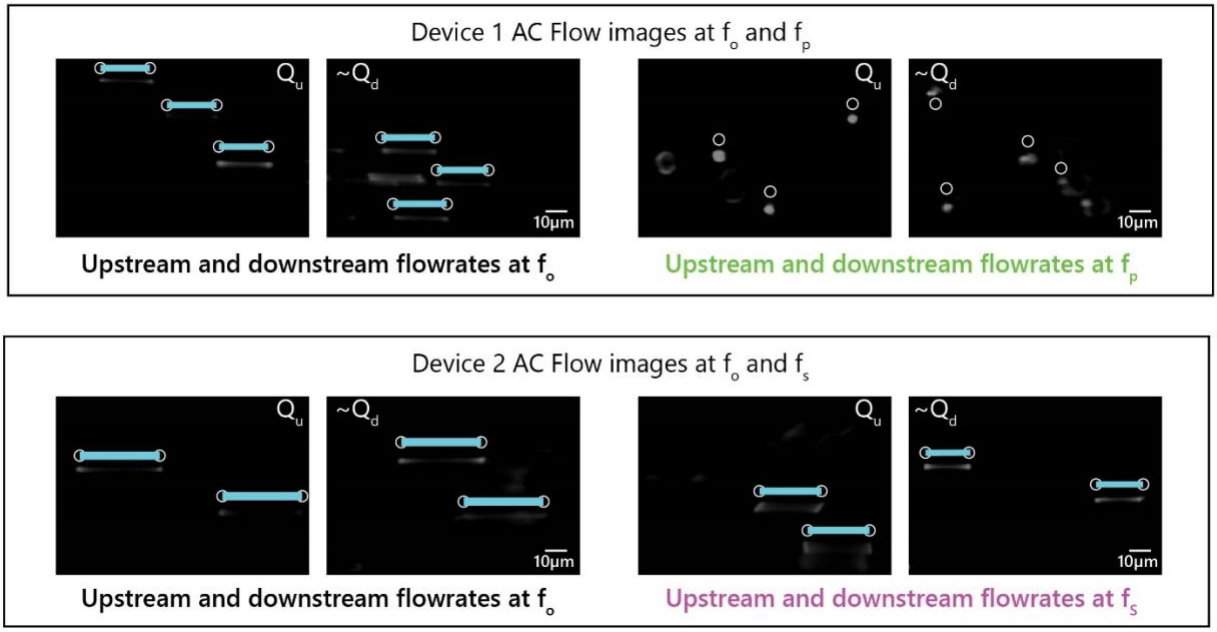

Figure 8.10. AC flow images at f_o and f_p for Device 1 showing comparable flow upstream and downstream

Figure 8.10 **Extended Caption** AC Flowrate images show comparable flow in the upstream and downstream channels at non-pumping resonance frequencies. In Device 1, the model predicted significant and comparable Q_u and Q_d at f_o and the same was observed (similar length of bead streaks, top left). Stationary beads indicate no flow at f_p in both the channels ($Q_u \sim Q_d \sim 0$), as expected (top right). Similarly, as per the model, in Device 2 comparable flow was observed at f_o (bottom left) and f_s (bottom right) in both the channels as indicated by similar length bead streaks.

8.9 DC PUMP PRESSURE FREQUENCY RESPONSE FOR DIRECTIONAL PUMP DEVICES

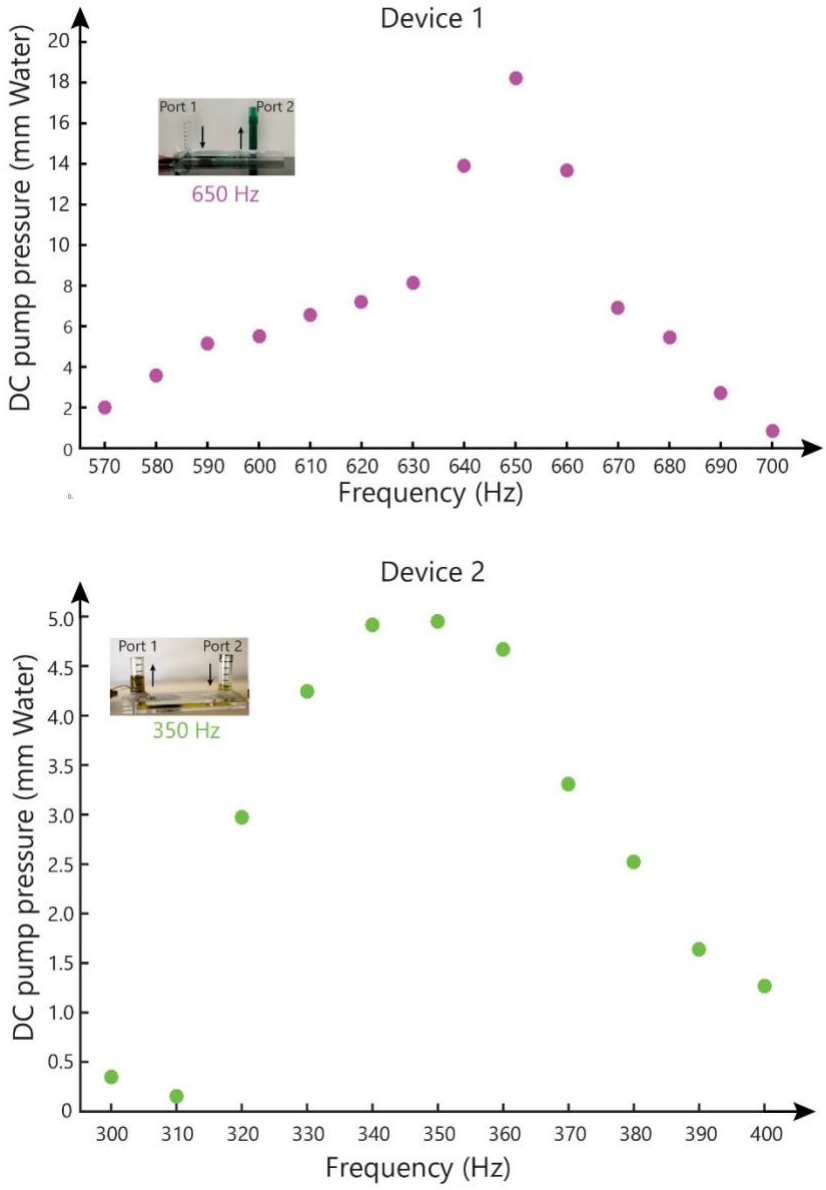

Figure 8.11. DC Pump pressure frequency responses for directional pump devices in Section 5.6.1

Figure 8.11 **Extended Caption** DC Pump pressure frequency responses for Device 1 and Device 2 show the same peak frequencies as the DC flowrate response included in the main text. The peak DC flowrate and DC pump

pressure may be inversely related. Device 2 had lower DC pump pressure (18.44 mm H_20 vs 4.9 mm H_20), but higher DC flowrate compared to Device 1 (2.5 μL/s vs 4.2 μL/s). Understanding the relationship between the DC pump pressure and DC flowrate may be imperative to designing more efficient direction control frequency-tuned pumps.

8.10 FORWARD PUMPING WAS NOT POSSIBLE AT PARALLEL RESONANCE

This section provides the mathematical framework showing that at parallel resonance $\dot{Q}_u < \dot{Q}_d$ for devices that can be fabricated using the methods described in the main text.

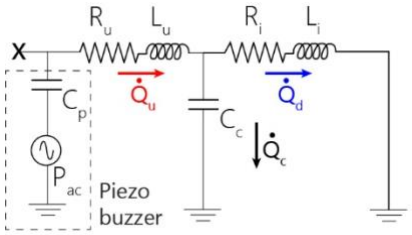

Figure 8.12. RLC circuit model for a generic microfluidic device with deformable features

Aim: To show $\left|\frac{\dot{Q}_u}{\dot{Q}_d}\right| < 1$ at f_p for all practical device designs

Note: Effect of diode in the circuit response is ignored for simplicity of calculation. $\dot{Q}$ is flowrate magnitude (not to be confused as amplitude, Q, used in main text)

Using mesh analysis, voltage loop equations for the downstream channel and the diode valve became:

$$\dot{Q}_d(R_d + j\omega L_d) - \dot{Q}_c \Big/ j\omega C_c = 0$$

and current conservation gives us $\dot{Q}_u = \dot{Q}_d + \dot{Q}_c$

Eliminating $\dot{Q}_c$ and rearranging gives

$$\frac{\dot{Q}_u}{\dot{Q}_d} = 1 + (R_d + j\omega L_d) j\omega C_c$$

which is complex quantity. The magnitude of the ratio is given as

$$\left|\frac{\dot{Q}_u}{\dot{Q}_d}\right|^2 = (1 - \omega^2 L_d C_c)^2 + (\omega C_c R_d)^2$$

Now, using the expression for parallel resonance frequency (derived in previous section):

$$\omega_p = \frac{1}{\sqrt{L_d C_c}}$$

Substituting $\omega = \omega_p$ in the expression for ratio of upstream and downstream flowrate magnitude squared gives

$$\left|\frac{\dot{Q}_u}{\dot{Q}_d}\right|_{\omega_p}^2 = (1 - \frac{1}{L_d C_c} L_d C_c)^2 + (\frac{1}{\sqrt{L_d C_c}} C_c R_d)^2$$

$$\left|\frac{\dot{Q}_u}{\dot{Q}_d}\right|_{\omega_p} = R_d \sqrt{\frac{C_c}{L_d}}$$

Since the goal is to understand the relationships between the device dimensions and the frequency response, simplified expressions for R_d and L_d [36] can be used to assess the expression further. Now,

$$R_d = \frac{12\mu l}{w^2 d^2}$$

$$L_d = \frac{\rho l}{wd}$$

Also,

$$2\pi f_p = \omega_p = \frac{1}{\sqrt{L_d C_c}}$$

where l, w, and d are the length, width and depth of a channel. Fluid dynamic viscosity and density are μ and ρ. Substituting these expressions in the expression for upstream and downstream flowrate ratio at parallel resonance:

$$\left|\frac{\dot{Q}_u}{\dot{Q}_d}\right|_{\omega_p} = \frac{2.1}{f_p A} < 1$$

where A= w*d was the cross-sectional area of the channel.

It is important to note that the flowrate ratio is inversely proportional to the cross-sectional area of the channel and the parallel resonance frequency. In this dissertation work, the aim goal was device operation in audio frequency range (>100Hz) because the broader goal of our research is to control microfluidic devices using audio tones generated on a cellphone (>100 Hz).

For $f_{p,min}$ = 100Hz, the expression reduces to

$$\frac{2.1}{100.A} < 1$$

Or

$$A > 0.021 mm^2$$

For a square channel, it is $w_{min} = d_{min} > 0.14\ mm$

This implies if channels wider and deeper than 0.14 mm are used, the upstream flow will always be less than downstream flow at parallel resonance frequency. The minimum channel width that could be reliably fabricated using our CO_2 laser cutter (Universal laser systems VLS 3.60) is about 0.8 mm. Hence, the upstream flowrate will always be smaller than the downstream flowrate at parallel resonance frequency for all practical devices using the described fabrication methods.

Example: For the range of device geometries and diaphragm material and operation in the 100-2000 Hz frequency range, the model-predicted magnitude order for $R_d \sim 10^{-3}$ kPa-s/mm^3, $C_c \sim 10^{-3}$-10^{-2} mm^3/kPa and $L_d \sim 10^{-5}$ Kg/mm^4.

For these typical values, $\left|\frac{\dot{Q}_u}{\dot{Q}_d}\right|_{\omega_p} \sim 10^{-3}\sqrt{\frac{10^{-2}}{10^{-5}}} = 10^{-1.5} \ll 1$

BIOBLIOGRAPHY

[1] Ericsson, “Ericsson mobility report,” 2015.

[2] T. Bocklet, E. Nöth, G. Stemmer, H. Ruzickova, and J. Rusz, “Detection of persons with Parkinson’s disease by acoustic, vocal, and prosodic analysis,” *IEEE Work. Autom. Speech Recognit. Underst.*, pp. 478–483, 2011.

[3] G. Martinez, A., Phillips, S., Carrilho, E., Thomas, S., Sindi, H., and Whitesides, “Simple telemedicine for developing regions: camera phones and paper-based microfluidic devices for real-time, off-site diagnosis,” *Anal. Chem.*, vol. 80, no. 10, pp. 3699–3707, 2008.

[4] J. Daneault and B. Carignan, “Using a smart phone as a standalone platform for detection and monitoring of pathological tremors,” *Front. Hum. Neurosci.*, vol. 6, p. 357, 2012.

[5] D. Breslauer, R. Maamari, and N. Switz, “Mobile phone based clinical microscopy for global health applications,” *PLoS One*, vol. 4, no. 7, p. e6320, 2009.

[6] H. Zhu, S. Isikman, and O. Mudanyali, “Optical imaging techniques for point-of-care diagnostics,” *Lab Chip*, vol. 13, no. 1, pp. 51–67, 2013.

[7] S. Wang, X. Zhao, I. Khimji, and R. Akbas, “Integration of cell phone imaging with microchip ELISA to detect ovarian cancer HE4 biomarker in urine at the point-of-care,” *Lab Chip*, vol. 11, no. 20, pp. 3411–3418, 2011.

[8] K. Yang, H. Peretz-Soroka, Y. Liu, and F. Lin, “Novel developments in mobile sensing based on the integration of microfluidic devices and smartphones,” *Lab Chip*, vol. 16, pp. 943–958, 2016.

[9] J. R. Buser *et al.*, “Electromechanical cell lysis using a portable audio device: enabling

challenging sample preparation at the point-of-care," *Lab Chip*, vol. 15, no. 9, pp. 1994–1997, Apr. 2015.

[10] T. Laksanasopin *et al.*, "A smartphone dongle for diagnosis of infectious diseases at the point of care," *Sci. Transl. Med.*, vol. 7, no. 273, p. 273re1, Feb. 2015.

[11] S. Mcinerney, "Can You Diagnose Me Now? A Proposal to Modify the FDA' s Regulation of Smartphone Mobile Health Applications with a Pre-Market Notification and Application Database Program Recommended Citation," *Mich. J. L. Reform*, vol. 48, no. 1073, 2015.

[12] K. Patrick, W. G. Griswold, F. Raab, and S. S. Intille, "Health and the mobile phone.," *Am. J. Prev. Med.*, vol. 35, no. 2, pp. 177–81, Aug. 2008.

[13] H. Wang and J. Liu, "Mobile Phone Based Health Care Technology," *Recent Pat. Biomed. Eng.*, vol. 2, no. 1, pp. 15–21, 2009.

[14] Q.-M. Xie and J. Liu, "Mobile Phone Based Biomedical Imaging Technology: A Newly Emerging Area," *Recent Patents Biomed. Eng.*, vol. 3, no. 1, pp. 41–53, Jan. 2010.

[15] A. Ozcan, "Mobile phones democratize and cultivate next-generation imaging, diagnostics and measurement tools.," *Lab Chip*, vol. 14, no. 17, pp. 3187–94, Sep. 2014.

[16] T. Laksanasopin *et al.*, "A smartphone dongle for diagnosis of infectious diseases at the point of care.," *Sci. Transl. Med.*, vol. 7, no. 273, p. 273re1, Feb. 2015.

[17] X. Xu *et al.*, "Advances in Smartphone-Based Point-of-Care Diagnostics," *Proc. IEEE*, vol. 103, no. 2, pp. 236–247, Feb. 2015.

[18] A. Pal, A. Visvanathan, A. D. Choudhury, and A. Sinha, "Improved heart rate detection using smart phone," in *Proceedings of the 29th Annual ACM Symposium on Applied Computing - SAC '14*, 2014, pp. 8–13.

[19] E. C. Larson, M. Goel, G. Boriello, S. Heltshe, M. Rosenfeld, and S. N. Patel, "SpiroSmart,"

in *Proceedings of the 2012 ACM Conference on Ubiquitous Computing - UbiComp '12*, 2012, p. 280.

[20] S. Huang and J. Liu, "Mobile phone based liquid crystal thermal imaging method and its medical implementation," *Zhongguo Yi Liao Qi Xie Za Zhi*, vol. 34, no. 5, pp. 317–22, Sep. 2010.

[21] J. Wojtczak and P. Bonadonna, "Pocket mobile smartphone system for the point-of-care submandibular ultrasonography," *Am. J. Emerg. Med.*, vol. 31, no. 3, pp. 573–577, Mar. 2013.

[22] S. K. Vashist, P. B. Luppa, L. Y. Yeo, A. Ozcan, and J. H. T. Luong, "Emerging Technologies for Next-Generation Point-of-Care Testing," *Trends Biotechnol.*, vol. 33, no. 11, pp. 692–705, Nov. 2015.

[23] G. Wu and M. H. Zaman, "Low-cost tools for diagnosing and monitoring HIV infection in low-resource settings," *Bull. World Health Organ.*, vol. 90, no. 12, pp. 914–920, Dec. 2012.

[24] C. D. Chin, V. Linder, and S. K. Sia, "Commercialization of microfluidic point-of-care diagnostic devices," *Lab Chip*, vol. 12, no. 12, p. 2118, May 2012.

[25] A. St John and C. P. Price, "Existing and Emerging Technologies for Point-of-Care Testing.," *Clin. Biochem. Rev.*, vol. 35, no. 3, pp. 155–67, Aug. 2014.

[26] Y. Kuo, S. Verma, T. Schmid, and P. Dutta, "Hijacking power and bandwidth from the mobile phone's audio interface," ... *First ACM Symp.* ..., 2010.

[27] T. B. Greenslade, "The Hydraulic Analogy for Electric Current," *Phys. Teach.*, vol. 41, no. 8, p. 464, Oct. 2003.

[28] M. Baser, "Hydraulic Capacitor Analogy," *Phys. Teach.*, vol. 45, no. 3, p. 172, Feb. 2007.

[29] K. W. Oh, K. Lee, B. Ahn, and E. P. Furlani, "Design of pressure-driven microfluidic

networks using electric circuit analogy," *Lab Chip*, vol. 12, no. 3, p. 515, 2012.

[30] D. C. Leslie *et al.*, "Frequency-specific flow control in microfluidic circuits with passive elastomeric features," *Nat. Phys.*, vol. 5, no. 3, pp. 231–235, 2009.

[31] M. R. Begley, M. Utz, D. C. Leslie, H. Haj-Hariri, J. Landers, and H. Bart-Smith, "Periodic response of fluidic networks with passive deformable features," *Appl. Phys. Lett.*, vol. 95, no. 20, pp. 2009–2011, 2009.

[32] R. R. Collino *et al.*, "Flow switching in microfluidic networks using passive features and frequency tuning.," *Lab Chip*, vol. 13, no. 18, pp. 3668–74, 2013.

[33] R. H. Phillips *et al.*, "Flow control using audio tones in resonant microfluidic networks: towards cell-phone controlled lab-on-a-chip devices," *Lab Chip*, vol. 80, pp. 3699–3707, 2016.

[34] F. Lu, H. P. Lee, and S. P. Lim, "Modeling and analysis of micro piezoelectric power generators for micro-electromechanical-systems applications," *Smart Mater. Struct.*, vol. 13, no. 1, pp. 57–63, Feb. 2004.

[35] C.-C. Wu, C.-C. Lee, G. Z. Cao, and I. Y. Shen, "Effects of corner frequency on bandwidth and resonance amplitude in designing PZT thin-film actuators," *Sensors Actuators A Phys.*, vol. 125, no. 2, pp. 178–185, 2006.

[36] C. J. Morris and F. K. Forster, "The correct treatment of harmonic pressure-flow behavior in microchannels," *Proc. ASME IMECE*, vol. MEMS, no. 2, pp. 473–479, 2000.

[37] S. M. Langelier, D. S. Chang, R. I. Zeitoun, and M. A. Burns, "Acoustically driven programmable liquid motion using resonance cavities.," *Proc. Natl. Acad. Sci. U. S. A.*, vol. 106, no. 31, pp. 12617–12622, 2009.

[38] M. Travagliati, G. De Simoni, C. M. Lazzarini, V. Piazza, F. Beltram, and M. Cecchini,

"Interaction-free, automatic, on-chip fluid routing by surface acoustic waves," *Lab Chip*, vol. 12, pp. 2621–2624, 2012.

[39] B. R. Lutz, J. Chen, and D. T. Schwartz, "Microscopic steady streaming eddies created around short cylinders in a channel: Flow visualization and Stokes layer scaling," *Phys. Fluids*, vol. 17, no. 2, pp. 1–7, 2005.

[40] V. O'Brien, "Pulsatile fully developed flow in rectangular channels," *J. Franklin Inst.*, vol. 300, no. 3, pp. 225–230, 1975.

[41] S. Vedel, L. H. Olesen, and H. Bruus, "Kilohertz microfluidics as an analytical tool for determining dynamic characteristics of microfluidic systems," *arXiv Prepr. arXiv*, vol. 20, no. 907, p. 2679, 2009.

[42] T. Bourouina and J. Grandchamp, "Modeling micropumps with electrical equivalent networks," *J. Micromechanics Microengineering*, vol. 6, no. 4, p. 398, 1996.

[43] R. Jain, R. B. Darling, and B. Lutz, "Frequency characterization of flow magnitude and phase in resonant microfluidic circuits," *Anal. Methods*, vol. 9, no. 37, 2017.

[44] R. Jain and B. Lutz, "Frequency tuning allows flow direction control in microfluidic networks with passive features," *Lab Chip*, vol. 17, no. 9, 2017.

[45] E. G. Richardson, "The amplitude of sound waves in resonators," *Proc. Phys. Soc.*, vol. 40, no. 1, pp. 206–220, Dec. 1927.

[46] A. Yakhot, M. Arad, and G. Ben-Dor, "Numerical investigation of a laminar pulsating flow in a rectangular duct," *Int. J. Numer. methods fluids*, vol. 29, no. 8, pp. 935–950, 1999.

[47] N.-S. Cheng, "Formula for the Viscosity of a Glycerol−Water Mixture," *Ind. Eng. Chem. Res.*, vol. 47, no. 9, pp. 3285–3288, 2008.

[48] J. D. Irwin and R. M. Nelms, *Basic engineering circuit analysis*. John Wiley, 2011.

[49] H. T. G. van Lintel, F. C. M. van De Pol, and S. Bouwstra, "A piezoelectric micropump based on micromachining of silicon," *Sensors and Actuators*, vol. 15, no. 2, pp. 153–167, 1988.

[50] E. Seker, D. C. Leslie, H. Haj-Hariri, J. P. Landers, M. Utz, and M. R. Begley, "Nonlinear pressure-flow relationships for passive microfluidic valves.," *Lab Chip*, vol. 9, no. 18, pp. 2691–7, Sep. 2009.

[51] S. Matsumoto, A. Klein, and R. Maeda, "Development of bi-directional valve-less micropump for liquid," in *Technical Digest. IEEE International MEMS 99 Conference. Twelfth IEEE International Conference on Micro Electro Mechanical Systems (Cat. No.99CH36291)*, 1999, pp. 141–146.

[52] H. Andersson, W. van der Wijngaart, P. Nilsson, P. Enoksson, and G. Stemme, "A valve-less diffuser micropump for microfluidic analytical systems," *Sensors Actuators B Chem.*, vol. 72, no. 3, pp. 259–265, Feb. 2001.

[53] B. Dahlbäck, "Blood coagulation," *Lancet*, vol. 355, no. 9215, pp. 1627–1632, May 2000.

[54] S. Bassus *et al.*, "Platelet-dependent coagulation assays for factor VIII efficacy measurement after substitution therapy in patients with haemophilia A," *Platelets*, vol. 17, no. 6, pp. 378–384, Jan. 2006.

[55] I. M. L. W. Keularts, K. Hamulyak, H. C. Hemker, and S. Béguin, "The Effect of DDAVP Infusion on Thrombin Generation in Platelet-rich Plasma of von Willebrand Type 1 and in Mild Haemophilia A Patients," *Thromb. Haemost.*, vol. 83, no. 4, pp. 638–642, Dec. 2017.

[56] G. Boden, V. R. Vaidyula, C. Homko, P. Cheung, and A. K. Rao, "Circulating Tissue Factor Procoagulant Activity and Thrombin Generation in Patients with Type 2 Diabetes: Effects of Insulin and Glucose," *J. Clin. Endocrinol. Metab.*, vol. 92, no. 11, pp. 4352–4358, Nov.

2007.

[57] N. Laurens, P. Koolwijk, and M. P. de Maat, “Fibrin structure and wound healing.,” *J. Thromb. Haemost.*, vol. 4, no. 5, pp. 932–939, May 2006.

[58] M. H. Kroll, J. D. Hellums, L. V McIntire, A. I. Schafer, and J. L. Moake, “Platelets and shear stress.,” *Blood*, vol. 88, no. 5, pp. 1525–41, Sep. 1996.

[59] M. Hoffman and D. M. Monroe, “Coagulation 2006: A Modern View of Hemostasis,” *Hematol. Oncol. Clin. North Am.*, vol. 21, no. 1, pp. 1–11, Feb. 2007.

[60] F. Josso and S. Beguin, “The Possible Role of Factor VII in the Intrinsic System,” in *Human Blood Coagulation*, Dordrecht: Springer Netherlands, 1969, pp. 77–81.

[61] L. Lorand and Middlebrook W, “The action of thrombin on modified fibrinogen,” *Thromb. Haemost.*, vol. 49, no. 3, pp. 208–213, Oct. 1983.

[62] A. H. Schmaier, “The elusive physiologic role of Factor XII.,” *J. Clin. Invest.*, vol. 118, no. 9, pp. 3006–9, Sep. 2008.

[63] A. T. Long, E. Kenne, R. Jung, T. A. Fuchs, and T. Renné, “Contact system revisited: an interface between inflammation, coagulation, and innate immunity,” *J. Thromb. Haemost.*, vol. 14, no. 3, pp. 427–437, Mar. 2016.

[64] Wikimedia Commons contributors, “Bibliographic details for File:Coagulation full.svg,” *Wikimedia Commons, the free media repository*, 2017. [Online]. Available: https://commons.wikimedia.org/w/index.php?title=Special:CiteThisPage&page=File%3ACoagulation_full.svg&id=235944811. [Accessed: 06-Feb-2018].

[65] R. F. Doolittle, “Structural Aspects of the Fibrinogen to Fibrin Conversion,” *Adv. Protein Chem.*, vol. 27, pp. 1–109, Jan. 1973.

[66] M. Kaibara and E. Fukada, “The effect of steady flow on transient viscoelastic behavior of

blood," *Biorheology*, vol. 18, no. 3–6, pp. 405–413, Dec. 1981.

[67] P. N. Walsh, "The Effects of Collagen and Kaolin on the Intrinsic Coagulant Activity of Platelets," *Br. J. Haematol.*, vol. 22, no. 4, pp. 393–405, Apr. 1972.

[68] Szalontai S, "Submicroscopic morphology of the fibrinogen-fibrin transition," *Fibrinogen*, no. Marcel Dekker New York, 1968.

[69] D. A. Triplett, "Coagulation and Bleeding Disorders: Review and Update."

[70] C. A. Lee *et al.*, "Influence of phospholipids on the assessment of factor VIII activity," *Haemophilia*, vol. 4, no. 4, pp. 646–650, Jul. 1998.

[71] P. Collins, N. Macartney, R. Davies, S. Lees, J. Giddings, and R. Majer, "A population based, unselected, consecutive cohort of patients with acquired haemophilia A," *Br. J. Haematol.*, vol. 124, no. 1, pp. 86–90, Jan. 2004.

[72] A. Tiede, R. E. Scharf, C. Dobbelstein, and S. Werwitzke, "Management of acquired haemophilia A," *Hamostaseologie*, vol. 35, no. 4, pp. 311–318, Jan. 2015.

[73] J. Delgado, V. Jimenez-Yuste, F. Hernandez-Navarro, and A. Villar, "Acquired Haemophilia: Review and Meta-Analysis Focused on Therapy and Prognostic Factors," *Br. J. Haematol.*, vol. 121, no. 1, pp. 21–35, Apr. 2003.

[74] C. R. M. Hay, S. Brown, P. W. Collins, D. M. Keeling, and R. Liesner, "The diagnosis and management of factor VIII and IX inhibitors: a guideline from the United Kingdom Haemophilia Centre Doctors Organisation," *Br. J. Haematol.*, vol. 133, no. 6, pp. 591–605, Jun. 2006.

[75] R. Parameswaran, A. D. Shapiro, J. C. Gill, and C. M. Kessler, "Dose effect and efficacy of rFVIIa in the treatment of haemophilia patients with inhibitors: analysis from the Hemophilia and Thrombosis Research Society Registry," *Haemophilia*, vol. 11, no. 2, pp.

100–106, Mar. 2005.

[76] P. Collins *et al.*, “Consensus recommendations for the diagnosis and treatment of acquired hemophilia A.,” *BMC Res. Notes*, vol. 3, p. 161, Jun. 2010.

[77] M. S. Kuntamukkula, L. V. McIntire, and E. A. Natelson, “A rheological study of the kinetics of coagulation in normal and hemophilic blood plasma,” *Biorheology*, vol. 16, no. 6, pp. 403–410, Dec. 1979.

[78] B. D. Spiess, K. J. Tuman, R. J. McCarthy, G. A. DeLaria, R. Schillo, and A. D. Ivankovich, “Thromboelastography as an indicator of post-cardiopulmonary bypass coagulopathies,” *J. Clin. Monit.*, vol. 3, no. 1, pp. 25–30, Jan. 1987.

[79] H. B. Moore *et al.*, “Viscoelastic Tissue Plasminogen Activator Challenge Predicts Massive Transfusion in 15 Minutes,” *J. Am. Coll. Surg.*, vol. 225, no. 1, pp. 138–147, Jul. 2017.

[80] L. Shen, S. Tabaie, and N. Ivascu, “Viscoelastic testing inside and beyond the operating room.,” *J. Thorac. Dis.*, vol. 9, no. Suppl 4, pp. S299–S308, Apr. 2017.

[81] C. Solomon, H. Schöchl, M. Ranucci, U. Schött, and C. J. Schlimp, “Comparison of fibrin-based clot elasticity parameters measured by free oscillation rheometry (ReoRox ®) versus thromboelastometry (ROTEM ®).,” *Scand. J. Clin. Lab. Invest.*, vol. 75, no. 3, pp. 239–46, 2015.

[82] S. Sølbeck, N. A. Windeløv, N. H. Bæk, J. D. Nielsen, S. R. Ostrowski, and P. I. Johansson, “In-vitro comparison of free oscillation rheometry (ReoRox) and rotational thromboelastometry (ROTEM) in trauma patients upon hospital admission,” *Blood Coagul. Fibrinolysis*, vol. 23, no. 8, pp. 688–692, Dec. 2012.

[83] O. Thomas, A. Larsson, N. Tynngård, and U. Schött, “Thromboelastometry versus free-oscillation rheometry and enoxaparin versus tinzaparin: an in-vitro study comparing two

viscoelastic haemostatic tests' dose-responses to two low molecular weight heparins at the time of withdrawing epidural catheters from ten patients after major surgery," *BMC Anesthesiol.*, vol. 15, no. 1, p. 170, Dec. 2015.

[84] World health organization, "WHO | Hospital medical equipment," *Core Med. Equip.*, vol. Online, no. http://www.who.int/medical_devices/priority/core_equipment/en/, 2017.

[85] S. M. Bates and J. I. Weitz, "Coagulation Assays," *Circulation*, vol. 112, no. 4, 2005.

[86] S. Kozek-Langenecker, "Management of massive operative blood loss.," *Minerva Anestesiol.*, vol. 73, no. 7–8, pp. 401–15.

[87] S. M. Donahue and C. M. Otto, "Thromboelastography: a tool for measuring hypercoagulability, hypocoagulability, and fibrinolysis," *J. Vet. Emerg. Crit. Care*, vol. 15, no. 1, pp. 9–16, Mar. 2005.

[88] J. L. Kashuk and E. E. Moore, "The Emerging Role of Rapid Thromboelastography in Trauma Care," *J. Trauma Inj. Infect. Crit. Care*, vol. 67, no. 2, pp. 417–418, Aug. 2009.

[89] A. D. Sharma, A. Al-Achi, J. F. Seccombe, R. Hummel, M. Preston, and D. Behrend, "Does incorporation of thromboelastography improve bleeding prediction following adult cardiac surgery?," *Blood Coagul. Fibrinolysis*, vol. 25, no. 6, pp. 561–70, Sep. 2014.

[90] K. Nogami, "The utility of thromboelastography in inherited and acquired bleeding disorders," *Br. J. Haematol.*, vol. 174, no. 4, pp. 503–514, Aug. 2016.

[91] K. Regling, S. Kakulavarapu, R. Thomas, W. Hollon, and M. B. Chitlur, "Utility of Thromboelastography for the Diagnosis of Von Willebrand Disease," *Blood*, vol. 128, no. 22, 2016.

[92] L. J. Enriquez and L. Shore-Lesserson, "Point-of-care coagulation testing and transfusion algorithms.," *Br. J. Anaesth.*, no. suppl 1, pp. i14-22, Dec. 2009.

[93] L. Müller *et al.*, "Investigation of Prothrombin Time in Human Whole-Blood Samples with a Quartz Crystal Biosensor," *Anal. Chem.*, vol. 82, no. 2, pp. 658–663, Jan. 2010.

[94] B. Ramaswamy, Y.-T. T. Yeh, and S.-Y. Zheng, "Microfluidic device and system for point-of-care blood coagulation measurement based on electrical impedance sensing," *Sensors Actuators B Chem.*, vol. 180, pp. 21–27, 2013.

[95] O. Cakmak *et al.*, "LoC sensor array platform for real-time coagulation measurements," in *2014 IEEE 27th International Conference on Micro Electro Mechanical Systems (MEMS)*, 2014, pp. 330–333.

[96] J. H. Barbee and G. R. Cokelet, "The Fahraeus effect," *Microvasc. Res.*, vol. 3, no. 1, pp. 6–16, Jan. 1971.

[97] M. Kaibara, "Rheology of blood coagulation," *Biorheology*, vol. 33, no. 2, pp. 101–117, Mar. 1996.

[98] J. V. Shah and P. A. Janmey, "Strain hardening of fibrin gels and plasma clots," *Rheol. Acta*, vol. 36, no. 3, pp. 262–268, May 1997.

[99] E. Fukada and M. Kaibara, "Rheological measurements of fibrin gels during clotting.," *Thromb. Res.*, vol. 8, no. 2 suppl, pp. 49–58, May 1976.

[100] I. K. Piechocka, R. G. Bacabac, M. Potters, F. C. MacKintosh, and G. H. Koenderink, "Structural Hierarchy Governs Fibrin Gel Mechanics," *Biophys. J.*, vol. 98, no. 10, pp. 2281–2289, May 2010.

[101] J. W. Weisel, "The mechanical properties of fibrin for basic scientists and clinicians," *Biophys. Chem.*, vol. 112, no. 2–3, pp. 267–276, Dec. 2004.

[102] S. Niewiarowski, E. Regoeczi, and J. F. Mustard, "Platelet Interaction With Fibrinogen and Fibrin: Comparison of the Interaction of Platelets With That of Fibroblasts, Leukocytes, and

Erythrocytes," *Ann. N. Y. Acad. Sci.*, vol. 201, no. 1, pp. 72–83, Oct. 1972.

[103] W. T. Sumner, D. M. Monroe, and M. Hoffman, "Variability in platelet procoagulant activity in healthy volunteers.," *Thromb. Res.*, vol. 81, no. 5, pp. 533–43, Mar. 1996.

[104] K. Vanschoonbeek *et al.*, "Initiating and potentiating role of platelets in tissue factor-induced thrombin generation in the presence of plasma: subject-dependent variation in thrombogram characteristics," *J. Thromb. Haemost.*, vol. 2, no. 3, pp. 476–484, Mar. 2004.

[105] H. C. Hemker, P. L. Giesen, M. Ramjee, R. Wagenvoord, and S. Béguin, "The thrombogram: monitoring thrombin generation in platelet-rich plasma.," *Thromb. Haemost.*, vol. 83, no. 4, pp. 589–591, 2000.

[106] K. E. Brummel-Ziedins, R. L. Pouliot, and K. G. Mann, "Thrombin generation: phenotypic quantitation," *J. Thromb. Haemost.*, vol. 2, no. 2, pp. 281–288, Feb. 2004.

[107] H. C. Hemker and S. Beguin, "Phenotyping the clotting system," *Thrombosis and Haemostasis*, vol. 84, no. 5. pp. 747–751, 2000.

[108] J. Ingerslev, L. H. Poulsen, and B. Sorensen, "Potential role of the dynamic properties of whole blood coagulation in assessment of dosage requirements in haemophilia," *Haemophilia*, vol. 9, no. 4, pp. 348–352, 2003.

[109] I. K. Piechocka, R. G. Bacabac, M. Potters, F. C. Mackintosh, and G. H. Koenderink, "Structural hierarchy governs fibrin gel mechanics.," *Biophys. J.*, vol. 98, no. 10, pp. 2281–9, May 2010.

[110] A. Floris *et al.*, "A prefilled, ready-to-use electrophoresis based lab-on-a-chip device for monitoring lithium in blood," *Lab Chip*, vol. 10, no. 14, p. 1799, Jun. 2010.

VITA

Originally from the city of Indore in Madhya Pradesh (translates to central state) in India, Rahil came to the US for graduate school. He found home at the Lutz lab in the Bioengineering department where he developed smartphone audio-powered microfluidic technologies for application in health diagnostic devices. Rahil has been recognized by the University of Washington for his innovation, and he was the Vikram Jandhyala Innovator of the Year in UW Electrical Engineering in 2015. He is the creator for two smart home products that use smartphones and smart speakers for control and monitoring of home (the first, Hook, is sold on Amazon). Rahil has won prizes in several business plan competitions and accelerator programs for these products. Along with entrepreneurial work, Rahil has made significant scientific advancements to the field of frequency-tuned flow control and analyte detection. Two of his publications have been featured on the front cover page on the premier journals in microfluidics. More information can be found on his LinkedIn page.